Department of Precision and Microsystems Engineering

Topology optimization of coupled heat problems

A. J. Hoogerbrugge

Report no	: 2019.012
Coach	: Ir. M. van der Kolk
Professor	: Dr. ir. M. Langelaar
Specialisation	: Engineering Mechanics and Mechatronic Systems Design
Type of report	: Master's Thesis
Date	: Thursday March 28, 2019

Delft
University of
Technology

Challenge the future

Topology optimization of coupled heat problems

An investigation of a combined thermo-mechanical and thermo-fluid topology optimization towards improving optical performance of a beam-steering mirror

by

A.J. Hoogerbrugge

to obtain the degree of Master of Science
at the Delft University of Technology,
to be defended publicly on Thursday March 28, 2019 at 01:00 PM.

Student number:	4048067	
Project duration:	November 13, 2017 – March 28, 2019	
Thesis committee:	Dr. ir. M. Langelaar,	TU Delft
	Dr. ir. R. A. J. van Ostayen,	TU Delft
	Ir. M. van der Kolk,	TU Delft
	Ir. A. H. Koevoets,	ASML

An electronic version of this thesis is available at `http://repository.tudelft.nl/`.

Abstract

In modern ASML machines optical components play an important role in the lithography process. EUV light is transported from the source to wafer by reflective optics. These mirrors are subjected to large thermal loading, as a large portion of the reflected light is absorbed in the mirror structure. The portion of the absorbed light is strongly dependent on the intensity and wavelength of the considered light, introducing varying amounts of thermally induced strains on the mirror structure and thereby limiting the optical performance.

Current mirror designs typically use solid mirror structures for more predictable deformations. These structures are coupled to spiral cooling channels to extract the absorbed heat to achieve more uniform temperature distributions. However, as ASML strives towards ever smaller resolutions, advances have to be found on the mirror design methodology to further reduce the thermally induced strains.

In this research, topology optimization is used as a possible method of producing designs which can minimise the thermally induced surface deformations of a mirror typically encountered when exposed to thermal loading. Due to the "multi-physics" nature of this problem, the optimization problem has to encompass thermo-mechanics, thermo-fluidics and the conjugate heat transfer at the interface of these two domains. The topology optimization formulation presented in this research, minimises surface deformations by altering the topology of the mirror structure together with the cooling channel layout producing an integrated solution.

Preface

This research was performed under the dual supervision of the department of Precision and Microsystems Engineering at the Technical University of Delft and the Flow and Temperature group at the Research department at ASML. The Advanced Thermal Control Consortium (ATCC), a group consisting of both industry and academia set up to better characterise thermal effects and subsequently improve thermal performance of systems in the the high-tech industry, was also a partial interest holder in the research.

The project would not have been possible without the diligent support of Max van der Kolk. Whose help spanned from implementation to project framing, debugging *hybrida* to debugging my misconceptions. My understanding of how to formulate a topology optimization problem is thanks to Max and his extensive prior work on the subject. Max's highly approachable demeanour throughout the thesis is greatly appreciated. At ASML, Marco Koevoets was a great source of discussion when sharing my early findings. Both by analysing my findings with engineering principles, but more importantly introducing some healthy skepticism for which to further investigate. My thanks also goes out to Matthijs Langelaar who, especially towards the final stages of the project, played an invaluable part in honing in the thesis.

The last year's move to Eindhoven was made quite a bit easier by the great group of interns at the Research department at ASML and the wonderful flat mates Michael and Rima. At the TU Delft: Sanne, Jian - the *hybrida* experts - also helped in debugging some of the more obscure issues faced, along with Stijn who kept up the pressure to finish already. One could always count on the administrative help of Eveline and Marianne who were great support and kept me jumping through the right hoops. Of course my parents, who have at all times been incredibly supportive and didn't so much as wince throughout the process. And Charlotte, who spent an unhealthy amount of time proof-reading first drafts, and spent the rest motivating me with holiday plans. Thank you.

A.J. Hoogerbrugge
Delft, March 2019

Nomenclature

The notation conventions adhered to in this research vary with the context. When model physics are being described symbolic notation is used. The moment an equation is to be implemented the switch is made to index notation. In both cases bold-faced uppercase letters refer to matrices, bold-faced lowercase letters refer to vectors and italic lowercase letters are scalars. Subscript and superscript italics refer to indices, where i generally refers to elements. Time derivatives, only covered in the literature study, are denoted with dots, whereby $\dot{\mathbf{u}}$ and $\ddot{\mathbf{u}}$ are the first and second order time derivatives of the displacement field.

Greek symbols

α	Thermal diffusivity
$\boldsymbol{\alpha}$	Thermal expansion vector
$\boldsymbol{\epsilon}$	Strain vector of mechanical contributions
$\boldsymbol{\epsilon}^*$	Strain vector of thermo-mechanical contributions
θ	Relative temperature $T - T_{\text{ref}}$
$\boldsymbol{\theta}$	Relative temperature field
κ	Permeability of Darcy flow region
λ_s	Thermal eigenvalue s
λ_i	Adjoint for the calculation of the adjoint sensitivities, where $i = 1, 2, \ldots$
μ	Dynamic viscosity
$\boldsymbol{\phi}^{(s)}$	Thermal mode vector of eigenvalue s
ρ	Physical element density for topology optimization
ρ_f	Fluid density
$\boldsymbol{\sigma}$	Stress vector
$\boldsymbol{\tau}_s$	Time constant of eigenvalue s

Roman symbols

A_surface	Surface area
$\mathbf{A}$	Thermal expansion matrix
$\mathbf{b}$	Internal pressure forces for Stokes flow
$\mathbf{B}_i$	Gradient matrix for fluid flow where $i = \mathrm{Da}, \mathrm{S}$
$\mathbf{B}_i^\top$	Divergence matrix for fluid flow where $i = \mathrm{Da}, \mathrm{S}$
c_p	Specific heat capacity
c_f	Pressure drop
$c_\mathrm{SD,max}$	Maximum permissible surface deformation
c_t	Thermal compliance
c_u	Mechanical compliance
C	Logarithmic constant in MSE formulation
$\mathbf{C}_\mathrm{T}$	Thermal capacitance matrix
$\mathbf{C}_\mathrm{U}$	Damping matrix
f	Objective function
$\mathbf{f}$	Force vector
$\mathbf{f}_\mathrm{v}$	Velocity force vector
$\mathbf{f}_\mathrm{p}$	Pressure force vector
g_i	Constraint number $i = 1, 2, \ldots$
$\mathbf{G}$	Displacement induced heat matrix
h	Convective heat transfer coefficient
$\mathbf{H}$	Stiffness tensor
$\mathbf{I}$	Identity matrix
k	Conduction
k_s	Conduction of solid
k_f	Conduction of fluid
$\mathbf{K}_\mathrm{C}$	Thermal convection matrix
$\mathbf{K}_\mathrm{D}$	Thermal conductivity/diffusivity matrix
$\mathbf{K}_\mathrm{Da}$	Darcy flow permeability matrix
$\mathbf{K}_\mathrm{S}$	Stokes flow viscosity matrix
$\mathbf{K}_\mathrm{T}$	Thermal conductivity/diffusivity matrix (in Literature study)
$\mathbf{K}_\mathrm{U}$	Stiffness matrix
$\mathbf{M}_\mathrm{U}$	Mass matrix
$\mathbf{M}_i$	Stability matrix for fluid flow where $i = \mathrm{Da}, \mathrm{S}$
M_ND	Measure of non-discreteness
MSE	Mean square error
$\mathbf{n}$	Normal unit vector
p	Pressure
Pe	Péclet number
$\mathbf{p}$	Pressure field
$\mathbf{q}$	Thermal flux
Q	Thermal energy
Re	Reynolds number
s	Design variable
$\mathbf{t}$	Mechanical tractions
T	Absolute temperature
T_ref	Reference temperature (293 K)
$\mathbf{u}$	Displacement field
v	Kinematic viscosity
$\mathbf{v}$	Velocity field
V	Volume
w	Wighting function in density filter

Contents

1 Introduction **1**
1.1 Motivation . . . 1
1.2 Problem statement and aims . . . 1
1.3 Approach and thesis outline . . . 2

2 Literature study **5**
2.1 Overview of considered physics . . . 5
  2.1.1 Thermo-mechanical model . . . 6
  2.1.2 Flow model . . . 6
  2.1.3 Thermo-fluid modelling . . . 7
2.2 Overview of existing work on topology optimization . . . 7
2.3 Comparison of optimization approaches . . . 10
  2.3.1 Density-based optimization approaches . . . 10
  2.3.2 Level-set optimization approaches . . . 11
2.4 Overview of the optimization loop . . . 11
  2.4.1 Optimization routines . . . 12
  2.4.2 Objective and constraint sensitivities . . . 12
  2.4.3 Filter formulations . . . 12
  2.4.4 Optimality conditions . . . 13
2.5 Objective functions and constraints in context of optical analysis . . . 13
2.6 Research choices . . . 14

3 Thermo-mechanical based optimization **17**
3.1 Thermo-mechanical domain and model definition . . . 18
  3.1.1 Co-located mechanical and thermal sinks . . . 19
  3.1.2 Separated mechanical and thermal sinks . . . 19
  3.1.3 State equations . . . 19
  3.1.4 Material penalisation and interpolation . . . 20
3.2 Optimization problem definition . . . 20
  3.2.1 Objective function . . . 20
  3.2.2 Constraints . . . 21
  3.2.3 Filter application to the topology optimization . . . 23
3.3 Optimization problems . . . 25
  3.3.1 Optimization problem 1: Surface deformation minimisation with a constant volume constraint . . . 25
  3.3.2 Optimization problem 2: Surface deformation minimisation with an active volume constraint . . . 25
  3.3.3 Optimization problem 3: Volume minimisation with surface deformation constraint . . . 26
3.4 Results . . . 26
  3.4.1 Co-located mechanical and thermal sinks . . . 27
  3.4.2 Separated mechanical and thermal sinks . . . 33
3.5 Discussion . . . 39

4 Thermo-mechanical and convection based optimization **41**
4.1 Thermo-mechanical and convective domain and model definition . . . 42
  4.1.1 Symmetric model . . . 43
  4.1.2 Asymmetric model . . . 45
  4.1.3 Modelling considerations of thermal boundary constraints of heat sink . . . 45
4.2 State equations . . . 46
4.3 Material interpolation . . . 46

4.4 Optimization problem . . . 47
  4.4.1 Optimization problem 4: Volume minimisation with surface deformation constraint . . . 47
4.5 Results . . . 47
  4.5.1 Symmetric model: Variation of Péclet . . . 47
  4.5.2 Asymmetric model: Variation of Péclet. . . . 48
  4.5.3 Symmetric model: Variation of channel numbers . . . 48
4.6 Discussion . . . 53

5 Thermo-mechanical, convective and flow based optimization 55
5.1 Thermo-mechanical, convective and flow domain and model definition . . . 56
5.2 Models with varying flow configurations . . . 56
5.3 State equations . . . 58
5.4 Material interpolation. . . . 58
5.5 Optimization problem . . . 58
  5.5.1 Flow energy dissipation (pressure drop) constraint . . . 58
  5.5.2 Optimization problem 5: Volume minimisation of a combined thermo-mechanical and thermo-fluid system . . . 59
5.6 Results . . . 60
  5.6.1 Selective domain optimization. . . . 60
  5.6.2 Model 1 . . . 61
  5.6.3 Model 2 . . . 61
  5.6.4 Model 3 . . . 62
5.7 Discussion . . . 62

6 Conclusions and Recommendations 65
6.1 Conclusions. . . . 65
6.2 Recommendations . . . 66

A Finite element discretisations 69
A.1 Thermo-mechanical . . . 69
A.2 Advection-diffusion. . . . 70
A.3 Flow. . . . 70

B Derivation of sensitivities 73
B.1 Surface deformations . . . 73
B.2 Adjoint sensitivities thermo-mechanical problem . . . 74
B.3 Adjoint sensitivities thermo-mechanical and convection problem . . . 74
B.4 Adjoint sensitivities thermo-mechanical, convection and flow problem . . . 75
  B.4.1 Pseudo-code implementation of $\frac{\partial \mathbf{K}_C}{\partial \mathbf{v}}\theta$ . . . 76
B.5 Adjoint sensitivities mechanical compliance constraint. . . . 76
B.6 Adjoint sensitivities thermal compliance constraint . . . 77
B.7 Sensitivities pressure drop constraint . . . 77

C Model and optimization details 79
C.1 Thermo-mechanical based optimization . . . 79
  C.1.1 Mesh characteristics . . . 79
  C.1.2 Material properties . . . 79
  C.1.3 Model parameters . . . 80
  C.1.4 Optimization parameters . . . 80
C.2 Thermo-mechanical and convection based optimization. . . . 80
  C.2.1 "Symmetric" model . . . 80
  C.2.2 Mesh characteristics . . . 80
  C.2.3 Material properties . . . 80
  C.2.4 Model parameters . . . 81
  C.2.5 Optimization parameters . . . 81
  C.2.6 "Asymmetric" model. . . . 81
  C.2.7 Mesh characteristics . . . 81
  C.2.8 Material properties . . . 82

C.2.9 Model parameters 82
C.2.10 Optimization parameters 82
C.3 Thermo-mechanical, convection and flow based optimization 82
C.3.1 Mesh characteristics 82
C.3.2 Material properties 82
C.3.3 Model parameters 84
C.3.4 Optimization parameters 84

D Extra density distributions and convergence plots 85
D.1 Density distributions 85
D.2 Convergence plots 89
D.2.1 Convergence of 3D symmetric models 89
D.2.2 Convergence of 2D asymmetric models 90
D.2.3 Convergence of 3D thermo-mechanical and thermo-fluid 91

E Finite differences 93

F Modal decomposition of advection-diffusion equation 95
F.1 1D Model 95
F.2 2D Model 95

Bibliography 99

1

Introduction

In ASML's never-ending quest to improve chip performance, engineers are forced into a state of creative overdrive. Their primary aim is simpler said than done: increase the transistor density in a chip. End-customers, often unknowingly, experience these advances in technology as longer battery-life of smartphones, faster boot-time of computers and instant results on search-engines. Although true that these examples are not the sole doing of ASML, the employees there are a thus far irreplaceable link in the chain of progress and responsibility.

ASML produces lithography systems; which in short, is the use of intense beams of light to burn patterns into a resist layer. This resist layer is highly reactive to the presence of light, and the reaction allows the resist layer to be removed in the targeted areas. Over the course of several layers and in combination with sequential layering of metals, insulators or other materials; is how a semiconductor takes shape.

1.1. Motivation

This research focuses on a single mirror in the light path of the source laser, a vital ingredient needed to produce low wavelength light for the newest generation of ASML's machines, namely *Extreme Ultra-Violet* (EUV). These mirrors are subject to heat loads and due to thermal expansion become a source of error. In an effort to control these errors that arise from thermally induced deformations, a system of cooling channels is to be integrated into the design of the mirrors.

Combining a mirror with a heat sink may seem at odds with the working principle of a mirror as a reflective device. However a certain percentage of light reflecting off of a mirror is always absorbed as heat. As the intensity of light increases, so too does the heat. Current methods of integrating heat sinks into optics have proven successful in meeting today's error budgets, however, future generations of ASML's machines may not be so forgiving. To overcome tomorrow's design problems, solutions have to become more integrated, meaning that to improve optical performance is to combine evermore physics.

1.2. Problem statement and aims

Multi-physics topology optimization is significantly more complex than single-physics topology optimization, this is due in part to the possible interactions between the physics, the problem formulation and material property interpolations. The problems are known to often converge to unclear layouts, which reduces the usefulness of the topology optimization results in the design practice.

The aim of this research is therefore to develop a fuller understanding of these interactions, and to find suitable problem formulations that yield clear and relevant results, with a focus on cases relevant to a 'heated mirror design'.

1.3. Approach and thesis outline

Layering more and more physics not only adds complexity to a simulation but also to a design optimization problem. A particularly versatile form of design optimization is *topology optimization* which can be perfromed on multi-physics problems. In topology optimization the question posed is: *What happens to the objective function when material is added or removed in a certain location?* This material can not only have an affect on the thermo-mechanical behaviour of the mirror but the topology optmization could also involve the removal or addition of material to alter the shape of a flow channel. Changing this material distribution anywhere in an optimization domain can be characterised as having a positive or detrimental effect on a chosen objective function.

Central to making the link between variations in material density and their effect on an objective function is the use of adjoint sensitivities. This adjoint method (as opposed to the direct method) reduces the computational cost and thereby enables the use of efficient gradient-based optimization algorithms.

In this research, a method is explored that allows for the improvement of optical performance of a mirror in a setting which combines thermo-mechanics and thermo-fluidics. The method outlined has been implemented in a code library called *hybrida*, an academic finite element library built and maintained by the department of Precision and Microsystems Engineering (PME) at the TU Delft. The research is carried out in the steady-state (time independent) setting, where wherever possible 2D elements have been used. In cases where the usefulness of 2D elements becomes limiting, the problem is then expanded to a "pseudo 2D" problem where 3D planes are used. The thermo-mechanics modelled are "one-way" coupled, which in this research means that temperature changes result in thermal strains.

In the literature study that follows hereafter, a review is made of the current state of affairs in regard to topology optimization for thermo-mechanical and thermo-fluid problems. Based on the outcome of this analysis the research direction within the field of topology optimization will be made clear.

Table 1.1: Progression of topology optimization complexity throughout the thesis. The diagram beneath the chapter columns is a 2D representation of the domain and physics taking part in the optimization problem. TM: Thermo-Mechanical, C: Convection, F: Flow

	Chapter 3	Chapter 4	Chapter 5
TM	◆	◆	◆
C		◆	◆
F			◆
	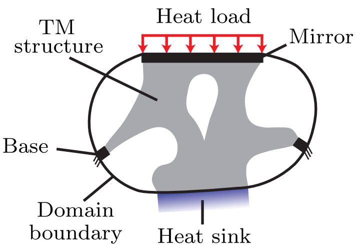 TM structure Heat load Mirror Base Domain boundary Heat sink	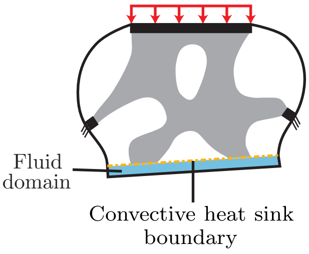	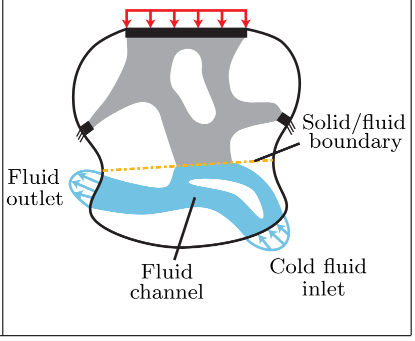 Solid/fluid boundary Fluid outlet Fluid channel Cold fluid inlet

Table 1.1 conveys the progression of the optimization problem through the chapters. Each chapter adds new physics given by the ◆ symbol. Black regions represent either the mirror or the fixed base, which are part of the analysis but not a design variable in the optimization problem. Grey regions represent the thermo-mechanical structure brought about as a consequence of the optimization and the light blue channel represents the fluid channel. Heat enters the system through the mirror and in Chapter 3 exits through the heat sink, in Chapter 4 through a fixed convective boundary and in Chapter 5 the optimization dictates precisely where along the solid-fluid interface convection takes place. The dotted yellow line therefore represents a separation between the solid and fluid optimization domains. The fluid inlet and outlet are predefined.

The following three chapters build sequentially upon each other. Due to the ever increasing complexity of adding different physics to the topology optimization it becomes more difficult to find root causes of problems and/or set correct parameters. Therefore, in Chapter 3: ‘Thermo-mechanical optimization’ first a thermo-mechanical model, seen in Table 1.1, is tackled where the basic thermal and mechanical models are tested and their physics interaction, compared. It should be noted that constraints are applied in a concerted effort to guide the topology optimization into obtaining a design which does not attempt to thermally or mechanically "uncouple" itself. Different ratios between these thermal and mechanical compliance constraints are tested and an overview is given of the influence of superimposed thermal and mechanical boundary conditions. Once it is deemed that a robust thermo-mechanical foundation has been set, a convection contribution is added to the thermal domain.

In Chapter 4: ‘Thermo-mechanical and convection optimization’, convection is added to the system. Heat is conducted through the thermo-mechanical structure and convected into cooling channels. The optimization selects these regions where the thermo-mechanical structure can best convect heat into the cooling channel. This convective interaction is given by $h\cdot(T-T_{\text{bulk}})$ where h is the heat transfer coefficient and the temperature difference is that between the solid/fluid interface and the bulk temperature of the fluid. Convection is used to describe the advection-diffusion interaction taking place at the fluid-solid interface and the heat transport of the fluid flow. In this chapter the flow channel is fixed, therefore its shape is not affected by the optimizer, and it functions as a heat-exchanger. The temperature of the cooling medium along the flow channel is set to rise as it absorbs thermal energy from the system. This asymmetric contribution of convection will be reflected in the optimized design of the thermo-mechanical structure. The convective quality of the flow channel will be tested using varying levels of the non-dimensional *Péclet* number in two flow regimes: in-plane and out of plane. The former provides connecting results to the previous (thermo-mechanical) chapter, the latter is used as a method of ascertaining the effect of the asymmetry on the conceived thermal structure but also on the surface deformations.

In Chapter 5: ‘Thermo-mechanical, convection and fluid optimization’, the final contribution, the fluid flow, is added to the optimization problem, where the system is permitted to choose areas in the domain for which convection is advantageous for the system performance. Different inlet and outlet configurations are considered to test not only surface deformation performance but also the cooling channel layout as far as the flow model permits.

Results will then be discussed and recommendations for future research will be given in the last chapter.

2

Literature study

The aim of this literature study is to ascertain the current state in the techniques and practices pertaining to the starting title of the research: "Transient topology optimization of coupled thermo-mechanical/thermo-fluid problem in beam steering mirrors". The goal therefore is to identify methods which can manipulate a material and fluid domain to produce an optimum in optical performance where a transient temperature flux agitates the system behaviour. Some transient aspects have been considered in the literature study however the final application was purely in the steady-state.

A combination of thermo-mechanical and thermo-fluid topology optimization has not yet been discovered in literature. Individually there have been instances where these topics are covered in both steady-state and most recently transient settings. This combination of physics (referred to as multi-physics) in a time transient setting has arguably only become possible to solve due to advances in processing capacity of computers. Traditionally transient topology optimization has been carried out using simplified methods such as: equivalent static loads or model order reduction [Behrou and Guest, 2017] due to the costly nature of solving for multiple time steps.

This literature study starts with explaining the different physics needed to model heat, elasticity and fluid equations; thereafter a selection of topology optimization works will be identified under the categories: "thermo-mechanical", "flow" and "thermo-fluid" where the application of the previously covered physics in a topology optimization can be seen. The optimization loop is then broken down into processes where the different topology optimization methods are discussed. An array of different methods is then analysed which can quantify optical performance. Due to the multi-physics nature of the problem this also includes thermal, mechanical and flow constraints which alter the converged design. Finally, the main research choices will be provided.

2.1. Overview of considered physics

Topology optimization requires state equations which dictate the physics of the design problem. State equations are derived from continuous governing equations in the form of partial differential equations and are subsequently discretised into a form represented by finite element methods (FEM). This finite element (FE) representation together with boundary conditions are then used as the building blocks for a topology optimization problem.

The coupled thermo-mechanical equations do not vary much in their representation in literature, whereas thermo-fluid models are more varied not only due to the modelling of heat transfer and heat transport however the advection-diffusion equations are often chosen in topology optimization. Fluid flow has by far the largest variation of representations, partly due to the large amount of flow conditions which exist but also because of the simplifications many make to gain computational performance.

2.1.1. Thermo-mechanical model

The linear thermo-mechanical equations have been derived from the conservation of energy for thermal analysis by e.g. Rixen [2011]. Two parts make up the thermo-mechanical equation, the heat flux through a thermal structure:

$$q = -k\nabla\theta \tag{2.1}$$

where k represents the conduction of a medium and $\nabla\theta$ the gradient of the relative temperature $\theta = T - T_{\mathrm{ref}}$. The stress contributions can be summarised as:

$$\boldsymbol{\sigma} = \mathbf{H}(\boldsymbol{\epsilon} - \boldsymbol{\epsilon}^*) \tag{2.2}$$

where $\mathbf{H}$ is Hooke's matrix and $\boldsymbol{\epsilon}^*$ the strain contribution of the mechanical system $\boldsymbol{\epsilon}$ and of thermal expansion $\boldsymbol{\epsilon}^* = \boldsymbol{\alpha}(T - T_{\mathrm{ref}})$ where $\boldsymbol{\alpha}$ is the thermal expansion vector. These equations are then discretised into their FE representation which for the purposes of the literature study also include the time dependent contributions (first order represented by $\dot{\bullet}$ and second order by $\ddot{\bullet}$). The fully coupled equations are therefore:

$$\begin{aligned} \mathbf{M}_{\mathrm{U}}\ddot{\mathbf{u}} + \mathbf{C}_{\mathrm{U}}\dot{\mathbf{u}} + \mathbf{K}_{\mathrm{U}}\mathbf{u} &= \mathbf{f} + \mathbf{A}\boldsymbol{\theta} \\ \mathbf{C}_{\mathrm{T}}\dot{\boldsymbol{\theta}} + \mathbf{K}_{\mathrm{T}}\boldsymbol{\theta} &= \mathbf{q} + \mathbf{G}\dot{\mathbf{u}} \end{aligned} \tag{2.3}$$

where the structural mass matrix is given by $\mathbf{M}_{\mathrm{U}}$, the mechanical damping by $\mathbf{C}_{\mathrm{U}}$, the thermal capacitance by $\mathbf{C}_{\mathrm{T}}$, the mechanical stiffness by $\mathbf{K}_{\mathrm{U}}$ and the conduction matrix $\mathbf{K}_{\mathrm{T}}$ (which we later refer to as $\mathbf{K}_{\mathrm{D}}$ for diffusivity). The coupling term containing the thermal expansion is $\mathbf{A}$ and the reverse coupling term for which a temperature gradient is created through deformations is $\mathbf{G}$ (where $\mathbf{G} = T_{\mathrm{ref}}\mathbf{A}^{\top}$). The mechanical load is given by $\mathbf{f}$ and the thermal load by $\mathbf{q}$. The degrees of freedom (DOF) are displacement $\mathbf{u}$ and the relative temperature $\boldsymbol{\theta}$ where dots over the DOFs represent time derivatives.

From the state equations the modal time constants of both the thermal and mechanical structure can be derived. Time constants relate the modes of the degrees of freedom to response times and are extracted from the modal equation which for the thermal equation can be extracted by substituting $\boldsymbol{\theta} = \boldsymbol{\phi}^{(s)}e^{-\lambda_s t}$ into the thermal equation and calculating the eigenmodes $\boldsymbol{\phi}^{(s)}$ and eigenvalues λ_s. The time constants are then $\tau_s = 1/\lambda_s$ and ordered by decreasing magnitude. Dugge [2012] analyses the use of time constants in topology optimization and Hooijkamp and Van Keulen [2017] use time constants in a model order reduction technique for topology optimization. Rixen [2011] furthermore describes the non-dimensional *Boley number* $\mathrm{Bo} = \frac{t_{\mathrm{t}}}{t_{\mathrm{u}}}$ used as an indicator for whether "thermal excitations can induce mechanical oscillations" concluding that this is only really witnessed in satellites, where severe temperature gradients and slender structures are common. None the less, highly compliant mechanical structures and thermal structures that induce high temperature gradients should be avoided.

2.1.2. Flow model

Flow modelling has been widely documented for many different flow regimes. This research will concentrate on incompressible laminar channel flow. Looking at the Navier-Stokes equation we can gain more insight on the needed flow aspects. The Navier-Stokes equation (e.g. Donea and Huerta [2005]) is given by:

$$\mathbf{v}_{,t} + (\mathbf{v}\cdot\nabla)\mathbf{v} - \nu\nabla^2\mathbf{v} + \nabla p = \mathbf{b} \tag{2.4}$$

where the conservation of mass $\nabla\cdot\mathbf{v} = 0$ is assumed, which means the divergence of the velocity $\mathbf{v}$ is zero. Furthermore, $\mathbf{v}_{,t}$ are time variations of the velocity, ν is the kinematic viscosity of the fluid, ∇p represents the internal pressure forces and $\mathbf{b}$ are the volume forces per unit mass. This can be rewritten in a non-dimensional form:

$$(\mathbf{v}\cdot\nabla)\mathbf{v} - \frac{1}{\mathrm{Re}}\nabla^2\mathbf{v} + \nabla p = 0 \tag{2.5}$$

where Re, the dimensionless Reynolds number, is used to describe the ratio between flow inertia and viscosity. At high Reynolds numbers, the flow is inertia-dominated whereas for low Reynolds numbers the flow is viscosity-dominated. By taking the assumption of low Reynolds numbers we can state that there will be an out-sized contribution of the viscous dominated or "diffusivity" term.

The remaining equation is termed Stokes equation [Donea and Huerta, 2005]:

$$\nu\nabla^2\mathbf{v} + \nabla p = \mathbf{b}. \tag{2.6}$$

A channeling technique is required to bound fluid flow regions (modelled by the aforementioned methods) from solid regions. This is generally performed by interpolating between the two regions. Although Stokes flow is enough to model flow within predefined boundaries, topology optimization of fluid channels requires that the sides or boundaries of the flow be allowed to move within the domain. As opposed to having a fully permeable region, shown in Figure 2.2d, impermeable regions allow the topology optimization to form areas of no flow. This is done by modelling an internal force that is often linked to an *inverse permeability* $(1/\kappa)$ term [Yaji et al., 2015, Nørgaard et al., 2016] also called an absorption term [Gersborg-Hansen et al., 2005]. These methods are based on Darcy flow which can be *homogenized* together with Stokes flow to produce solid domains or highly impermeable flow regions:

$$\left((1-\rho)\mu\nabla^2 - \rho\frac{\mu}{\kappa}\mathbf{I}\right)\mathbf{v} - \nabla p = \rho_f \mathbf{b}. \tag{2.7}$$

Here ρ pertains to the physical densities associated with the topology optimization and not the fluid density, μ is the dynamic viscosity, $1/\kappa$ the inverse permeability, $\mathbf{I}$ the identity matrix and ρ_f the fluid density. The terms $(1-\rho)$ and ρ dictate the interpolation between Stokes flow and Darcy flow.

2.1.3. Thermo-fluid modelling

Thermo-fluid modelling is the term most often found in literature when referring to topology optimization of fluid heat exchangers. What is meant by thermo-fluid is only the heat transfer into the fluid and heat transport carried by the fluid. This physical phenomenon can be captured by the advection-diffusion equation, where advection is the general term for heat convection and diffusion a term for conduction. Literature calls this thermal exchange *conjugate heat transfer* [Alexandersen, 2016]. The advection-diffusion equation in the fluid domain is:

$$\rho_f c_\mathrm{p}(\mathbf{v}\cdot\nabla)\theta - k_\mathrm{f}\nabla^2\theta = 0 \tag{2.8}$$

where c_p is the thermal heat capacity, $\mathbf{v}$ velocities, k_f the thermal conductance of the fluid and θ is the reference temperature. In the solid domain the velocities $\mathbf{v}$ drop to zero and the conduction then becomes that of a solid:

$$k_\mathrm{s}\nabla^2\theta + Q = 0 \tag{2.9}$$

where k_s is the thermal conductance of the solid and Q the thermal energy. Similar to Equation 2.7, interpolation between Equation 2.8 and 2.9 is performed to ensure that the thermal characteristics of the impermeable regions reflect that of a solid.

2.2. Overview of existing work on topology optimization

Topology optimization has successfully been applied in many use cases in the steady state regime. Its wide use is in part thanks to Bendsoe and Sigmund [2003] who wrote the handbook on topology optimization and presented many applications including thermo-fluid and thermo-mechanical ones. As opposed to designing by intuition and design principles, topology optimization allows you to use the very physics that define the problem, to design a solution. This means that the user can approach a problem with very little prior knowledge of the design, although care should be taken in interpreting the results. Resulting designs can often be deemed organic or natural, Figure 2.1 shows aeroplane wings exhibiting high detail bone-like structures; passive heat-sinks appearing like corals and flow networks appearing like capillaries or tributaries leading to a main artery. The resemblance of designs emerging from topology optimization to designs based on biomimicry are striking, however the mathematical underpinnings of the former are tangible whereas the latter suffers from being a natural form of evolution which cannot as easily be replicated.

Stereotypically this formulation consists of steady state physics and inputs. However topology optimization can also be performed with respect to the time domain or frequency domain. Bendsoe and Sigmund [2003] describes some methods for applying topology optimization to time transient cases, and it would appear that the first use cases were seen in crashworthiness cases such as in Pedersen [2004] and on thermal actuation of compliant mechanisms in Li et al. [2004] where time-dependent physics and time integration steps are integrated into the optimization. In the frequency domain Hooijkamp and Van Keulen [2017] applied modal order reduction on thermal conduction problems to characterise the transient nature of structures.

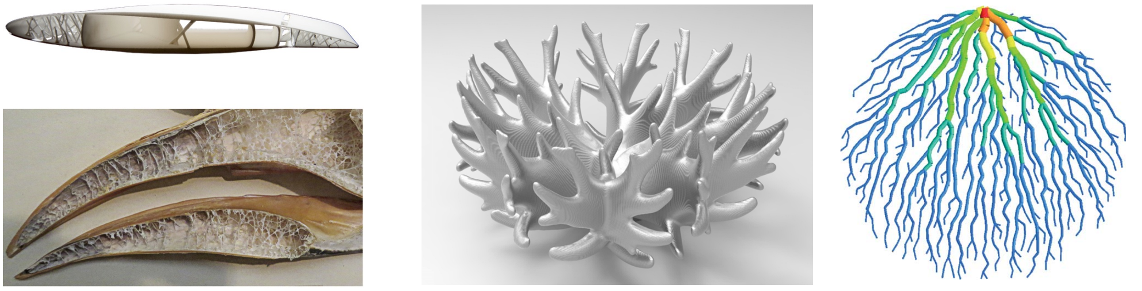

(a) Airplane wing cross-section compared to bird beak Aage et al. [2017].

(b) Coral-like natural convection heat sink Alexandersen [2016].

(c) Arterial tree-type flow network Klarbring et al. [2003].

Figure 2.1: Resulting designs of topology optimization, showing an organic appearance.

The main bulk of work on topology optimization applied to thermo-mechanics is in the use of thermo-mechanical actuators for micro-electromechanical systems (MEMS) in in-plane use [Sigmund, 2001], out-of-plane buckling scenarios [Wu et al., 2018] and including transient effects [Li et al., 2004]. There are however certain examples to be found on mirrors for high-powered lasers in Kim et al. [2005] where a mean square error (MSE) minimisation is applied to an asymmetric model, where the results are then presented in terms of Zernike polynomials, and on the design of lightweight mirrors [Lee, 2005] where a multi-objective optimization of the MSE surface deformations and *Strehl ratio* (a measure of lens aberrations) is performed. Work has also been performed in optical settings by Koppen et al. [2018] in a system based approach by optimizing optics based on cumulative performance as opposed to individual performance of reflective surfaces.

For the flow problem, topology optimization has successfully been performed at different complexities. Fluid flow topology optimization stems from Borrvall and Petersson [2003] where a combination of Stokes, which can best be described as creeping flow for low Reynolds numbers, and Darcy flow, which models fluid permeating through porous media, are used to create fluid channels in a domain with varying permeability. The advantages of this combination of flow models are that within the flow domain it is possible to veer from one flow form to the other, using the same density-based technique as in the thermo-mechanical optimization and no extra boundary conditions have to be introduced between flow regimes [Guest and Prévost, 2006]. The density scales between $0 < \rho_i \leqslant 1$, 0 representing full Stokes flow and 1 fully impermeable flow in an element modelled by Darcy flow. The addition of Stokes and Darcy system matrices have to be *homogenized* as originally done by Sanchez-Palencia [1980] by the scaling term κ/μ where κ is the permeability as set out by the Darcy matrix and μ the viscosity of the flow shared by both matrices. Gersborg-Hansen et al. [2005] expands on Stokes and replicates the technique using Navier-Stokes. This is more accurate as it adds inertial aspects to the fluid model. Both these methods try to reduce fluid friction - which can also be considered as a pressure drop - of the flow channels.

In Figure 2.2 a few results of Gersborg-Hansen et al. [2005] are presented showing the effect of the Reynolds number on topology optimization based on Navier-Stokes modelling. The aim is to increase fluid compliance, which can be viewed as a method of creating a channel which causes least resistance for the fluid flow. What can be seen in Figure 2.2 are the different channel designs which provide the lowest flow resistance for varying Reynolds numbers.

Stokes flow, also called creeping is accurate for $\mathrm{Re} \ll 1$, however comparing Figure 2.2a to Figure 2.2b the influence of inertia is seen to be quite limited on the optimization problem when the Reynolds number is many times higher, namely $\mathrm{Re} = 50$. In Figure 2.2c the influence of inertia becomes clearly visible, where the fluid quite literally "throws" its weight out.

Conjugate heat transfer, where heat is transferred from solid to fluid, has also readily been handled in literature. Powerful computational fluid dynamics and additive manufacturing has allowed for great improvements in the performance of heat exchangers by reducing pressure drop across inlet and outlet and increasing the effective heat transfer, therefore improving compactness and weight of heat exchange units [Saunders, 2018]. This can be seen in Figure 2.3 where a gas-to-gas heat exchanger or "annular recuperator" used to extract heat from a micro gas turbine is shown. The FE model has been investigated by Tang and Jiang [2006] where the numerical method is described in combination with Navier-Stokes flow. Good results have been produced by Dede [2009]

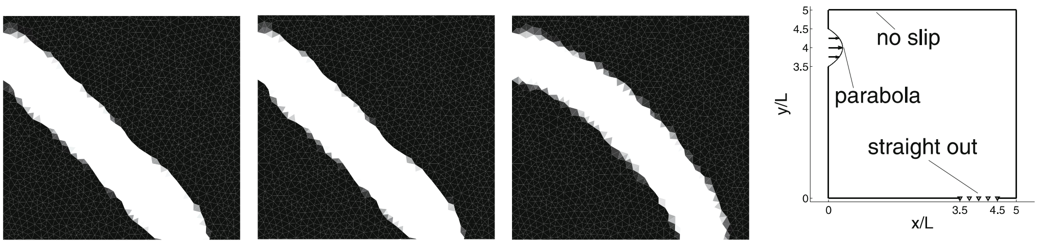

(a) Re = 0 (b) Re = 50 (c) Re = 850 (d) Domain configuration.

Figure 2.2: Comparison of fluid compliance optimization with varying Reynolds numbers from Gersborg-Hansen et al. [2005]. Parabolic input velocity profile entering the domain from the top left. Channels are represented in white, impermeable regions in black.

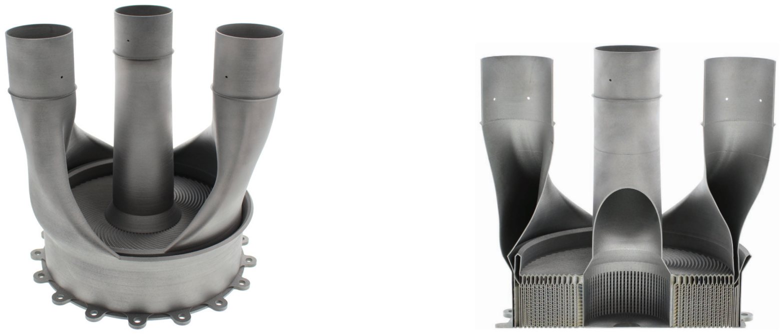

Figure 2.3: "Annular recuperator" or high efficiency heat exchanger for two separate gas flows designed by HiETA Technologies [Saunders, 2018], manufactured using additive manufacturing.

who compares a single and multi-physics optimization method. Matsumori et al. [2013] and Yaji et al. [2015] show general trends for laminar flow whereby their converged solutions show wide channels for low Reynolds numbers Re ≈ 10 and for increasing Reynolds numbers up to Re ≈ 100, more intricate channels are produced. Yaji's most recent work [Yaji et al., 2018] in 3D unsteady flow provides incredibly complex designs by applying parallel computing to the optimization problem. Structures provided by this most recent method can be seen in Figure 2.4 and have little to no resemblance to the current state of heat exchangers presenting an evolution towards designs with little explicable design language. To note is that Yaji et al. [2018] used a supercomputer with up to 512 nodes to achieve these results, each optimization iteration took up to 251 seconds.

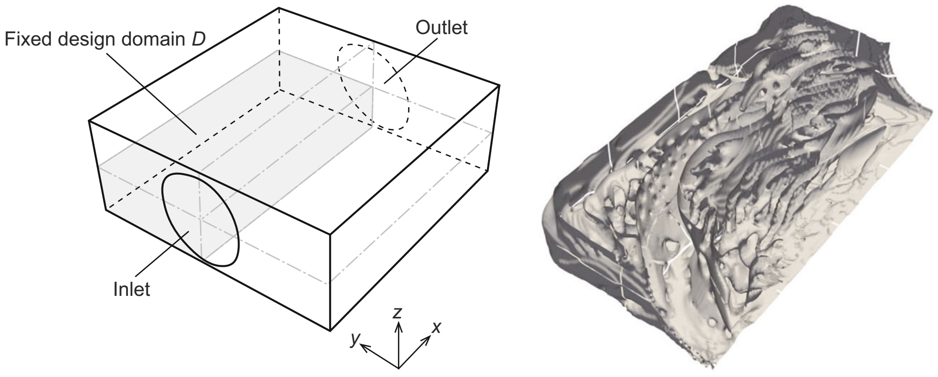

(a) Domain of conjugate heat exchanger. Assuming the optimized design be symmetrical, only a quarter of the design domain is optimized.

(b) Quarter symmetry representation of heat exchanger. Note the exceptionally complex and intricate flow channels.

Figure 2.4: Yaji et al. [2018] designed conjugate heat exchangers using topology optimization. The objective was to optimize heat transfer where a pressure drop constraint was applied. This was performed in a transient setting using a novel technique to reduce memory use of computations.

All these examples show a general trend of increasing complexity and scale, leading to larger computational requirements. Transient topology optimization is a feature lagging in commercial software packages and together with large scale optimization, the reason why the most elaborate and ambitious academic papers use bespoke code. These examples use compiled coding languages such as Fortran or C++ which are typically much more efficient than interpreted code such as Python or Matlab at performing numerical computing work. Kouatchou [2018] gives a basic comparison of the same command being performed in different coding languages, it quite clearly shows the gains of using compiled code.

Simplifications can be done in order to still make meaningful analyses from interpreted code. Choosing 2D models over 3D and simplifying model physics will reduce the computational requirements and limits the required implementation time.

2.3. Comparison of optimization approaches

In this literature study only continuous design variable methods will be compared as it has generally been proven that discrete methods are not as efficient and often do not converge to global minima [Sigmund and Maute, 2013].

A basic topology optimization loop, given in Figure 2.5, consists of a simulation step where a finite element analysis (FEA) is performed using the current design variable configuration. System performance is measured based on the outcome of this step. Thereafter the design sensitivities are calculated. These sensitivities express the variation of the objective function and constraints with respect to changes in the design variables. This information is then relayed to the optimizer which calculates a new design variable configuration. Whether a converged design has been reached is based on whether a predefined relative tolerance has been met over a number of consecutive optimization iterations.

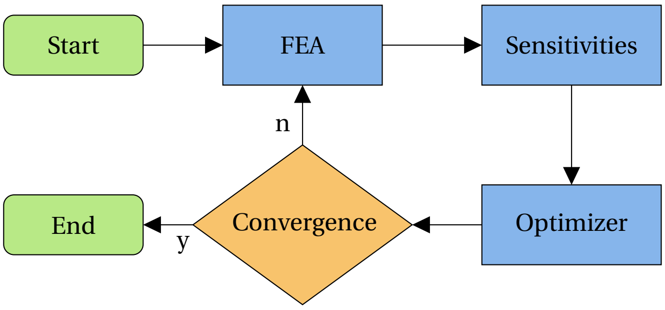

Figure 2.5: Simplified system representation of an optimization loop.

There are four main categories for continuum topology optimization approaches with continuous design variables [Sigmund and Maute, 2013]: density-based, level-set, topological derivatives and phase-field. All these methods use gradient-based optimizers described in Section 2.4.1. The most commonly used methods in thermo-mechanical and thermo-fluid topology optimization are density-based and thereafter level-set which is also where we will narrow the discussion to.

2.3.1. Density-based optimization approaches

Density-based approaches scale the local material properties with a value between zero and one. Zero would usually represent a void region and one would retain full material properties. Scaled properties in mechanics would be the stiffness matrix, in thermo-mechanics the thermal expansion and conductivity matrix. For fluid flow the scaling term ρ interpolates two terms: the diffusivity term $(1-\rho)\mu\nabla^2\mathbf{v}$ and the Darcy term $\rho\frac{\mu}{\kappa}\mathbf{v}$. Two reasonably similar methods exist for density penalisation: *Simplified Isotropic Material with Penalization* (SIMP) and *Rational Approximation of Material Properties* (RAMP) both covered in Bendsoe and Sigmund [2003] but the latter originating from Stolpe and Svanberg [2001]. Both perform the same task which is to promote density values of zero or one in the optimization process, thereby reducing *grey* areas. RAMP however gains a computational advantage of not having a gradient of zero in void regions [Sigmund and Maute, 2013] which allows the density distribution to more easily evolve [Hooijkamp et al., 2014].

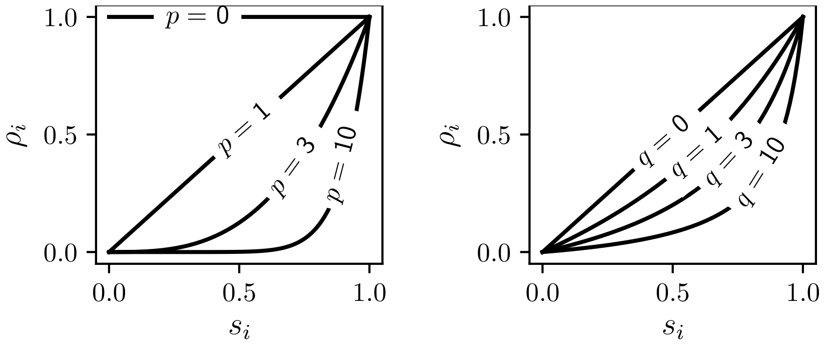

(a) SIMP scaling term for p=0,1,3,10. (b) RAMP scaling term for q=0,1,3,10.

Figure 2.6: Comparison of penalisation schemes. Note the difference in gradient for $\lim_{s_i \to 0} \frac{\partial \rho_i}{\partial s_i}$.

SIMP penalisation scales densities between $\rho_{\min} \leq \rho \leq 1$. The value $\rho_{\min}$ is not quite zero to prevent the derivative vanishing at the minimal density. Figure 2.6a shows SIMP scaling with parameter p:

$$\rho_i = s_i^p. \tag{2.10}$$

RAMP penalisation, similar to SIMP, designates the design variables s_i with values at the outer limits of $\rho_{\min} \leq \rho \leq 1$ so as to produce topologies with a higher contrast. This also reduces so called *grey areas* from forming and therefore increases definition and manufacturability of the output density distribution. RAMP penalisation scales the density term for each element i as follows:

$$\rho_i = \frac{s_i}{1 + q(1 - s_i)} \tag{2.11}$$

here s_i is the output of the optimizer and q a parameter of the RAMP penalisation scheme. In Figure 2.6b the effect of the q parameter can be seen on the scaling term.

Gao and Zhang [2010] compare both SIMP and RAMP on a thermo-elastic topology optimization using a volume constraint, and reach the conclusion that "RAMP leads to stable iterations and clear optimization configurations". This does not necessarily mean that this should be the case in all scenarios. A similar comparison has not been found in topology optimization of flow channels.

2.3.2. Level-set optimization approaches

Level-set approaches define the regions between two different phases by implicitly defining contour lines between the two regions. By optimizing these boundaries, as opposed to the properties of discrete elements that make up the mesh, level-set approaches have a far superior boundary quality to density-based approaches [Van Dijk et al., 2013]. While density-based approaches can suffer from step-wise boundaries at the interface of two material phases (alleviated by choosing a finer mesh, remeshing at high density gradients or adding density filters), level-set methods do not suffer from these disadvantages. However the level-set method has difficulty forming new void regions within solid domains, which can restrict it from converging to a global optimum [Sigmund and Maute, 2013].

2.4. Overview of the optimization loop

The optimization loop can be broken down into sub-problems shown in Figure 2.5. A few of the more prevalent optimizers will be discussed, thereafter methods of reducing the computational load when deriving the sensitivities of the FEA, based on the physical models covered in Section 2.1. Although not shown in Figure 2.5 because their inclusion is widespread, filtering techniques will be covered to show their influence on the converged designs. To provide insight in to how far convergence has come, some insight in to optimality conditions will be discussed.

2.4.1. Optimization routines

The two previously described optimization approaches belong to the family of continuous design variable approaches where gradient-based methods are very efficient. These gradients (sensitivities) provide a direction for the optimizer to converge to the global optimum. Other optimization algorithms exist, such as *non-gradient*, but these are generally used for discrete variable problems, and *Hessian-based* but this is better suited to problems with a smaller number of design variables [Dbouk, 2017]. The most used algorithms found in topology optimization literature are *sequential quadratic programming* (SQP), its commercial variant *sparse nonlinear optimizer* (SNOPT), *method of moving asymptotes* (MMA), and its variant *global convergent MMA* (GCMMA). All these methods are highly effective in converging quickly to an optimal design however, the most used of these in topology optimization is MMA [Sigmund and Maute, 2013]. All these methods accept linear and non-linear objectives and constraints. However, Sigmund and Maute [2013] recommend the use of MMA when combining different physics due to the ease in which MMA can handle added complexity.

2.4.2. Objective and constraint sensitivities

Gradient-based methods require sensitivities as an input to the optimizer to calculate new density distributions. Sensitivities in topology optimization are a measure of the effect a variation in the design variable s_i has on an objective or constraint. Haftka [1981] outlined two methods to calculate the sensitivities on thermal systems referred to as the direct method and the adjoint method for thermal analysis. The direct method furthermore calculates the derivatives of the entire structural response (i.e. $\frac{\partial \Theta}{\partial \rho}$), which is only more efficient than taking adjoints when the number of constraints exceeds that of design variables. The adjoint method calculates the derivatives of the performance or response function with respect to the design variables. This is a less costly problem to solve when the design variables outnumber the constraints. Van Keulen et al. [2005] adds that the differentiation only needs to be performed on elements that are affected by the design variables. Meaning that loading terms need not be differentiated as they are independent of the design variables.

2.4.3. Filter formulations

Although topology optimization produces density distributions which in theory would give an improved performance, these distributions sometimes suffer from artefacts. One example is "checkerboarding" which occurs when neighbouring elements take on opposite density extremes in quick succession as it creates regions of "artificially high (numerical) stiffness" [Sigmund, 1997] which arises from bad numerical modelling and is a problem associated with low-order elements. Although good (optimization) performance can be obtained by the converged design, their physical validity is questionable and manufacturability even worse. Filtering is a method of improving convergence without adding extra constraints to the optimization problem. Density and sensitivity filtering can help remove signs of checkerboarding and local density anomalies (caused by mesh dependency) without altering the volume fraction.

The sensitivity filter is highly effective in attaining a mesh-independent design, providing a certain type of robustness against any unforeseen consequences mesh choice or mesh refinement may have [Sigmund, 1997; Sigmund and Petersson, 1998]. The sensitivity filter, similarly to density filtering, is a weighted average of neighbouring elements. In practice this applies a softening effect on local features which in this case are mesh irregularities. Comparing Figures 2.7a and 2.7b clearly shows the effect of the sensitivity filter. There are problems associated to this type of filtering, as by changing the sensitivities, the gradient information of the optimization is changed hence the optimization path is altered which can mean that the optimization does not converge. However Sigmund and Maute [2012] claim that "a gradient can be altered considerably without compromising the convergence" and "may promote convergence of some length scales over others and thereby speed up convergence".

The density filter blurs the density field by making the density of each element a weighted average of its neighbouring elements. In turn the system matrices free themselves of "granular" behaviour [Bendsoe and Sigmund, 2003] and become a function of a weighted average of neighbouring elements. Figure 2.7b shows the step-wise behaviour of the boundary we are referring to as a possible source of granular behaviour, and Figure 2.7c shows the boundaries turned grey.

Filtering can also be used to influence the convergence of optimization to add design contributions such as introducing length scales to designs. Guest et al. [2004] introduced a projection scheme for precise control

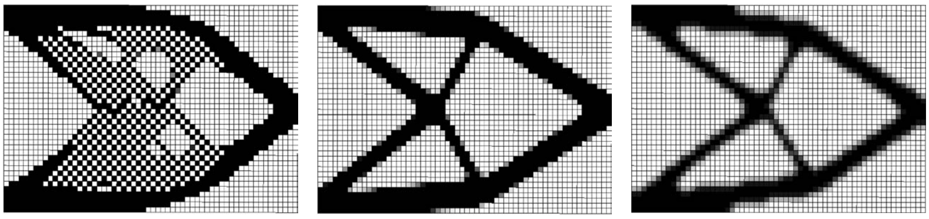

(a) Result of no filtering. Checkerboarding is very evident.

(b) Result of applying the sensitivity filter on the optimization problem. Note the step-wise boundaries.

(c) Sensitivity and density filter applied to the optimization problem.

Figure 2.7: Results produced by Bruns [2005] showing typical results after sequentially applying different filters to an optimization problem.

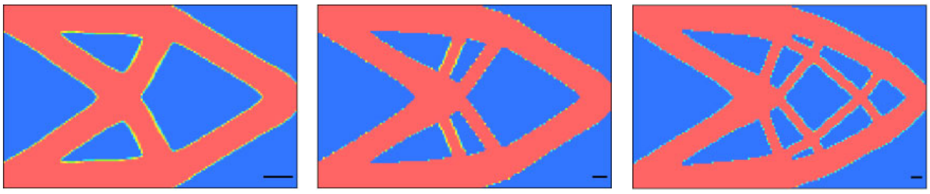

Figure 2.8: Varying minimum length scales introduced to the same optimization problem produced by Guest et al. [2004]. Black bar in bottom right corner represents the prescribed length.

over how thin structural members can become. Figure 2.8 shows varying levels of intricacies prescribed by introducing a minimum length scale filter. This filter can be used in conjunction with compliance constraints to reach designs that may be more adequate.

2.4.4. Optimality conditions

Certainty that a high-dimensional non-convex optimization problem has converged to a global minimum cannot be guaranteed. Inherent to topology optimization is searching for an optimum with as many dimensions as there are design variables. Adding constraints does not necessarily improve the situation, as although the design space becomes smaller, these newly introduced boundaries in the design space can create more local minima.

For optimizations that remain in a state of grey, Sigmund [2007] proposed a method of gauging the fraction of design variables that have not reached a design variable limit (ρ_{min} or 1). The name given to this is *Measure of Non-Discreteness* and is calculated as follows:

$$M_{\text{ND}} = \frac{\sum_{i=1}^{n} 4\hat{\rho}_i(1-\hat{\rho}_i)}{n} \times 100\% \tag{2.12}$$

here $\hat{\rho}_i$ is the filtered density of an element and n the total number of elements. A value of 0% represents all filtered element densities are discrete (equal to $\hat{\rho}_{\text{min}}$ or one), and a value of 100% would signify that all filtered element densities have a value of 0.5. Ideally the aim is to have a fully discretised system. However, the density filter makes this impossible, as it will always interpolate at interfaces between discrete areas. In Sigmund [2007] different filters are tested and their M_{ND} values range between 0.36 and 24.02%. For density filtering using a weighted mean average approach, according to Sigmund [2007] values between $20\% < M_{\text{ND}} < 25\%$ can be expected.

2.5. Objective functions and constraints in context of optical analysis

With the aim of improving the optical performance of a system, performance measures can be added in the form of an objective or constraint. Objective functions in topology optimization are generally minimised, meaning that the aim of the optimizer is to configure design variables in such a way that the objective attains an ever decreasing value in subsequent iterations. The constraint is usually represented in *negative null form*, for the optimizer this represents a value that must not exceed zero.

Optics has two archetypal performance measures. The most basic one is surface flatness, captured by minimising the surface deformations, and the second, more encompassing one is to represent the objective as a series of Zernike polynomials [Genberg, 1984]. This latter method allows for precise tuning of the light path and wavefront aberrations, but at a computational cost. First, least squares is applied through the surface deformations, thereafter, this is translated into Zernike polynomial coefficients.

Both methods can be described by a single response by taking a version of the mean square error (MSE). This is quite a powerful method of describing a multitude of factors in one single variable. One can minimise the error between a point and a predefined displacement, or make this error iteration dependent, such as taking the error between a point and the mean of a collection of points. The latter does however introduce a shifting objective with each iteration of the optimization, as each optimization iteration produces a new density distribution which in turn influences the surface deformations. The MSE is given as:

$$\mathrm{MSE} = \frac{1}{m} \sum_{j=1}^{m} (x_j - \bar{x}_j)^2 \tag{2.13}$$

where x_j is a quantity to be optimized. This could be a node displacement but also a coefficient of a Zernike polynomial. $\bar{x}_j$ is the desired value of said quantity, e.g. for a mean value then $\bar{x}_j = x_{\mathrm{avg}} = \frac{1}{m}\sum_{j=1}^{m} x_j$. Entries with large errors are penalised more severely by means of taking the square. This MSE in essence lays the optimizer's focus on a configuration that has the lowest possible average squared error. The MSE can be expanded to take a certain number of coefficients of Zernike polynomials into account with respect to desired values. The Zernike polynomial coefficients can also be optimized using a multi-objective optimization technique, which attaches weighting factors to each coefficient thereby tuning the focus of the optimizer.

Both of these methods can also be introduced as a constraint or a list of constraints, and therefore become performance thresholds that must be met but need not be improved past the prescribed value. For Zernike polynomials this has been done by Sahu et al. [2017] with the objective of reducing mass for space telescopes. Furthermore, constraints can be added to meet performance criteria that are not directly related to the optics, such as a mechanical compliance constraint to avoid structures with very high compliance which can occur in thermo-elastic optimization [Deaton and Grandhi, 2013], a thermal resistance constraint to control temperature gradients and a pressure drop constraint to prevent highly complex channel layouts. It is not common-place to apply mechanical or thermal compliance constraints. Usually these are used as objective functions. However, as a means to more easily interchange between their use as objectives or constraints this has been considered convenient. The use of compliance-based responses is also a computationally attractive method as they involve self-adjoint problems. This means that no additional solve is required in the adjoint sensitivity analysis, which lowers computational cost.

2.6. Research choices

A one-way coupled thermo-mechanical model will be used to depict the thermal conduction, elastic deformation and thermal expansion of the solid. The reverse coupling term is not used because it recovers thermal energy from deformation rates in time. Being a transient effect this cannot be captured in the steady state. Furthermore, the thermal contribution of these deformations only becomes interesting to capture in the model with slender structures commonly used on satellites in space.

The advection-diffusion model will be used to model the heat transfer between the solid and fluid, including the thermal field of the fluid itself. Although some other methods exist to model the solid-fluid thermal interaction (mainly parametric methods), most if not all past research on topology optimization appears to have used this formulation.

Fluid flow is modelled by the viscous dominated Stokes flow. Stokes flow modelling as shown in Figure 2.2a, produces similar results to Navier-Stokes in topology optimization for quite a range of low Reynolds numbers as seen in Figure 2.2b. Therefore assuming a low Reynolds number one can avoid having to solve the full Navier-Stokes equations.

The material properties of both the solid and fluid will be scaled using the RAMP method. This is mainly due to the theoretical advantage of not having a zero gradient when the material is void. Although the void material never quite reaches zero material, as a minimum density $\rho_{\text{min}} > 0$ is required to prevent the optimization from becoming unstable, the gradients of the SIMP method are theoretically still slightly more advantageous.

The optimizer used will be the MMA due to its applicability to multi-physics problems and non-linear objectives and constraints. An added benefit of the MMA, is that it has been tried and tested extensively, which is reflected in the amount of literature on the method.

A density filter will be applied to the design variables in order to prevent features such as checkerboarding from occurring. This will require the sensitivities to be corrected to accommodate the density filter. Other filters can later replace or be added to the density filter to improve optimizer performance or encourage certain design attributes.

Surface flatness, which in this research will be the optical performance measure, can be characterised using the MSE. The MSE will be used to calculate the error between a deformation and the mean of the deformations (which could potentially be expanded to be a predefined shape or curve). This formulation characterises the average deformation error, which itself is not a commonly used optical performance metric. Errors in optics are normally associated with respect to a Zernike polynomial. This research will however assume that a flat mirror is sought after, subject to a thermal load. Where, if large imbalances in the deformation error occur, the power (from $[\cdot]^2$ to for example $[\cdot]^3$) could be raised.

3

Thermo-mechanical based optimization

In this chapter topology optimization is performed on a thermo-mechanical structure. First the optimization domain will be introduced whereby the different sub-domains and boundaries are treated. Thereafter two different models will be given for comparison, both sharing the same governing equations. Figure 3.1 provides a basic understanding of the elements being covered in this chapter. Three different optimization problems will then be defined which test the influence of certain constraints on the model and the objective function. The constraints implemented are used to promote designs with better mechanical and thermal compliance. This is done for two reasons:

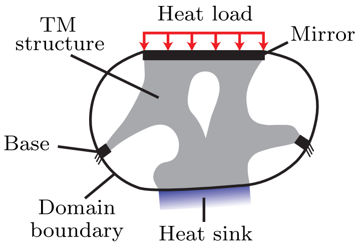

Figure 3.1: Interpretation of the modelling elements in this chapter.

- Preliminary testing has shown that the optimizer tends to designs in which the mirror is uncoupled from the thermal sinks and mechanical supports. Such free-floating mirrors are free to expand while staying flat when heated, but impossible to implement in practice. The influence of including the mechanical and thermal compliance constraints are shown in Section 3.2.2.

- These compliance constraints provide computationally "cheap" control of thermal and mechanical aspects of the final design, due to no extra solves needing to be performed. As extra physics is added to the model in the subsequent chapters, it may become necessary to control these two aspects to attain certain feasible design characteristics.

The intention of this chapter is therefore to attain improved thermo-mechanical structures for mirrors using the aforementioned compliance constraints, where the final design can be controlled by the mechanical and thermal compliance constraints.

This chapter should be seen as a building block for the following chapters where the aim is to tune the thermal and mechanical compliance constraints to not only compare the two constraints but also to gain a preliminary understanding of what parameters improve the problem bounding and speed of convergence; and what problem formulation and structural features contribute to good surface deformation performance.

3.1. Thermo-mechanical domain and model definition

The reference model, given in Figure 3.2, has been chosen to compare converged designs in this chapter and their evolution in the chapters proceeding. The model given in Figure 3.2 consists of a temperature and a displacement field attributed as follows: sub-domain j in Ω_j^t and Ω_j^u respectively. The white region enclosed by the boundaries in Figure 3.2, Ω_{opt}, is the sub-domain to be optimized. Black regions represent the sub-domains Ω_{mirror} and Ω_{base} which are set at full material ($\rho = 1$ in $\Omega_{\text{mirror}} \cup \Omega_{\text{base}}$) throughout the optimization.

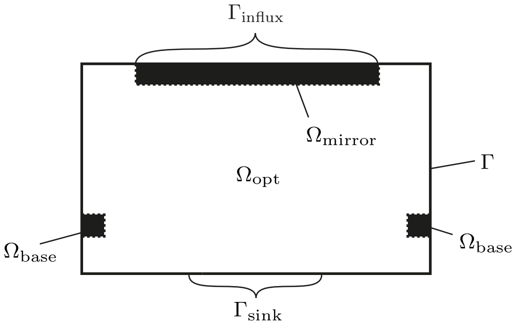

Figure 3.2: Domain designation of thermo-mechanical model. Here Ω_j represents the sub-domain j and Γ_j represents the boundary j. Where $\Omega = \{\Omega_{\text{opt}} \cup \Omega_{\text{mirror}} \cup \Omega_{\text{base}}\}$ and $\Gamma \supseteq \{\Gamma_{\text{influx}}, \Gamma_{\text{sink}}\}$.

The partial differential equation (PDE) which applies to the thermal domain Ω^t is:

$$-\nabla \cdot (k \cdot \nabla \theta) = Q \quad \text{in}\, \Omega^t \tag{3.1}$$

where k is the conductivity and $\theta = T - T_{\text{ref}}$ the relative temperature with respect to a chosen reference temperature (such as ambient temperature) and Q the rate of internal or volumetric heat generation make up the thermal energy balance. The displacements in this model arise directly from mechanical loads and indirectly from the temperature field which produces thermally induced mechanical strains. The latter is calculated from the temperature field θ and when combined with Hooke's law ($\boldsymbol{\sigma} = \mathbf{H}\boldsymbol{\varepsilon}$) gives the mechanical strains $\boldsymbol{\varepsilon}$:

$$\boldsymbol{\varepsilon} = \mathbf{H}^{-1}\boldsymbol{\sigma} + \boldsymbol{\alpha}\theta \quad \text{in}\, \Omega^u \tag{3.2}$$

where $\mathbf{H}$ is Hooke's matrix (also called the stiffness tensor), $\boldsymbol{\sigma}$ the stress vector and $\boldsymbol{\alpha}$ the thermal expansion matrix. The thermal flux, normal to the boundary is given as:

$$q = -k\mathbf{n} \cdot \nabla \theta \quad \text{on}\, \Gamma^t \tag{3.3}$$

where $\mathbf{n}$ is the vector normal to the surface.

The stress field normal to the boundary is given by:

$$\mathbf{t} = \mathbf{n} \cdot \boldsymbol{\sigma} \quad \text{on}\, \Gamma^u \tag{3.4}$$

where $\mathbf{t}$ are the applied tractions.

Each node in the FE mesh contains one temperature degree of freedom (DOF) and a displacement DOF for each spatial dimension. These equations are discretised in Appendix A.1 and given in matrix form in Equations A.7 and A.8.

Two modelling choices have been made which will affect the resulting density distributions' symmetry:

- Firstly: an unstructured mesh has been used which can be a contributing factor to the non-symmetrical designs. For more complicated models, the likelihood of an unstructured mesh being used would increase.
- Secondly: the full domain has been optimised. In the literature study many of the examples found (especially large scale examples) leverage symmetry anywhere possible. Therefore only half and sometimes even quarter domains are optimized meaning that the symmetry lines in 2D and surfaces in 3D have special boundary conditions allowing for the optimization to recognise the boundary as a reflection of the optimized surface. Future chapters will contain an inherent asymmetry therefore a symmetrical approach was not sought.

In the next two sub-sections (Sections 3.1.1 and 3.1.2) the models are introduced which are used in this chapter to study the mechanical and thermal compliance constraints.

3.1.1. Co-located mechanical and thermal sinks

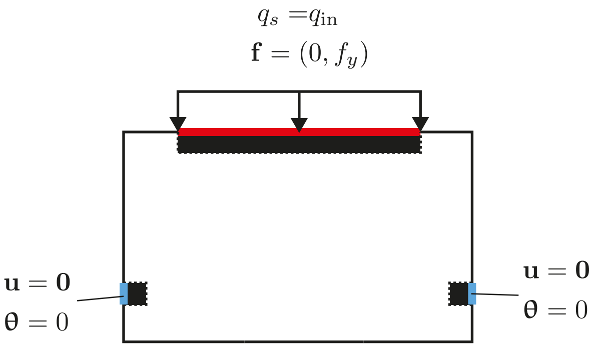

Figure 3.3: "Co-located" model where the heat sinks and fixed points are both located at the base Ω_{base}.

Figure 3.3 shows the distributed thermal load ($q_s = q_{\text{in}}$) and heat sink ($\theta = 0$) for the temperature field and also the uniform distributed mechanical load ($\mathbf{f} = (0, f_y)$) and fixed points ($\mathbf{u} = \mathbf{0}$) for the displacement field. Both the thermal and mechanical load occur at Γ_{influx}.

As the thermal and mechanical loads both occur from the same boundary Γ_{influx} and the thermal sink and mechanical fixed points are "co-located" the boundary conditions overlap. The aim here is to see the different density distributions of a mechanically stiff system to one that is thermally very conductive on this "overlapped" system. Model dimensions and parameters are given in Appendix C.

3.1.2. Separated mechanical and thermal sinks

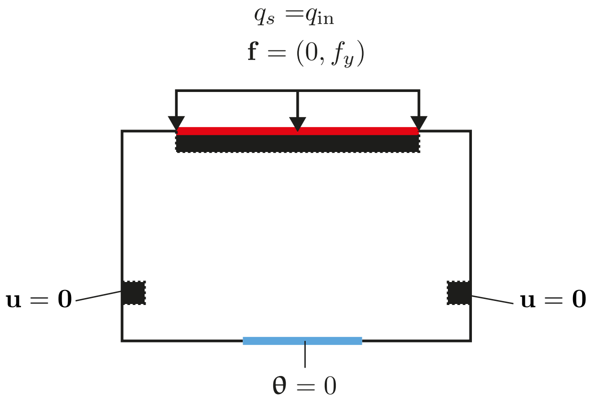

Figure 3.4: "Separated" model where the heat sink is located at Γ_{influx} and fixed points are located at the base Ω_{base}.

Figure 3.4 shows a similar configuration to that in Section 3.1.1 however the thermal sink is now located at the bottom of the domain at Γ_{sink}. Separating the mechanical base and thermal sink allows the final design to be steered towards a stiffer mechanical design or one of better thermal conductance. Model dimensions and parameters are given in Appendix C.

3.1.3. State equations

In this research it is assumed that the system is *one-way coupled*, i.e.: only the effect of temperature induced displacements are taken into account and not the displacement induced temperature variations (a transient effect). The effect of the coupling term is of great importance as this is the primary source of deformation of the structure and not the applied force **f** (used for the purpose of activating the mechanical compliance constraint). The general FE derivation can be found in Zienkiewicz and Taylor [2013], however the matrix notation of the one-way coupled thermo-mechanical relationship from Rixen [2011] is used. The discretised steady state thermo-mechanical state equations are therefore:

$$\begin{bmatrix}\mathbf{K}_\mathrm{D} & 0\\ -\mathbf{A} & \mathbf{K}_\mathrm{U}\end{bmatrix}\begin{bmatrix}\theta\\ \mathbf{u}\end{bmatrix}=\begin{bmatrix}\mathbf{q}\\ \mathbf{f}\end{bmatrix} \tag{3.5}$$

where $\mathbf{K}_\mathrm{D}$ is the diffusivity (conductivity) matrix, $\mathbf{A}$ a matrix containing the thermal expansion relation, $\mathbf{K}_\mathrm{U}$ the mechanical stiffness matrix, $\mathbf{q}$ the thermal flux and $\mathbf{f}$ the mechanical force. The degrees of freedom are θ (the relative temperature) and $\mathbf{u}$ (the displacements).

3.1.4. Material penalisation and interpolation

Penalisation helps the optimizer converge to discrete ($\rho = \rho_\mathrm{min}$ or $\rho = 1$) density distributions. The physical material density (ρ_i) is calculated using the RAMP function given in Equation 2.11, whereby the design variables s_i are given as input. This penalisation is applied to the interpolation of the density in the element routines of each system matrix during the finite element (FE) assembly by multiplying the element matrix with the penalisation term as shown by Bendsoe and Sigmund [2003]; Hooijkamp et al. [2014]. The element stiffness, diffusion and thermal expansion matrices for element i subsequently become:

$$\mathbf{K}_\mathrm{U}^i=\rho_i\mathbf{K}_\mathrm{U}^0 \quad \mathbf{K}_\mathrm{D}^i=\rho_i\mathbf{K}_\mathrm{D}^0 \quad \mathbf{A}^i=\rho_i\mathbf{A}^0 \tag{3.6}$$

where the superscript "0" represents the full material element matrix.

3.2. Optimization problem definition

Figure 2.5 shows a typical optimization loop. Whereas in the previous section (3.1) where the characteristics pertaining to the FEA step are covered, this section will concentrate on the following optimization aspects: the objective and constraints, adjoint sensitivities and filtering techniques.

3.2.1. Objective function

Surface flatness of the mirror is characterised using the mean square error given in Equation 2.13. Where the error taken is in relation to the mean of a set of vertical displacements which characterise the surface flatness. Care must be taken in selecting coherent displacement DOFs, that is to say that the DOF set must only contain DOFs pertaining to the same displacement component. It is assumed that the mean displacement $\bar{x}_j$ of the mirror is not of importance compared to the MSE of the mirror surface, i.e. rigid body displacements can be compensated by other means.

For scenarios where the objective function improves by orders of magnitude it may be necessary to take the logarithm of the current objective formulation. This is due to large differences in the objective and constraint values affecting the performance when using MMA optimizers [Svanberg], but is possibly a wider issue with gradient-based methods. This is achieved as follows:

$$f_\mathrm{log}=\log_{10}\left(C\frac{1}{m}\sum_{j=1}^{m}(x_j-\bar{x}_j)^2+1\right) \tag{3.7}$$

where we introduce the scaling constant C which is the value of the objective function at the first optimization iteration $C = 1/f_0$ and add "1" inside the logarithm to prevent the gradients tending to infinity. Introducing this term prevents the optimizer from being caught out by the very steep ($\frac{\partial f_\mathrm{log}}{\partial f}\approx\infty$) or very flat ($\frac{\partial f_\mathrm{log}}{\partial f}\approx 0$) gradients in the logarithmic function and prevents results that converge to a higher point than the initial value.

Adjoint sensitivities

Using the method set out by Haftka [1981] an adjoint problem can be derived using the following formulation:

$$f^*=f+\lambda_1^\top\left(\mathbf{K}_\mathrm{D}\theta-\mathbf{q}\right)+\lambda_2^\top\left(\mathbf{K}_\mathrm{U}\mathbf{u}-\mathbf{A}\theta-\mathbf{f}\right) \tag{3.8}$$

where λ_1 and λ_2 are the system adjoints. The adjoint sensitivities are therefore given as:

$$\frac{\partial f^*}{\partial s_i} = \lambda_1^\top \frac{\partial \mathbf{K}_\mathrm{D}}{\partial s_i}\theta + \lambda_2^\top \left(\frac{\partial \mathbf{K}_\mathrm{U}}{\partial s_i}\mathbf{u} - \frac{\partial \mathbf{A}}{\partial s_i}\theta\right) \tag{3.9}$$

The full derivation can be found in appendices B.1 and B.2. The adjoints λ_1 and λ_2, which are system vectors with dimensions equal to the temperature and displacement fields, are calculated by solving:

$$\begin{bmatrix} \mathbf{K}_\mathrm{D}^\top & -\mathbf{A}^\top \\ \mathbf{0} & \mathbf{K}_\mathrm{U}^\top \end{bmatrix} \begin{bmatrix} \lambda_1 \\ \lambda_2 \end{bmatrix} = \begin{bmatrix} \mathbf{0} \\ -\frac{\partial f}{\partial \mathbf{u}} \end{bmatrix} \tag{3.10}$$

where the term $\frac{\partial f}{\partial \mathbf{u}}$ is taken from the chain rule: $\frac{\partial f}{\partial s_i} = \frac{\partial f}{\partial \mathbf{u}}\frac{\partial \mathbf{u}}{\partial s_i}$, which are the sensitivities of the objective function with respect to the deformations $\mathbf{u}$.

3.2.2. Constraints

Three constraints are applied to the optimization problem: a maximum volume constraint and maximum mechanical and thermal compliance constraints.

- Maximum volume constraint: this constraint caps the maximum volume fraction taken up by the structure as a fraction of the total volume.
- Maximum mechanical compliance constraint: this limits the compliance of the mechanical structure, producing "stiffer" designs.
- Maximum thermal compliance constraint: this limits the effective resistance of the structure producing thermal designs with at least a certain effective conductance.

All constraints are presented in negative null form as shown in Papalambros and Wilde [2010]. Formulating the constraints in negative null form scales their values equally, whereby their relative weight is equally prominent in the optimization algorithm. This prevents certain constraints from overshadowing others due to their higher relative values.

Setting a severe maximum to a constraint (which reduces the design space drastically) can render another constraint redundant (inactive) or infeasible. Constraints however can help the objective function to converge by reducing the design space, this reduces the number of possible solutions (and possible local minima). However, constraints can add non-convexity to the design space, meaning that the optimizer would have to pass through infeasible regions to reach the global (or a better local) optimum.

The constraint sensitivities of the mechanical and thermal compliance constraints, like the surface deformation objective, are those of the adjoint problem which are derived in Appendix B.

Volume constraint

The volume constraint is given by:

$$g_1 = \frac{\sum_i V_i \rho_i}{V V_{\mathrm{frac,max}}} - 1 \leq 0 \tag{3.11}$$

where V is the total volume of the domain, and V_i and ρ_i the volume and density of element i. The maximum volume fraction is given by $V_{\mathrm{frac,max}}$, which takes a value between $0 \ll V_{\mathrm{frac,max}} \leq 1$. The volume constraint helps the optimizer converge more quickly, meaning that density distributions with a large amount of grey regions can be improved by reducing the permissible volume fraction. In combination with the RAMP penalisation term, the volume constraint makes the optimizer consider grey regions as inefficient use of material.

The sensitivities are calculated as follows:

$$\frac{\partial g_1}{\partial \rho_i} = \frac{V_i}{V V_{\mathrm{frac}}}. \tag{3.12}$$

The sensitivities of the volume constraint are therefore constant with respect to the element volume size.

Mechanical compliance constraint

Mechanical compliance is given by:

$$c_u = \mathbf{u}_\mathrm{m}^\top \mathbf{K}_\mathrm{U} \mathbf{u}_\mathrm{m} \tag{3.13}$$

where $\mathbf{u}_\mathrm{m}$ are the mechanically induced deformations (without the thermo-mechanical contribution), calculated by $\mathbf{u}_\mathrm{m} = \mathbf{K}_\mathrm{U}^{-1}\mathbf{f}$. A minimum mechanical compliance can be applied as follows:

$$g_2 = \frac{\mathbf{u}_\mathrm{m}^\top \mathbf{K}_\mathrm{U} \mathbf{u}_\mathrm{m}}{c_\mathrm{u,max}} - 1 \leq 0 \tag{3.14}$$

forcing the mechanical structure to take on a configuration at least as stiff as $c_\mathrm{u,max}$. $\mathbf{u}_\mathrm{m}^\top \mathbf{K}_\mathrm{U} \mathbf{u}_\mathrm{m} = \mathbf{u}_\mathrm{m}^\top \mathbf{f}$ is actually the mechanical work done by the structure and by implying that it must remain under the threshold $c_\mathrm{u,max}$, forces the optimizer to choose a stiffness configuration $\mathbf{K}_\mathrm{U}$ that reduces $\mathbf{u}$ by minimising the product $\mathbf{u}_\mathrm{m}^\top \mathbf{K}_\mathrm{U} \mathbf{u}_\mathrm{m}$. The sensitivities of the mechanical compliance constraint are given as follows:

$$\frac{\partial g_2}{\partial \rho_i} = -\frac{1}{c_\mathrm{u,max}} \mathbf{u}_\mathrm{m}^\top \frac{\partial \mathbf{K}_\mathrm{U}}{\partial s_i} \mathbf{u}_\mathrm{m} \tag{3.15}$$

where the full derivation is found in Appendix B.5. The mechanical compliance problem is self-adjoint, which means that no additional solve is needed to obtain the adjoint state.

Thermal compliance constraint

Thermal compliance is given by $c_t = \theta^\top \mathbf{K}_\mathrm{D} \theta$. A minimum thermal compliance can be applied as a constraint as follows:

$$g_3 = \frac{\theta^\top \mathbf{K}_\mathrm{D} \theta}{c_\mathrm{t,max}} - 1 \leq 0 \tag{3.16}$$

where it functions similar to the mechanical compliance constraint, only here the thermal resistance is considered. By lowering $c_\mathrm{t,max}$, the maximum temperature gradient is reduced across the system by allowing heat to more easily propagate through the thermal structure. The sensitivities of the thermal compliance constraint are given as follows:

$$\frac{\partial g_3}{\partial \rho_i} = -\frac{1}{c_\mathrm{t,max}} \theta^\top \frac{\partial \mathbf{K}_\mathrm{D}}{\partial s_i} \theta, \tag{3.17}$$

where the full derivation is found in Appendix B.5. The thermal compliance problem is also self-adjoint.

Influence of mechanical and thermal compliance constraints on converged design

The mechanical and thermal compliance constraints are applied sequentially in Table 3.1. The "separated" model is used, where the mechanical base is situated at the sides and the thermal heat sink along the bottom of the domain.

When no compliance constraints are present on the mechanical or thermal part of the system, the "top-left" design is the result. Here, the majority of the material present is "grey", in the region between the mirror and the heat sink, and little to no material present between the mirror and the mechanical base. Convergence can be seen to actually worsen throughout the iterations. This formulation is very badly bounded, and even after an extended amount of iterations (1200 as opposed to 550) convergence continues to deteriorate. This focus of the optimizer is exclusively to reduce the MSE of the surface deformations, meaning that the temperature field due to the thermal structure is not considered in the objective function similar to the displacements (excluding the surface deformations) of the mechanical structure not being considered in the objective function either.

The presence of a thermal compliance constraint shown on the "top-right" shows the improvement of the structure in conducting heat from the mirror surface to the heat sink. However, the structure doesn't appear to gain any mechanical performance. Unlike with the "bottom-left" where only the mechanical compliance constraint is used showing a definite improvement in the mechanical performance. Convergence is improved by including the individual mechanical and thermal compliance constraints in the optimization problem seen in the corresponding convergence plots. The mechanical compliance plot appears to be more critical compared to the thermal compliance when only considering the final objective value. Separation between

Table 3.1: Comparison of the influence of the mechanical and thermal compliance constraints. Optimization problem 2 (described in further detail in Section 3.3.2) is used to minimise the surface deformations of the mirror surface under the constraint of a maximum volume fraction of $V_{\text{frac,max}} = 0.55$. The mechanical and thermal compliance constraints are implemented interchangeably to produce an overview of their effect. When implemented, the constraints take on the values: $c_{\text{u,max}} = 2.25 \times 10^{-6}$ and $c_{\text{u,max}} = 1.00 \times 10^{-4}$ which are stiffer and more conductive than the configuration of the initial optimization step. Adjacent to the density distributions is a plot of the objective function convergence.

		Thermal compliance	
		OFF	ON
Mechanical compliance	OFF	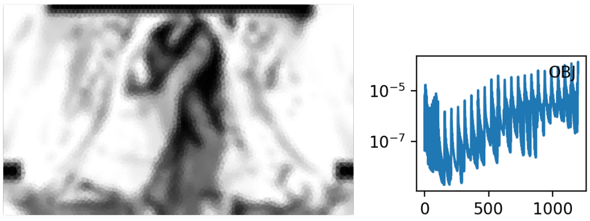	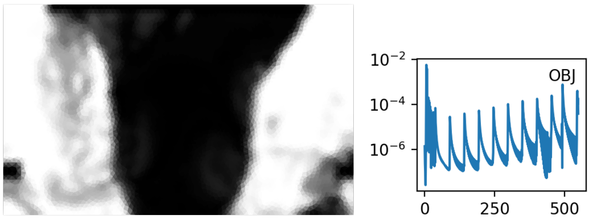
	ON	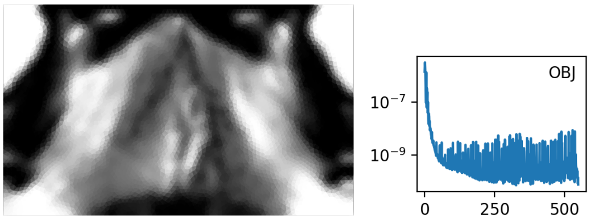	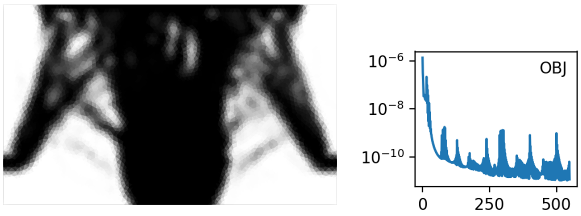

the mechanical and thermal fields is clearly seen: the mechanical compliance constraint has little influence on the thermal system, as it would readily allow temperatures to rise significantly by not conducting heat to the thermal boundary constraint (due to a weak thermal connection). The same can be said for the the thermal compliance constraint, which does not improve the overall structural deformations brought upon by mechanical loading (due to a weak mechanical connection).

It is however clear that convergence is best met by activating both constraints as seen in the "bottom-right" structure. Clearer structures are formed that provide both a given mechanical and thermal compliance performance. Objective convergence also shows a definite improvement, likely due to the improved bounding of the design space. The resulting structure is heavily dictated by the location of the boundary conditions.

Combining the location of the mechanical and thermal boundary conditions would not have the independent effect of the mechanical and thermal structures seen in Table 3.1. The mechanical and thermal structures would as a result of combining the location not be separated. This would be reflected in the dominant compliance constraint largely dictating the shape of the final structure.

3.2.3. Filter application to the topology optimization

The filtered densities (taken from Sigmund [2007]) are calculated as follows:

$$\hat{\rho}_e = \frac{\sum_{i \in N_e} w(\mathbf{x}_i) V_i s_i}{\sum_{i \in N_e} w(\mathbf{x}_i) V_i} \tag{3.18}$$

here i represents the neighbouring elements N_e to element e, $w(\mathbf{x}_i)$ is the weighting function on coordinates $\mathbf{x}_i$ of the element centre, V_i the element volume and s_i the design variable.The filter attributes a weighted average of the density values of bordering elements to each element [Bruns and Tortorelli, 2001]. The filtering radius is the size of the region where the weighted average is taken from the "baricentre" of the element in question. For the purposes of this research the weighted average sample taken from a radius of 1.1 times the length of the element in question.

For clarity, two different density states are referred to in this research: the "raw" density state, also referred to as the design variable s_i which is the density distribution of the system before applying filters. The "physical" density is the density distribution used in the FEA step of the optimization loop. This is the term given to the density distribution after applying all filters. This chapter only uses one filter on the densities therefore this is sometimes referred to as the filtered densities.

Table 3.2: Sequentially applying filters to the same "separated" optimization problem using topology Optimization problem 3 (shown in3.3.3). The objective is a volume minimisation with surface deformation ($c_{\mathrm{SD,max}} = 1\times10^{-10}\,\mathrm{m}^2$), thermal compliance ($c_{\mathrm{t,max}} = 1.00\times10^{-4}$) and mechanical compliance ($c_{\mathrm{u,max}} = 2.25\times10^{-6}$) constraints. The top row consists of the "raw" density distribution, the second row is the "physical" density distribution. The graphs show the volume fraction (VF as the objective function) where the final volume fraction is given, MSE of the surface deformations (SD) and the measure of non-discreteness (M_{ND}) over 550 iterations. Values in the graph are the final values of the optimization, where the MSE of the surface deformations is the average of the final five iterations.

	1. No filtering	2. Density filtering
"Raw" density distribution s_i	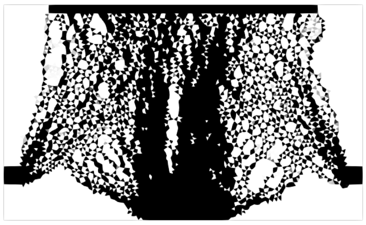	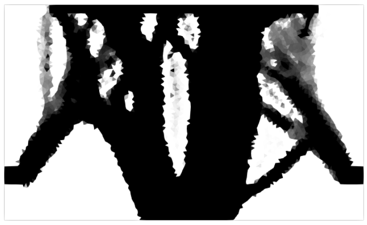
"Physical" density distribution $\hat{\rho}_i$	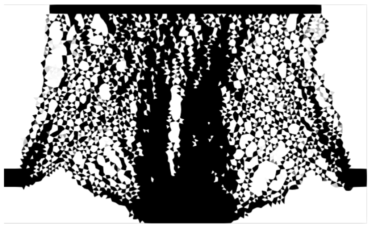	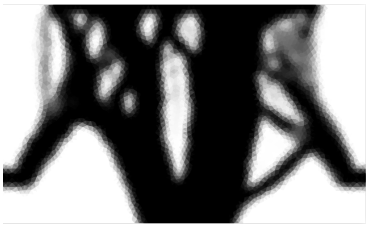
Graph	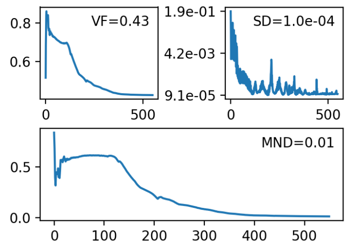	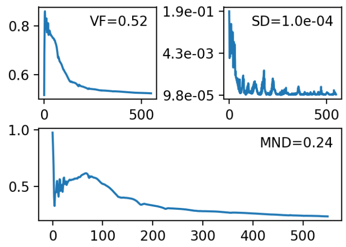

To gain the correct sensitivities after the FEA step, the sensitivities of the objective function have to be expressed with respect to the design variables, i.e. $\frac{\partial f}{\partial s_i}$, and not with respect to the filtered densities, $\frac{\partial f}{\partial \hat{\rho}_i}$. This is done by applying the chain rule, which gives:

$$\frac{\partial f}{\partial s_i} = \frac{\partial f}{\partial \hat{\rho}_i}\frac{\partial \hat{\rho}_i}{\partial s_i} \tag{3.19}$$

where the term $\frac{\partial \hat{\rho}_i}{\partial s_i}$ is in fact the filter. Writing this out fully gives [Sigmund, 2007]:

$$\frac{\partial f}{\partial \rho_e} = \frac{\sum_{i\in N_e} w(\mathbf{x}_i)\rho_i \frac{\partial f}{\partial \rho_i}/V_i}{\rho_e/V_e \sum_{i\in N_e} w(\mathbf{x}_i)}. \tag{3.20}$$

As a means of understanding the influence of the filters, the "separated" model given in Section 3.1.2 has been worked out with the optimization problem given in Equation 3.22. This problem is described in Section 3.3.3. In Table 3.2 the columns show the improvement of applying the density filter throughout the topology optimization. There is no difference between the two density distributions in the first column as there is no density filter used in this example, therefore the "raw" and "physical" density distributions are one and the same. In the second column the smoothing effect of the density filter can be seen. Throughout the topology optimization a "raw" version of the densities exist. They are only displayed for reference as their values are not used in the analysis step or in the calculation of the sensitivities.

For clarity: the density filter is applied just before the FEA step in the optimization loop and the sensitivity correction filter (Equation 3.20) is applied just before the optimizer step. The measure of non-discreteness

M_{ND} given in the bottom graph of the bottom row in Table 3.2 is a measure of the grey regions in the density distribution. When no filtering is applied this attains a very favourable value, however the trade-off is clearly seen to be a very porous structure normally referred to as checkerboarding. The smoothing effect of the density filter provides all the edges of the structure with a grey region, acting as an interface between void regions and full material regions.

3.3. Optimization problems

Three different optimization problems are described in this section. Each proceeding problem is an evolution of the formulation to improve convergence of the optimization. Optimization problems 1 and 2 are identical in formulation, the only difference being that in the latter, the maximum permissible volume fraction is tuned for each combination of the mechanical and thermal compliance constraints. Optimization problem 3 uses a volume minimisation formulation to again improve the definition of the final density distribution.

3.3.1. Optimization problem 1: Surface deformation minimisation with a constant volume constraint

The aim of this optimization is to minimise surface deformations whilst being subjected to varying levels of thermal and mechanical compliance constraints. The volume constraint is held constant. This tests how well the penalisation performs when the volume constraint is minimally invasive, and whether the rate of convergence is better in certain examples. The maximum thermal and mechanical compliance values $c_{\mathrm{t,max}}$ and $c_{\mathrm{u,max}}$ have been chosen so as to visually see the effect these values have on the converged design.

The mechanical and thermal compliance is benchmarked by performing an FEA step on a design where the entire domain is seen as solid. The mechanical compliance of both models with full material $\rho_i = 1$ is $c_u = 0.704 \times 10^{-6}$ Nm. The thermal compliance varies because of the size and location of the thermal heat sinks. The "co-located" model has a thermal compliance of $c_t = 0.427 \times 10^{-4}$ WK/m and the "separated" model $c_t = 0.570 \times 10^{-4}$ WK/m. Using this as a reference, the values of the compliance constraint parameters: $c_{\mathrm{t,max}}$ and $c_{\mathrm{u,max}}$ are chosen heuristically. Slightly different values are used for both the "co-located" and "separated" model variants, so as to better show the influence the constraints have on the final design. Optimization problem 1 is given as follows:

$$
\begin{aligned}
\min_{s} \quad & f = \frac{1}{m}\sum_{j=1}^{m}(x_j - \bar{x}_j)^2 \\
\text{s.t.} \quad & \begin{bmatrix} \mathbf{K}_{\mathrm{D}} & 0 \\ -\mathbf{A} & \mathbf{K}_{\mathrm{U}} \end{bmatrix} \begin{bmatrix} \theta \\ \mathbf{u} \end{bmatrix} = \begin{bmatrix} \mathbf{q} \\ \mathbf{f} \end{bmatrix} \\
& g_1 = \frac{1}{V V_{\mathrm{frac,max}}} \sum_i V_i \rho_i - 1 \le 0 \\
& g_2 = \frac{\mathbf{u}_{\mathrm{m}}^{\top} \mathbf{K}_{\mathrm{U}} \mathbf{u}_{\mathrm{m}}}{c_{\mathrm{u,max}}} - 1 \le 0 \\
& g_3 = \frac{\theta^{\top} \mathbf{K}_{\mathrm{D}} \theta}{c_{\mathrm{t,max}}} - 1 \le 0 \\
& \rho_{\min} \le \rho \le 1
\end{aligned}
\tag{3.21}
$$

where the objective is to minimise f with respect to the design variables s, subject to the state equations, constraints and the density limits. Here the volume fraction $V_{\mathrm{frac,max}}$ for the "co-located" system is $V_{\mathrm{frac,max}} = 0.6$ and for the "separated" system $V_{\mathrm{frac,max}} = 0.7$ due to the larger volume needed to span the "separated" heat sink from the base.

3.3.2. Optimization problem 2: Surface deformation minimisation with an active volume constraint

The optimization problem here is the same as in Section 3.3.1 where the surface deformations are being minimised. The thermal and mechanical compliance constraints also cover the same range. However, whereas in the previous example the maximum volume fraction ($V_{\mathrm{frac,max}}$) of the volume constraint was kept constant, here the fraction is varied with each different thermal and mechanical compliance configuration. This is done to improve convergence and the definition of the final design.

The maximum volume fraction, $V_{\text{frac,max}}$ permissible for the "co-located" and "separated" topology optimizations are seen in Tables 3.3 and 3.4. These values were found by iteratively tuning $V_{\text{frac,max}}$. The volume constraint function intersects both the thermal and mechanical compliance constraint functions therefore the aim of the chosen volume fraction is to be low enough to force a black and white density distribution but not so low that a constraint becomes infeasible.

Table 3.3: Maximum volume fraction $V_{\text{frac,max}}$ of "co-located" topology optimization.

	$c_{\text{t,max}} = 0.75 \times 10^{-4}$	$c_{\text{t,max}} = 1.50 \times 10^{-4}$	$c_{\text{t,max}} = 2.25 \times 10^{-4}$
$c_{\text{u,max}} = 0.85 \times 10^{-6}$	0.95	0.95	0.95
$c_{\text{u,max}} = 1.50 \times 10^{-6}$	0.52	0.45	0.45
$c_{\text{u,max}} = 3.30 \times 10^{-6}$	0.50	0.26	0.27

Table 3.4: Maximum volume fraction $V_{\text{frac,max}}$ of "separated" topology optimization.

	$c_{\text{t,max}} = 0.75 \times 10^{-4}$	$c_{\text{t,max}} = 1.00 \times 10^{-4}$	$c_{\text{t,max}} = 1.50 \times 10^{-4}$
$c_{\text{u,max}} = 1.25 \times 10^{-6}$	0.70	0.65	0.65
$c_{\text{u,max}} = 2.25 \times 10^{-6}$	0.65	0.55	0.45
$c_{\text{u,max}} = 3.30 \times 10^{-6}$	0.65	0.52	0.43

3.3.3. Optimization problem 3: Volume minimisation with surface deformation constraint

In an attempt to reduce the grey regions even further, the volume constraint will be removed and introduced as a volume minimisation objective. The surface deformation objective (Equation 3.7) will become a surface deformation constraint where for each variation of the thermal ($c_{\text{t,max}}$) and mechanical ($c_{\text{u,max}}$) compliance values, the same maximum surface deformation $c_{\text{SD,max}}$ is applied. The surface deformation constraint is taken as the logarithm of the MSE where the constant C is calculated in the first optimization iteration just like in Equation 3.7. The volume minimisation is given as follows:

$$\begin{aligned}
\min_{s} \quad & f = \frac{1}{V}\sum_i V_i \rho_i \\
\text{s.t.} \quad & \begin{bmatrix} \mathbf{K}_{\text{D}} & 0 \\ -\mathbf{A} & \mathbf{K}_{\text{U}} \end{bmatrix} \begin{bmatrix} \theta \\ \mathbf{u} \end{bmatrix} = \begin{bmatrix} \mathbf{q} \\ \mathbf{f} \end{bmatrix} \\
& g_1 = \frac{1}{\log_{10}(C c_{\text{SD,max}})} \log_{10}\left(C \frac{1}{m} \sum_{j=1}^{m} (x_j - \bar{x}_j)^2 + 1 \right) - 1 \leq 0 \\
& g_2 = \frac{\mathbf{u}_{\text{m}}^{\top} \mathbf{K}_{\text{U}} \mathbf{u}_{\text{m}}}{c_{\text{u,max}}} - 1 \leq 0 \\
& g_3 = \frac{\theta^{\top} \mathbf{K}_{\text{D}} \theta}{c_{\text{t,max}}} - 1 \leq 0 \\
& \rho_{\text{min}} \leq \rho \leq 1
\end{aligned} \tag{3.22}$$

where g_1 is the surface deformation constraint written in negative null form.

3.4. Results

This section presents the results of the two models previously covered. The "co-located" and "separated" models are described at different states of evolution in the refinement of the topology optimization problem.

For each resulting density distribution (given in Tables 3.6- 3.12) in this section, four graphs are plotted alongside to show the convergence of not only the objective function but also the constraints. Optimization problems 1 and 2 have the same objective function namely the MSE of the surface deformations. In Optimization problem 3 the MSE of the surface deformations becomes a constraint and as opposed to plotting g_1 it is plotted as it is in Optimization problems 1 and 2 for easier comparison of the surface deformation performance. When a constraint is positive it means that the constraint is infeasible, when zero the constraint is active and when negative the constraint is satisfied.

The measure of non-discreteness given in Equation 2.12 of the final optimization iteration is stated alongside each density distribution. As each optimization begins with a starting density of $\rho = 0.5$, the corresponding M_{ND} is 100%. This can be interpreted as a measure of *greyness* where the lower the value the better the optimization problem has converged to a discrete design.

3.4.1. Co-located mechanical and thermal sinks

To benchmark the MSE value, an FEA was performed on a fully solid domain ($\rho_i = 1$). This corresponds with MSE = $0.0112\,\mathrm{m}^2$. Because ρ_i is set to 0.5 in the first optimization iteration, the initial corresponding MSE value of the surface deformations provided in the results of Tables 3.6 and 3.7 is MSE = $0.223\,\mathrm{m}^2$.

Optimization problem 1: Surface deformation minimisation with active volume constraint

Resulting density distributions for when the volume constraint is set at the same value for each configuration are given in Table 3.6 on Page 30.

At first glance it is immediately obvious that there is inherent difference between the results of the top row compared to the bottom two. The top row of results has converged by far to the most discrete (material or void) distribution, this is backed up by their M_{ND} values which are comparatively low. It can also be seen that their convergence according to the objective graph is the steadiest and most immediate, however their improvement is much smaller (less than one order of magnitude) compared to the over four order of magnitude improvements of the bottom two rows. The mechanical and thermal compliance constraints have been met, however it may be of interest to increase the design space by increasing the maximum volume constraint.

The second and third rows have not fully converged, as evident from the high grey fraction by more importantly the objective graph still appears to be falling or oscillating. This "noisy" convergence is in part due to the objective function, that due to the changing value of the mean deformations causes a moving target effect between iterations. A relatively large $V_{\mathrm{frac,max}}$ in the volume constraint does not bound the optimization problem very well. This will be improved in the next optimization problem where the maximum permissible volume fraction is chosen more stringently for each case.

Optimization problem 2: Surface deformation minimisation with active volume constraint

To obtain the correct volume constraint values, an iterative process of tuning $V_{\mathrm{frac,max}}$ is adopted until a certain desired contrast is reached and all constraints are met. The obtained volume fractions are stated in Table 3.3. The top required a significantly volume to achieve an improvement similar in size to the other examples.

What can be seen in Table 3.7 on Page 31 is an immediate improvement in contrast and definition from the density distribution attained in Table 3.6, this can also be seen in the largely improved M_{ND} values. Interestingly, when given a larger volume the top row has gained a fundamentally different design, alongside a much improved final objective value. The last two rows have not attained quite as low an objective within the 550 iterations, however the designs have become more discrete.

The iterative method adopted in order to select the volume fraction for the volume constraint is not a very effective method of constraining the optimization problem. The top right volume constraint graph of each optimization problem shows an almost immediate convergence to the maximum volume fraction. Each combination of compliance constraints requires a minimum volume to satisfy them, due to the tuning of the volume fraction this leads to it rapidly being satisfied.

Rewriting the optimization problem where an explicit surface deformation performance target is seen as a constraint and a volume minimisation as an objective, may force the optimizer to be more "efficient" with material placement. This leverages the material penalisation more effectively. This is therefore done in Optimization problem 3.

Optimization problem 3: Volume minimisation with surface deformation constraint

The results of this case are shown in Table 3.8 on Page 32, where the overall M_{ND} has gained a consistency of lower values over those of Table 3.7. The surface deformation constraint with a maximum MSE of $c_{\text{SD,max}} = 10^{-10}\,\text{m}^2$, allowed almost all the different examples to converge within 550 iterations. With a maximum MSE of $c_{\text{SD,max}} = 10^{-11}\,\text{m}^2$, many of the examples did not fully converge to a discrete design within the 550 iterations, which is why they are not displayed.

The examples that have converged are those that have been most stringently constrained (first row and column), most likely because of the better bounding provided by the thermal and mechanical compliance constraint.

The volume minimisation brought similar designs compared to the previous optimization problem for the first and last row. Interestingly, the second row has converged to an inherently different design, where we see that they all share a similar design. The region beneath the centre of the mirror however has only converged well in the most thermally constrained of the three without penalising the surface deformation.

The last design of the last row shows two "braces" rising from the base to just beneath the mirror surface. This feature hasn't converged to a discrete black and white design, and may be due to the inactive thermal compliance constraint, that after 550 iterations hasn't yet converged.

Discussion

Optimization problem 3 has shown to largely produce more consistent (black and white) convergence than both Optimization problems 1 and 2 in the "co-located" model. Minimising the MSE of the surface deformation is therefore no longer the objective but a constraint. This helps convergence but does not necessarily ensure the best possible optical performance, rather it guarantees a certain minimum by introducing the performance measure as a constraint.

A selection of designs from Optimization problem 3 are plotted in Table 3.5 in order to further analyse their mechanical and thermal performance. The deformations shown in the first column show an increasing vertical displacement and mirror length. There are two reasons for this:

- Increasing the mechanical compliance of a structure produces more slender structures allowing for larger deformations.
- Increasing the thermal compliance of a structure also produces more slender structures allowing for larger temperature gradients due to the increased effective resistance.

The increased temperature difference can be seen in the third column quite clearly at the mirror surface, where the temperature rises due to the thinning structure. This is due to the higher effective resistance associated with a narrower medium shown in the fourth column by the higher temperature gradients reflected in the equation $\nabla T = -q/k$.

The surface deformations of the first and final iteration are shown in the second column. The final attained value of the MSE is $c_{\text{SD}} = 1 \times 10^{-10} m^2$. As the supporting structure beneath the mirror surface becomes more slender the surface gradually becomes more affected by surface oscillations.

The different combinations of compliance constraints provides an interesting overview of different designs and methods to prevent a parabolic mirror deformation. The design in the first row has slits to reduce the rotation which would otherwise produce the parabolic deformation produced in the initial condition. The second and third rows show structures with more of a mechanism design, most likely because of the larger deformation induced by the higher temperatures.

Table 3.5: Table containing a selection of converged designs from the "co-located" model using Optimization problem 3. The deformed and undeformed states have been plotted in column one, the surface deformations of the starting and final designs in the second column, the relative temperature is plotted in column three of regions where $\rho \geq 0.5$ and the final column contains the magnitude of the temperature gradient of regions where $\rho \geq 0.5$.

	Deformed state (×25) ▨ Undeformed ■ Deformed	Surface deformation (m)	Temperature field (K) $\theta = 0$ 0.07	Magnitude of temperature gradient (K/m) $\nabla\theta = 0$ 0.6
MC0.85×10^{-6} TC0.75×10^{-4}	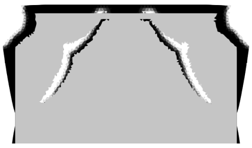	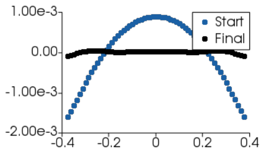	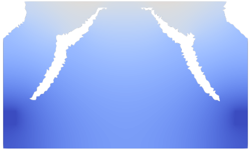	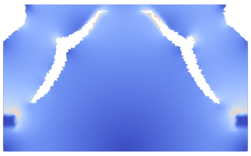
MC1.5×10^{-6} TC0.75×10^{-4}	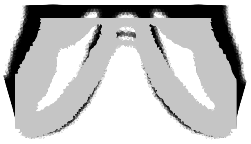	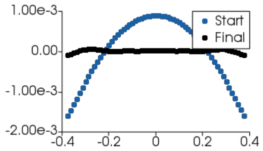	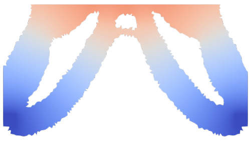	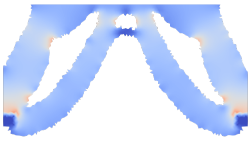
MC3.3×10^{-6} TC1.5×10^{-4}	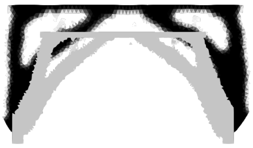	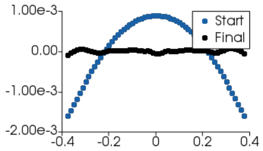	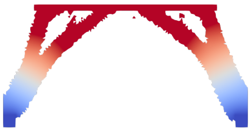	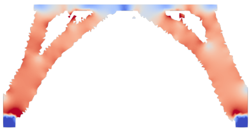

Table 3.6: Comparison of density distributions for varying thermal and mechanical compliance constraints all subject to the same volume constraint. Black regions represent material whereas white areas are voids. The graphs contain the following data: OBJ: Surface deformation objective function (non-scaled MSE), VC: Volume fraction constraint, MC: Mechanical compliance constraint, TC: Thermal compliance constraint, M_{ND}: Measure of non-discreteness of final iteration.

		Thermal compliance (TC)		
		$c_{\mathrm{t,max}} = 0.75 \times 10^{-4}$	$c_{\mathrm{t,max}} = 1.50 \times 10^{-4}$	$c_{\mathrm{t,max}} = 2.25 \times 10^{-4}$
Mechanical Compliance (MC)	$c_{\mathrm{u,max}} = 0.85 \times 10^{-6}$	$M_{\mathrm{ND}} = 0.06$ 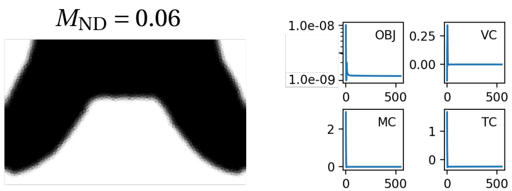	$M_{\mathrm{ND}} = 0.06$ 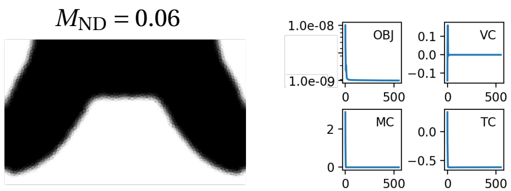	$M_{\mathrm{ND}} = 0.06$ 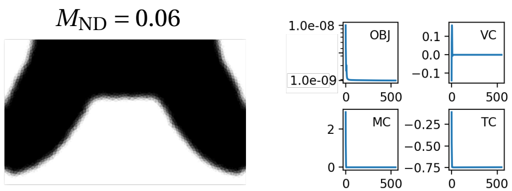
	$c_{\mathrm{u,max}} = 1.50 \times 10^{-6}$	$M_{\mathrm{ND}} = 0.29$ 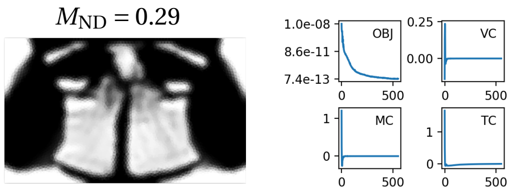	$M_{\mathrm{ND}} = 0.35$ 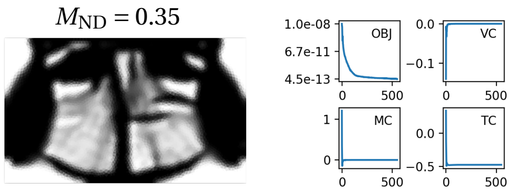	$M_{\mathrm{ND}} = 0.35$ 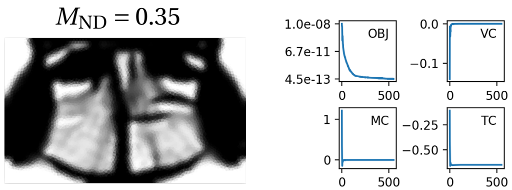
	$c_{\mathrm{u,max}} = 3.30 \times 10^{-6}$	$M_{\mathrm{ND}} = 0.26$ 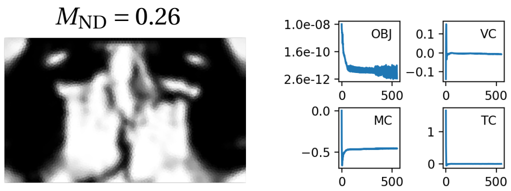	$M_{\mathrm{ND}} = 0.66$ 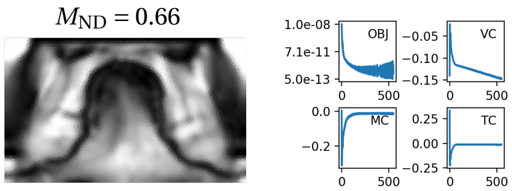	$M_{\mathrm{ND}} = 0.62$ 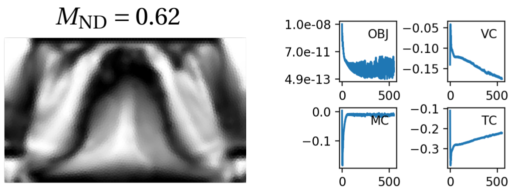

Table 3.7: Comparison of density distributions for varying thermal and mechanical compliance constraints subject to varying volume constraints. Black regions represent material whereas white areas are voids. The graphs contain the following data: OBJ: Surface deformation objective function (non-scaled MSE), VC: Volume fraction constraint, MC: Mechanical compliance constraint, TC: Thermal compliance constraint, M_{ND}: Measure of non-discreteness of final iteration.

		Thermal compliance (TC)		
		$c_{\text{t,max}} = 0.75 \times 10^{-4}$	$c_{\text{t,max}} = 1.50 \times 10^{-4}$	$c_{\text{t,max}} = 2.25 \times 10^{-4}$
Mechanical Compliance (MC)	$c_{\text{u,max}} = 0.85 \times 10^{-6}$	$M_{\text{ND}} = 0.08$ 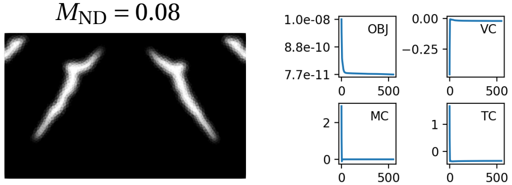	$M_{\text{ND}} = 0.08$ 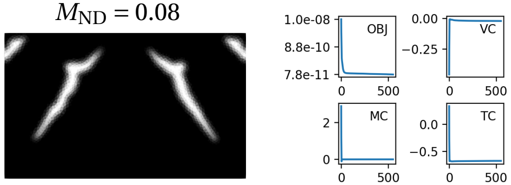	$M_{\text{ND}} = 0.08$ 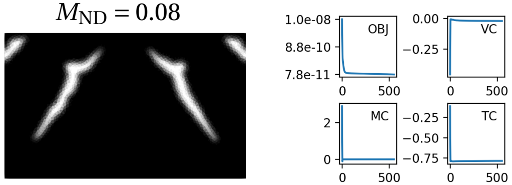
	$c_{\text{u,max}} = 1.50 \times 10^{-6}$	$M_{\text{ND}} = 0.16$ 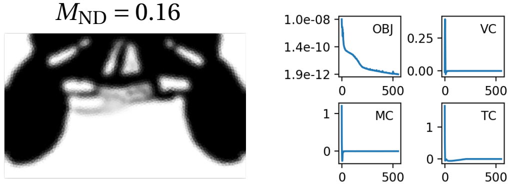	$M_{\text{ND}} = 0.11$ 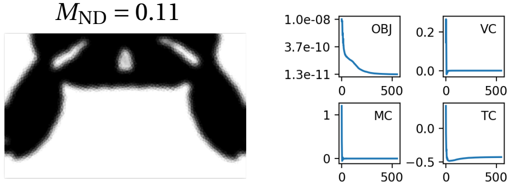	$M_{\text{ND}} = 0.11$ 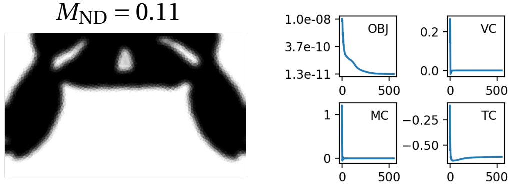
	$c_{\text{u,max}} = 3.30 \times 10^{-6}$	$M_{\text{ND}} = 0.15$ 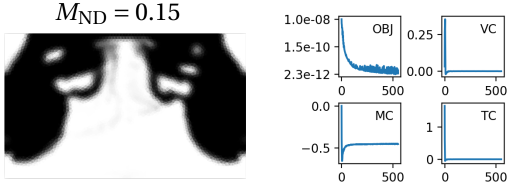	$M_{\text{ND}} = 0.16$ 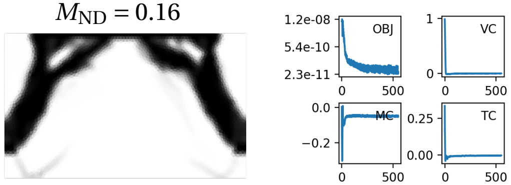	$M_{\text{ND}} = 0.25$ 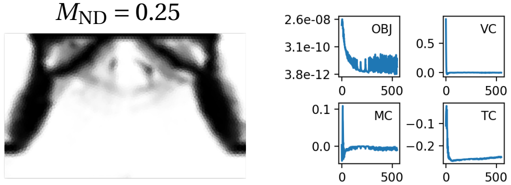

Table 3.8: Comparison of density distributions for varying thermal and mechanical compliance constraints all subject to the same surface deformation constraint. Black regions represent material whereas white areas are voids. The graphs contain the following data: OBJ: Volume minimisation objective function, SD: MSE of surface deformations, MC: Mechanical compliance constraint, TC: Thermal compliance constraint, M_{ND}: Measure of non-discreteness of final iteration.

		Thermal compliance (TC)		
		$c_{\mathrm{t,max}} = 0.75 \times 10^{-4}$	$c_{\mathrm{t,max}} = 1.50 \times 10^{-4}$	$c_{\mathrm{t,max}} = 2.25 \times 10^{-4}$
Mechanical Compliance (MC)	$c_{\mathrm{u,max}} = 0.85 \times 10^{-6}$	$M_{\mathrm{ND}} = 0.08$ 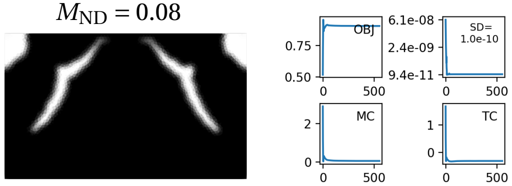	$M_{\mathrm{ND}} = 0.08$ 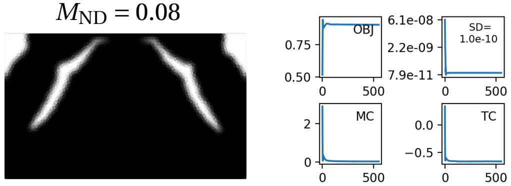	$M_{\mathrm{ND}} = 0.08$ 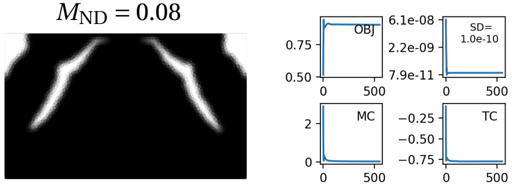
	$c_{\mathrm{u,max}} = 1.50 \times 10^{-6}$	$M_{\mathrm{ND}} = 0.15$ 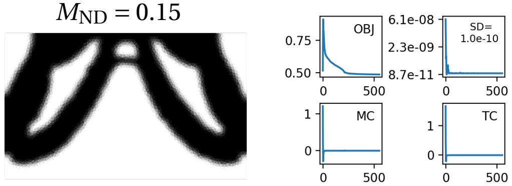	$M_{\mathrm{ND}} = 0.17$ 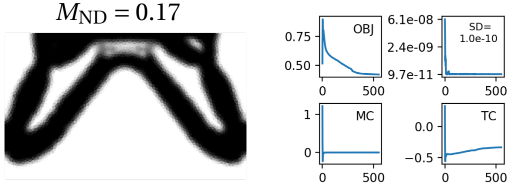	$M_{\mathrm{ND}} = 0.17$ 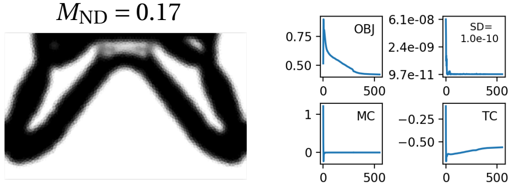
	$c_{\mathrm{u,max}} = 3.30 \times 10^{-6}$	$M_{\mathrm{ND}} = 0.15$ 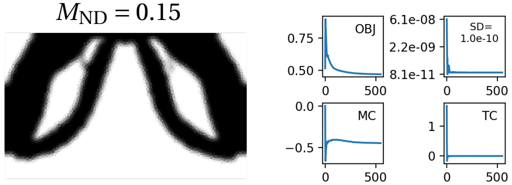	$M_{\mathrm{ND}} = 0.12$ 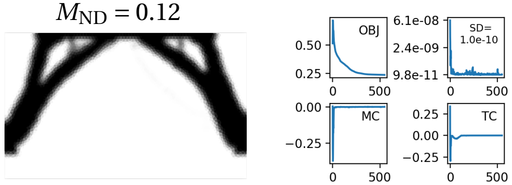	$M_{\mathrm{ND}} = 0.23$ 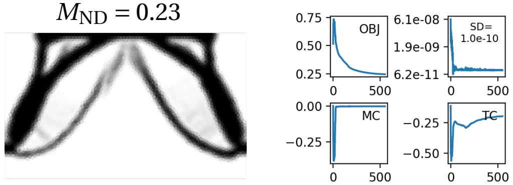

3.4.2. Separated mechanical and thermal sinks

The results in this section are based on the model given in Section 3.1.2 where the heat sink and the base are "separated". Here the results of the optimization problems described in Section 3.3 are shown. The starting value of the MSE of the surface deformation of the "separated" examples is MSE = $0.190\,\mathrm{m}^2$, this corresponds with a starting density of $\rho_i = 0.5$. A fully dense ($\rho_i = 1$) distribution would result in a value of MSE = $0.00978\,\mathrm{m}^2$.

Optimization problem 1: Surface deformation minimisation with active volume constraint

Similar to the "co-located" model results, convergence to a black and white layout is not reliably reached for the "separated" model using Optimization problem 1 as shown in Table 3.10, which is clear from the large M_{ND} values . The only example that converges to a reasonable extent is (TC0.75×10^{-4},MC1.25×10^{-6}). The corresponding graph does show that the objective function has not fully converged which may allow the definition of the density distribution to further improve. Similar to the results given in Table 3.6, this optimization problem appears to need a more stringent volume constraint to converge to a black and white design. This is further reinforced by the objective functions of the last two rows which are very noisy suggesting that there could be bounding issues associated with the current optimization problem.

Optimization problem 2: Surface deformation minimisation with active volume constraint

The volume fraction $V_{\mathrm{frac,max}}$ is again found by iteration, until a volume fraction is found that fulfils all the constraints and that not only provides an acceptable black and white contrast but also allows for a well performing objective function. These volume fractions are given in Table 3.4. The resulting density distributions are shown in Table 3.11, where a definite improvement can be seen in both the definition of the density distribution and convergence of the objective, compared to Optimization problem 1. Whereas the problem previously suffered of noisy convergence of the objective function, this has in part been improved by tailoring the volume constraint to each example.

Unlike in the previous optimization problem, there is a definite sense that optimization is converging to a certain design. The influence of the mechanical compliance constraint can be seen in the length scales of the truss holding the structure to the base, whereas the the thermal compliance constraint can be seen in the varying length scales of the central column connecting the mirror to the heat sink.

Optimization problem 3: Volume minimisation with surface deformation constraint

Table 3.12 shows the different density distributions for Optimization problem 3. The maximum permissible surface deformation has been set at $c_{\mathrm{SD,max}} = 10^{-10}\,\mathrm{m}^2$ like in the previous model. A lower threshold is possible namely $c_{\mathrm{SD,max}} = 10^{-11}\,\mathrm{m}^2$, however not all examples converged within the 550 optimization iterations.

Black and white convergence has been improved upon over the previous two optimization problems based on the M_{ND} value, which has reached lower values than the previous two optimization problems. The bottom-right example has the highest M_{ND}, which is due to the many edges which are all "grey" due to the density filtering.

The effect of the mechanical and thermal compliance constraints is clearly visible: in the left column, the thermal system allows heat flux to pass through easily to the heat sink on the bottom of the domain, whereas on the right, the thermal path is narrower and less direct meaning more thermal resistance is permissible. The top row corresponds to a stiffer mechanical system. The struts holding the structure to the base are thicker therefore it can be expected that the structure deforms less in the vertical direction. The bottom row corresponds to a more mechanically compliant system.

In examples where the objective function still appears to be falling, although the M_{ND} value and amount of grey material are low, it is likely that the boundaries are shifting. This "boundary translation" [Sigmund and Maute, 2013] is a notoriously slow process, for there are no known remedies.

Table 3.9: Table containing a selection of converged designs from the "separated" model using Optimization problem 3. The deformed and undeformed states have been plotted in column one, the surface deformations of the starting and final designs in the second column, the relative temperature is plotted in column three of regions where $\rho \geq 0.5$ and the final column contains the magnitude of the temperature gradient of regions where $\rho \geq 0.5$.

	Deformed state (×25) ▨ Undeformed ■ Deformed	Surface deformation (m)	Temperature field (K) $\theta = 0$ 0.07	Magnitude of temperature gradient (K/m) $\nabla\theta = 0$ 0.6
MC1.25 × 10^{-6} TC0.75 × 10^{-4}	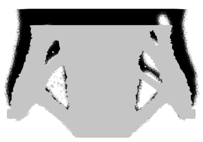	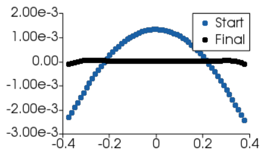	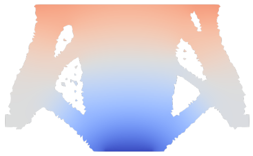	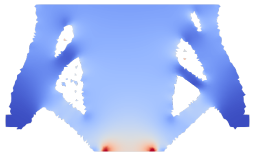
MC2.25 × 10^{-6} TC1.0 × 10^{-4}	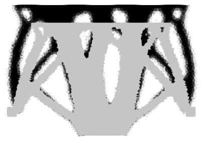	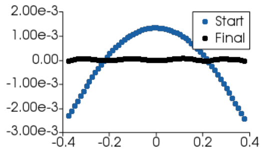	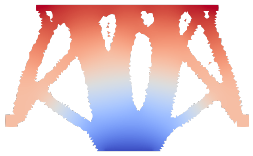	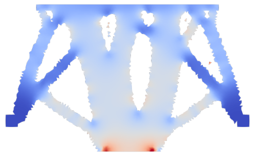
MC3.3 × 10^{-6} TC1.5 × 10^{-4}	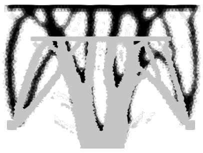	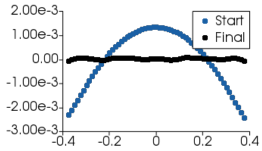	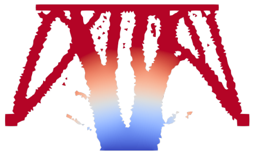	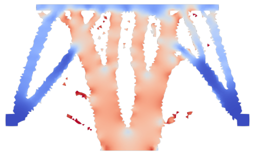

Discussion

Convergence of Optimization problem 3 is in almost all cases better compared to Optimization problems 1 and 2. This is partly due to the reduced MSE requirement, which has been set at $c_{\mathrm{SD,max}} = 10^{-10}\,\mathrm{m}^2$, meaning that the highly sensitive regions beneath the mirror surface can more easily converge. Although reliable convergence is met, surface deformation performance is hindered as a consequence. Optimization problem 2 would therefore be more favourable if the bounding of the design space could be improved, in turn perhaps improving the "boundary translation" problem.

In Table 3.9 a selection of the resulting designs from Optimzation problem 3 are chosen for further analysis with respect to their mechanical and thermal performance.

Similar to in the "co-located" model the largest deformations arise from the examples with the most slender structures. This is mainly due to the higher effective resistance of these structural members causing higher temperature gradients in the system. A warmer mirror surface therefore causes a larger thermal expansion, which again for this model is the upwards "piston" action of the entire mirror structure and to a perhaps less noticeable extent, the elongation of the mirror surface itself.

The surface deformation oscillations are again most prevalent with structures that have less material beneath the mirror surface. Although it must be stated that the MSE requirement was met.

An aspect of the design which can be brought into question can be seen when looking at the mechanical base of each structure in the heat map. The top two examples show struts leaving the bottom of the "thermal column" to the mechanical struts on the side. This results in a relatively low base temperature. This design feature is not shared in the bottom design, where high temperatures are seen at the mechanical base. In precision engineering it may be advantageous to separate the *thermal path* from the mechanical supports to prevent parasitic thermal effects occurring outside this domain. The temperature at the mechanical base may therefore be of interest to constrain for a certain thermal performance.

In the gradient magnitude maps an interesting feature, likely due to modelling deficiencies, can be seen at the extremities of the heat sink. A region of high temperature gradient is seen at each corner of the heat sink, this is more clearly seen in the top two designs, however the bottom design also exhibits this trait. This is most likely due to a FE error modelling the Dirichlet $\theta = 0$ boundary condition.

Table 3.10: Comparison of density distributions for varying thermal and mechanical compliance constraints all subject to the same volume constraint. Black regions represent material whereas white areas are voids. The graphs contain the following data: OBJ: Surface deformation objective function (non-scaled MSE), VC: Volume fraction constraint, MC: Mechanical compliance constraint, TC: Thermal compliance constraint, M_{ND}: Measure of non-discreteness of final iteration.

		Thermal compliance (TC)		
		$c_{\mathrm{t,max}} = 0.75 \times 10^{-4}$	$c_{\mathrm{t,max}} = 1.00 \times 10^{-4}$	$c_{\mathrm{t,max}} = 1.50 \times 10^{-4}$
Mechanical Compliance (MC)	$c_{\mathrm{u,max}} = 1.25 \times 10^{-6}$	$M_{\mathrm{ND}} = 0.19$ 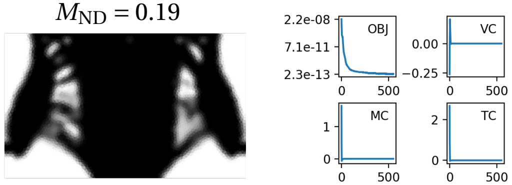	$M_{\mathrm{ND}} = 0.34$ 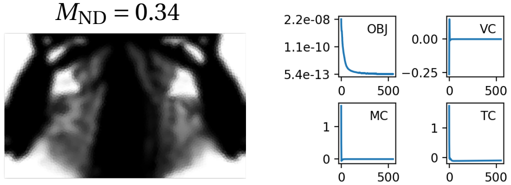	$M_{\mathrm{ND}} = 0.36$ 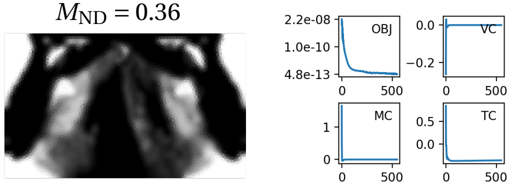
	$c_{\mathrm{u,max}} = 2.25 \times 10^{-6}$	$M_{\mathrm{ND}} = 0.36$ 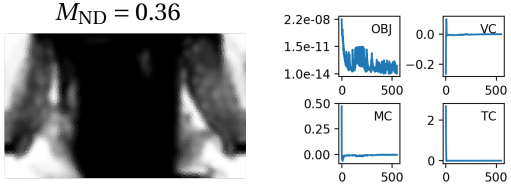	$M_{\mathrm{ND}} = 0.58$ 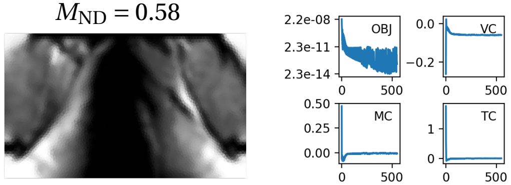	$M_{\mathrm{ND}} = 0.65$ 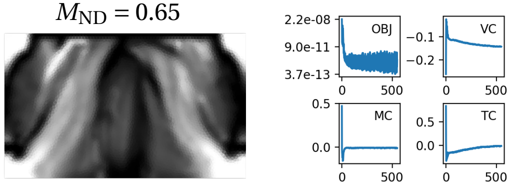
	$c_{\mathrm{u,max}} = 3.30 \times 10^{-6}$	$M_{\mathrm{ND}} = 0.41$ 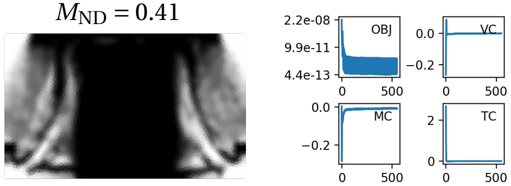	$M_{\mathrm{ND}} = 0.59$ 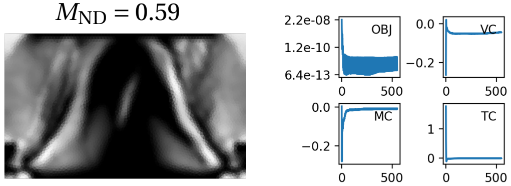	$M_{\mathrm{ND}} = 0.72$ 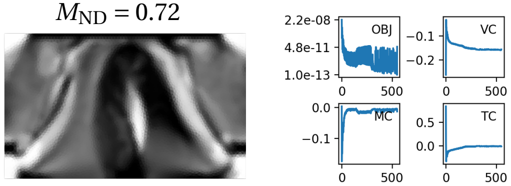

Table 3.11: Comparison of density distributions for varying thermal and mechanical compliance constraints subject to varying volume constraints. Black regions represent material whereas white areas are voids. The graphs contain the following data: OBJ: Surface deformation objective function (non-scaled MSE), VC: Volume fraction constraint, MC: Mechanical compliance constraint, TC: Thermal compliance constraint, M_{ND}: Measure of non-discreteness of final iteration.

		Thermal compliance (TC)		
		$c_{\mathrm{t,max}} = 0.75 \times 10^{-4}$	$c_{\mathrm{t,max}} = 1.00 \times 10^{-4}$	$c_{\mathrm{t,max}} = 1.50 \times 10^{-4}$
Mechanical Compliance (MC)	$c_{\mathrm{u,max}} = 1.25 \times 10^{-6}$	$M_{\mathrm{ND}} = 0.19$ 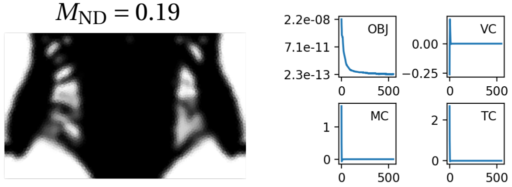	$M_{\mathrm{ND}} = 0.28$ 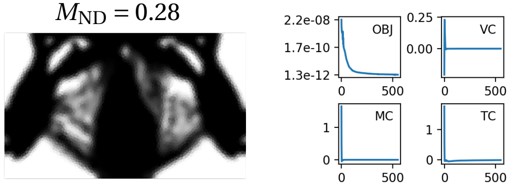	$M_{\mathrm{ND}} = 0.33$ 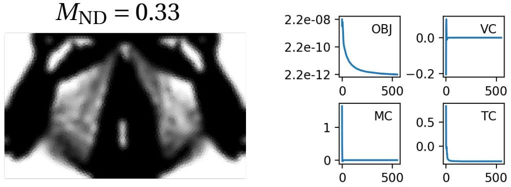
	$c_{\mathrm{u,max}} = 2.25 \times 10^{-6}$	$M_{\mathrm{ND}} = 0.23$ 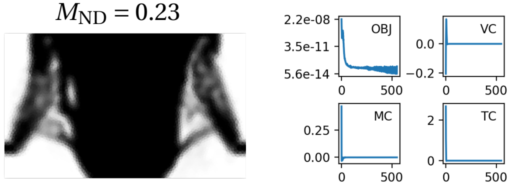	$M_{\mathrm{ND}} = 0.27$ 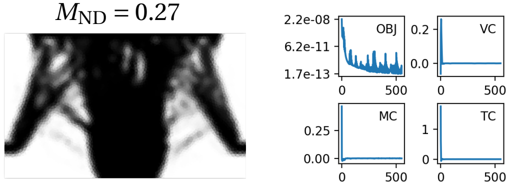	$M_{\mathrm{ND}} = 0.29$ 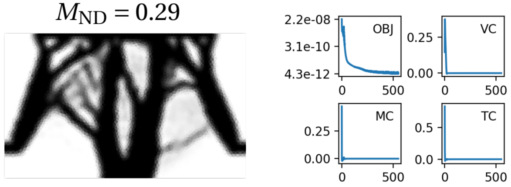
	$c_{\mathrm{u,max}} = 3.30 \times 10^{-6}$	$M_{\mathrm{ND}} = 0.31$ 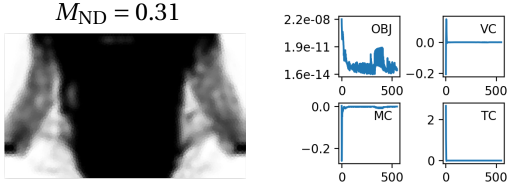	$M_{\mathrm{ND}} = 0.27$ 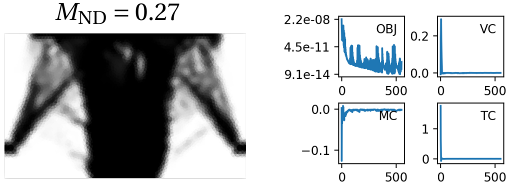	$M_{\mathrm{ND}} = 0.33$ 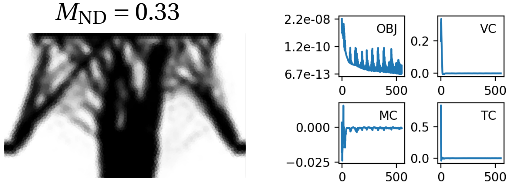

Table 3.12: Comparison of density distributions for varying thermal and mechanical compliance constraints all subject to the same surface deformation constraint. Black regions represent material whereas white areas are voids. The graphs contain the following data: OBJ: Volume minimisation objective function, SD: Surface deformation constraint, MC: Mechanical compliance constraint, TC: Thermal compliance constraint, M_{ND}: Measure of non-discreteness of final iteration.

		Thermal compliance (TC)		
		$c_{\mathrm{t,max}} = 0.75 \times 10^{-4}$	$c_{\mathrm{t,max}} = 1.00 \times 10^{-4}$	$c_{\mathrm{t,max}} = 1.50 \times 10^{-4}$
Mechanical Compliance (MC)	$c_{\mathrm{u,max}} = 1.25 \times 10^{-6}$	$M_{\mathrm{ND}} = 0.14$ 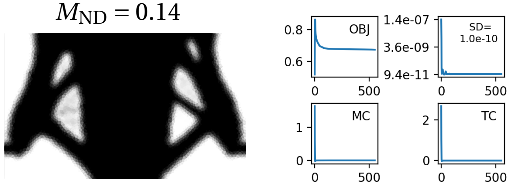 	$M_{\mathrm{ND}} = 0.21$ 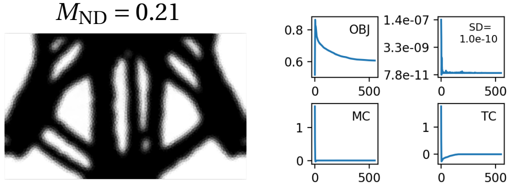 	$M_{\mathrm{ND}} = 0.24$ 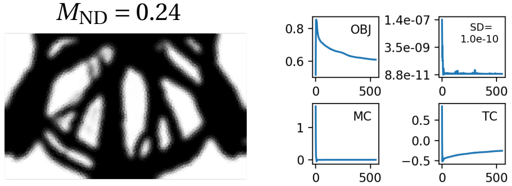
	$c_{\mathrm{u,max}} = 2.25 \times 10^{-6}$	$M_{\mathrm{ND}} = 0.14$ 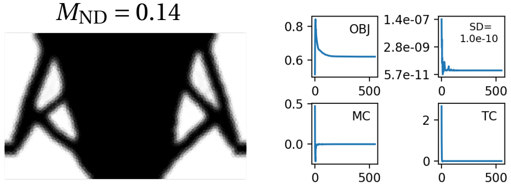 	$M_{\mathrm{ND}} = 0.21$ 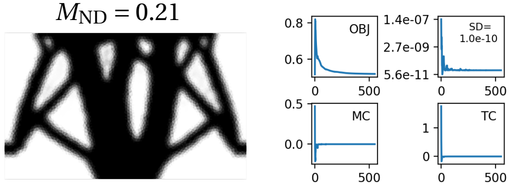 	$M_{\mathrm{ND}} = 0.25$ 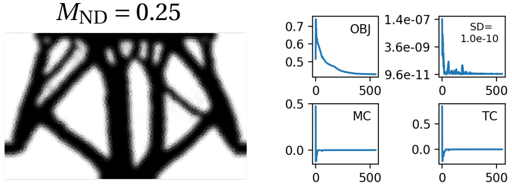
	$c_{\mathrm{u,max}} = 3.30 \times 10^{-6}$	$M_{\mathrm{ND}} = 0.14$ 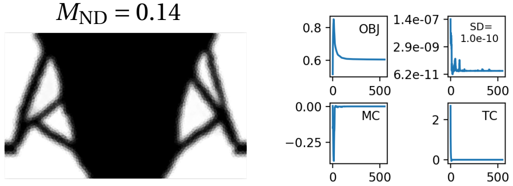 	$M_{\mathrm{ND}} = 0.17$ 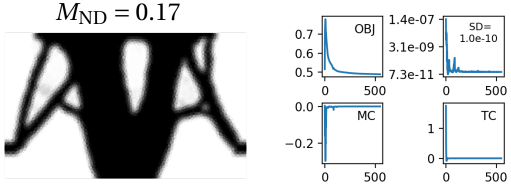 	$M_{\mathrm{ND}} = 0.30$ 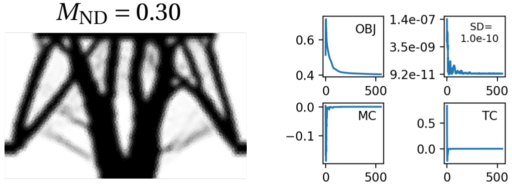

3.5. Discussion

Throughout this chapter the mechanical and thermal compliance constraints have successfully been used to control the final design, and therefore the mechanical and thermal performance of the system. The first "co-located" model overlaid both the mechanical and thermal problem to compare what accounted as a "stiff" design and a thermally "conductive" design while reducing surface deformations to a minimum. This can be seen in the first row and first column of Table 3.8.

The second model successfully managed to "steer" the problem to focus on being more stiff or more thermally conductive by separating the heat sink from the fixed points. When more stiffness was needed, a larger proportion of the volume accounted for supporting the mechanical structure. For less thermal resistance (or better conduction) the volume was attributed to improving the thermal path of the system, as expected. This "separated" model also meant that both the mechanical and thermal compliance constraints were active, irrespective of the severity of the applied constraint parameter. This can be seen in all entries of Table 3.12.

Although convergence of the optimization is improved for both models by actively changing the volume constraint in Optimization problem 2, the method is time consuming as it requires the user to iteratively adapt $V_{\mathrm{frac,max}}$. This often meant allowing the full number of iterations to be performed only to still be left with a grey density distribution. Once an acceptable value of $V_{\mathrm{frac,max}}$ was found, it sometimes came with a small penalty to the objective function, however rarely did the objective function fully appear to converge with either Optimization problem 1 or 2. Therefore Optimization problem 3 was set up to alleviate the shortcomings of the previous two. Reformulating the optimization problem as a volume minimisation, and setting the surface deformation as a constraint allowed for far better and quicker convergence. The rate of convergence did degrade quickly when the surface deformation parameter $c_{\mathrm{SD,max}}$ was set too stringently, therefore a tradeoff was found using $c_{\mathrm{SD,max}} = 10^{-10}\,\mathrm{m}^2$ (meaning that the average deviation from the mean is $10^{-5}\,\mathrm{m}$). The surface deformation constraint generally allowed for a larger error on the sides of the mirror surface shown in the surface deformation plots of Tables 3.5 and 3.9.

The MSE of the surface deformation can therefore mischaracterise surface deformation performance, whereby bad performance at the ends of the mirror is evened out by better performance around the centre of the mirror or allowing for oscillations along the mirror surface. This can be improved by:

- Reducing $c_{\mathrm{SD,max}}$ will reduce the overall error, however it is apparent that there is a limit to this parameter which still allows for convergence.
- Putting a constraint on the maximum deviation of any single displacement DOF. This will spread the error more evenly along the mirror surface. This would a require an individual constraint on each DOF which in the interest of the MMA optimizer is not desirable.
- A spacial weighting could be included in the MSE formulation, to add more significance to deformations in certain regions. This could be based on an analysis of which regions are most significant to optical performance.
- Attaching a constraint on the Zernike coefficients of interest, provides more granular control over certain optical performance related measures.
- Increasing the power of the MSE could also show improved performance on the concentration of errors. By penalising the outliers ever more substantially.
- Thickening the mirror layer used, may reduce the oscillations along the mirror layer, but tends to increase the deviations at the ends as seen in the top examples of the Tables 3.5 and 3.9.

Both models acted predictably to the varying mechanical and thermal compliance constraints. The original use of these two compliance constraints, as mentioned earlier, was to prevent the optimizer from converging to "un-coupled" designs, however the presence of the compliance constraints also contributed to better and faster convergence by better bounding the optimization problem.

Although not mentioned prior to this, the resulting density distributions are not symmetrical. This is in part to two aspects of the modelling choices made:

- Firstly: an unstructured mesh has been used which can be a contributing factor to the non-symmetrical designs.

- Secondly: the full domain has been optimised. In the literature study many of the examples found (especially large scale examples) leverage symmetry anywhere possible. Therefore only half and sometimes even quarter domains are optimized meaning that the symmetry lines in 2D and surfaces in 3D have special boundary conditions allowing for the optimization to recognize the boundary as a reflection of the optimized surface. Future chapters will contain an inherent asymmetry therefore a symmetrical approach was not sought.

Heat sinks with prescribed temperature values were used in this chapter. This approach resulted in designs with very high fluxes near the heat sinks (shown in the gradient plots of Tables 3.5 and 3.9). This phenomenon should not happen and is caused by modelling anomalies. This will most likely be solved in the subsequent chapters by the addition of convection to remove heat from the system.

The following chapters will be based on a model similar to the "separated" model where the thermal energy is removed through the bottom boundary of the model by means of a convective channel. This uniformity in the design configuration allows for comparisons to be made throughout the following chapters. The main driver for choosing the separated design is that a fluid plane can more easily be integrated into the system. This configuration also shares more commonalities with the current state of cooled mirror design, where the fluid channels are spread out through the entire mirror surface. The main difference to the current model is the limited size of the heat sink on Γ_{sink} with respect to the length of the convective boundary (referred to later as Γ_{conv}).

4

Thermo-mechanical and convection based optimization

In this chapter the model is updated by replacing the thermal heat sinks from the previous chapter with a fixed convective heat channel (or channels) acting as a heat exchanger along the bottom of the model. In the previous chapter, modelling inconsistencies arose due to the heat sink which had a prescribed temperature as a boundary condition.

Adding convection to the model should resolve this and in addition bring new features into consideration. Not only is the heat transfer from a solid into a fluid domain modelled, but also the heat transport in the fluid. The heat transport, acting in the direction of the fluid flow, adds an asymmetry (should be seen in Figure 4.1 as a fluid flow from, for example, left-to-right) to the thermal problem which will be reflected in the thermal expansion of the system and therefore the optimizer will take this into consideration in the thermo-mechanical structure. Figure 4.1 provides a simplified glimpse into the additional elements in this chapter.

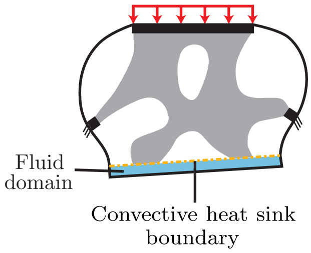

Figure 4.1: Interpretation of the modelling elements, now including a convective boundary.

By not yet optimizing the fluid channels, the optimizer only has control of the thermo-mechanical structure and which portions of the convective boundary to convect heat to. This simplification allows the analysis of the system to be focused on the interaction between the thermo-mechanical system and the convective heat boundary, therefore eventual changes in these these two areas can be associated with the addition of the fluid domain in the optimization problem.

The mechanical compliance constraint is used to ensure feasible mechanical structures are created and the thermal compliance constraint is primarily used to ensure thermal contact along the convective boundary. Having already investigated the influence of the prescribed values $c_{\mathrm{u,max}}$ and $c_{\mathrm{t,max}}$ of these constraints in the previous chapter, each case in this chapter will retain a constant value throughout this chapter. However, to gain a better insight into the convective contribution, variations in the flow conditions can be brought about by influencing the heat transfer coefficient h_{c}.

Two different analyses will be made in this chapter which affect the heat transfer coefficient. Firstly the Péclet number, a ratio between the advective and diffusive transport rate, will be varied for two different models. This provides an understanding of the influence the convection has on the mirror support structure. Thereafter the optimization problem is tested by altering the convective fluid channel layout, by increasing the number of fluid channels whilst maintaining the same flow velocity and surface area in contact with the convective boundary, to investigate whether the optimized density distributions vary significantly when spreading the fluid channels more evenly.

4.1. Thermo-mechanical and convective domain and model definition

Fluid flow enters the system with a temperature θ_{in}, and is heated up by the flux q_{in} entering the system through the mirror. Assuming no conduction through other domain boundaries, Newton's law of cooling states:

$$q_{\text{in}} = h_{\text{c}}(\theta_{\text{out}} - \theta_{\text{in}}) \tag{4.1}$$

where the flux q is equal to the heat transfer coefficient h_{c} times the temperature difference between inlet and outlet $(\theta_{\text{out}} - \theta_{\text{in}})$. Knowing that the thermal flux entering the system must be the same as that leaving the system, and the temperature at the inlet is $\theta_{\text{in}} = 0\,\text{K}$, one can rearrange Equation 4.1 for the outlet temperature of the fluid to:

$$\theta_{\text{out}} = q_{\text{in}}/h_c. \tag{4.2}$$

The heat transfer coefficient is therefore of interest when quantifying the degree of convection of the system. When increased, this would reduce the temperature at the outlet of the cooling channel. In this chapter the heat transfer coefficient is dependent on the following: $h_{\text{c}} \propto \{A_{\text{surface}}[s_i], \text{Pe}, v\}$ where only $A_{\text{surface}}[s_i]$, the surface area in contact with the flow channel, is dependent on the optimization design variables s_i. The other two variables: the non-dimensional Péclet number Pe, and the fluid velocity v are the parameters that can be altered to change the convective characteristics of the system considered.

In areas where the thermo-mechanical structure comes into contact with the cooling channel, heat is convected to the channel. The temperature rise along the length of the cooling channel affects the temperature field of the entire thermo-mechanical system as well. Two model orientations have been set-up, where the first draws similarities to the "separated" model in Section 3.1.2 of the previous chapter and the second tests the altered temperature field on the resulting thermo-mechanical structure. The first is the "symmetric" model, where the fluid flow is out-of-plane (or into the page). Therefore, the gradient of the bulk temperature (averaged fluid temperature) runs parallel to this, meaning the asymmetry brought upon by the fluid flow goes seemingly unnoticed in the considered 2D domain. The "asymmetric" model sees the fluid flow orientated in-plane, here the gradient of the bulk temperature lies along the length of the channel.

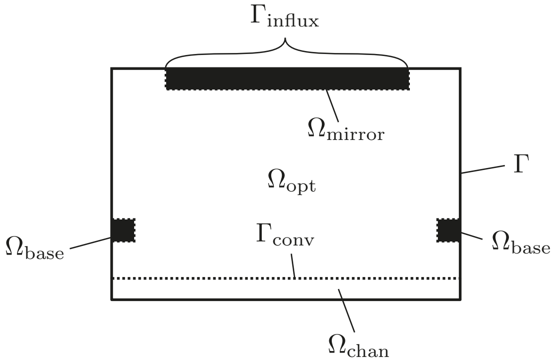

Figure 4.2: Domain designation of thermo-mechanical model.

In Figure 4.2 the sub-domain and boundary designations are shown. The main change compared to the "separated" model of the previous chapter is the addition of flow channel Ω_{chan}. Γ_{conv} is the convective boundary, portions of which will interface the solid thermo-mechanical structure and the fluid flow channel. This boundary is the edge of the mechanical and fluid domain, meaning that in the model mechanical deformations below Γ_{conv} are zero and flow velocities above Γ_{conv} are zero. The optimization sub-domain remains in Ω_{opt}, therefore Ω_{chan} is out of the optimization scope.

The mechanical domain is modelled as described in Chapter 3, the thermal domain now has the convection contribution from the fluid channel. The energy balance used to model convection in Ω_{chan} is the advection-diffusion equation:

$$\rho c_{\text{p}}(\mathbf{v}\cdot\nabla)\theta - k_{\text{f}}\nabla^2\theta = 0 \tag{4.3}$$

where ρ is the fluid density, c_{p} the specific heat capacity of the fluid, $\mathbf{v}$ the flow velocity vector and k_{f} is the conductivity of the fluid. The first term in Equation 4.3 is referred to as the advection portion whereas the second term is the diffusion portion in the fluid. This can be linked to the dimensionless Péclet number, which relates the diffusion rate to the advection rate in the system:

$$\text{Pe} = \underbrace{\frac{|\mathbf{v}|L}{\upsilon}}_{\text{Reynolds}}\underbrace{\frac{\upsilon}{\alpha}}_{\text{Prandtl}} = \frac{|\mathbf{v}|L}{\alpha} \tag{4.4}$$

where here $|\mathbf{v}|$ is the fluid flow velocity, L the characteristic length, υ the kinematic viscosity and α the thermal diffusivity (where $\alpha = \frac{k_f}{\rho c_{\text{p}}}$).

The thermal field in the solid domain can be modelled with:

$$Q + k_{\text{s}}\nabla^2\theta = 0 \tag{4.5}$$

where Q is the energy entering the system and k_{s} the conductivity of the solid. This is in fact the same equation as Equation 3.1, however the different solid and fluid conductivities can now be accounted for by the subscript s and f.

The boundary conditions of the thermal field are as follows:

$$\begin{aligned} -k_{\text{f}}\nabla\theta\cdot\mathbf{n} &= q_s \quad \text{on } \Gamma_{\text{influx}} \\ -k_{\text{f}}\nabla\theta\cdot\mathbf{n} &= 0 \quad \text{on } \Gamma \\ \theta &= 0 \quad \text{on } \Gamma_{\text{inlet}} \end{aligned} \tag{4.6}$$

where $\mathbf{n}$ represents the normal vector to the boundary and q_s the heat flux entering the system. The first boundary condition represents the conditions for flux entering the system, the second boundary condition states that the boundaries are adiabatic and the final boundary condition represents the prescribed inlet temperature of the flow. Although not shown in Figure 4.2, two boundaries preside over the inlet (Γ_{inlet}) and outlet (Γ_{outlet}) of the channel. Due to the varying orientation of fluid flow and arrangement of the channels, these have not been included in this figure, however their placement will become apparent in the next sections where the "symmetric" and "asymmetric" models are described in further detail. Dimensions of the models are found Appendix C.

4.1.1. Symmetric model

The flow in this model is out-of-plane, denoted in the left portion of Figure 4.3 with ⊗. Flow enters the sub-domain through the blue portion of Ω_{chan} with an inlet speed and relative temperature of $\mathbf{v} = \upsilon_{\text{in}}$ and $\theta = 0\,\text{K}$. The right portion of Figure 4.3 illustrates the channel configurations of two, three and four channel inlets, where the blue regions are Γ_{inlet} and directly behind them would be Γ_{outlet}. Due to the nature of this flow direction, a 3D model of one element thick is used to provide a convective surface that allows fow a temperature gradient in the flow direction. This temperature gradient in the flow direction has an effect on the thermal expansion near Γ_{conv} where the thermally induced strain is larger on the upstream side: this tilts the thermo-mechanical structure out-of-plane. This deformation is not of interest to the research and may result in artefacts in the resulting structure. As the aim is to compare the features of this model with those of the previous chapter, these out-of-plane deformations are not considered and therefore set to zero.

The use of 3D elements would double the number of nodes in this model and have an even larger impact on the number of elements, therefore the mesh has been made coarser to reduce the computation time of the optimization.

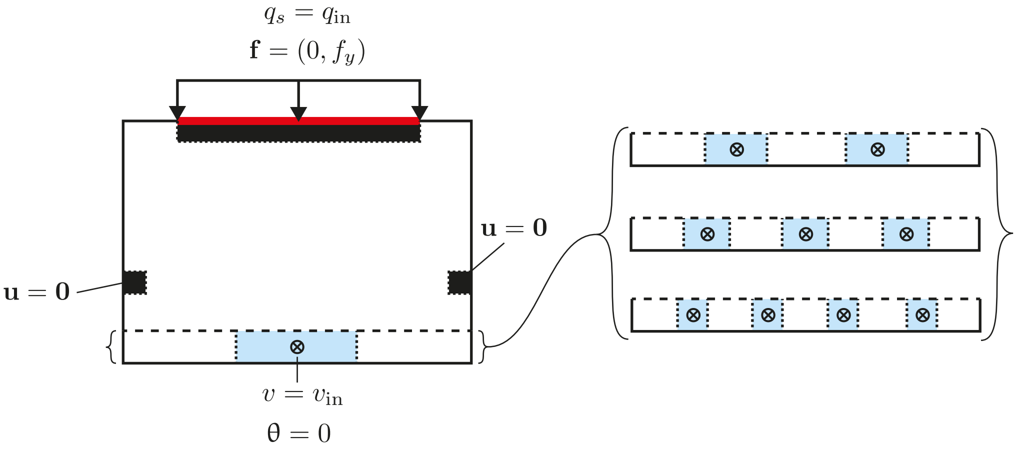
$q_s = q_{\text{in}}$
$\mathbf{f} = (0, f_y)$
$\mathbf{u} = \mathbf{0}$
$\mathbf{u} = \mathbf{0}$
$v = v_{\text{in}}$
$\theta = 0$

Figure 4.3: "Symmetric" model with on the left the full one channel model. The right portion illustrates the channel configurations where the total surface area of the flow channels (in blue) is equal to that of the single channel.

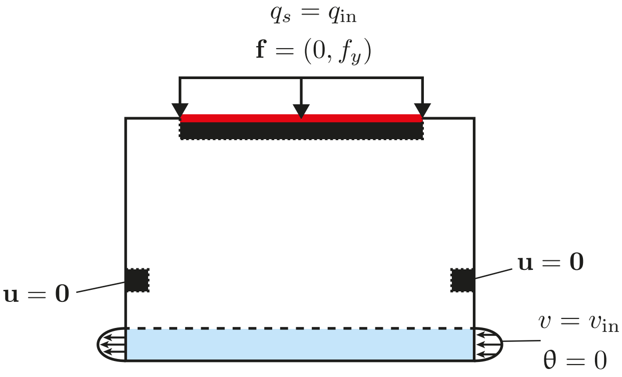
$q_s = q_{\text{in}}$
$\mathbf{f} = (0, f_y)$
$\mathbf{u} = \mathbf{0}$
$\mathbf{u} = \mathbf{0}$
$v = v_{\text{in}}$
$\theta = 0$

Figure 4.4: "Asymmetric" model with a flow direction from right to left along the bottom sub-domain Ω_{chan} (in blue).

4.1.2. Asymmetric model

The flow in this model is seen entering the bottom-right corner of the model in Figure 4.4 with an inlet speed and relative temperature of $|\mathbf{v}| = v_{\text{in}}$ and $\theta = 0$. This flow direction can be modelled in 2D, meaning no constraints have to be made (or can be made) on the out-of-plane deformations, therefore this model is uses 2D elements. The locations of Γ_{inlet} and Γ_{outlet} are located at the entry and exit of the flow channel.

4.1.3. Modelling considerations of thermal boundary constraints of heat sink

Where in the previous chapter the heat sink was a predefined Dirichlet boundary constraint, the introduction of a convective boundary Γ_{conv} changes the thermal solution of the system. The temperature at the inlet is set by prescribing Dirichlet boundary conditions. Because Γ_{inlet} and Ω_{opt} share a node in the "asymmetric" model and multiple nodes in the "symmetric" model, care has to be taken to ensure that the boundary condition set in the previous chapter is not replicated. By not applying Dirichlet boundary conditions on Γ_{conv}, i.e. the nodes that are shared by (Ω_{chan}) and (Ω_{opt}), direct heat transfer from the thermo-mechanical domain to these heat sinks through conduction is avoided. Figures 4.5 and 4.6 show the steps taken to separate the temperature boundary condition from the convective boundary Γ_{conv} to prevent the thermal solution tending to the Dirichlet condition.

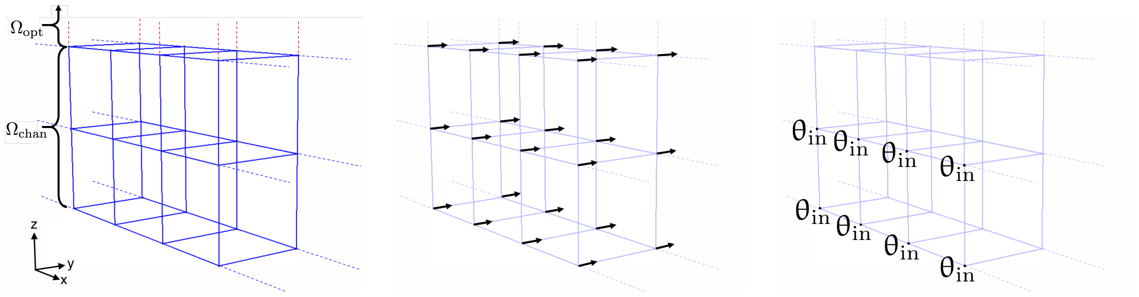

(a) 3D representation of elements in the sub-domain Ω_{chan}.

(b) Prescribed velocities in Ω_{chan}.

(c) Prescribed temperature on Γ_{inlet}. Note that the temperature is not prescribed on the boundary Γ_{conv}.

Figure 4.5: Zoomed-in view of the symmetric mesh. The field of view is of an arbitrary portion within Ω_{chan} where velocity and temperature conditions are applied.

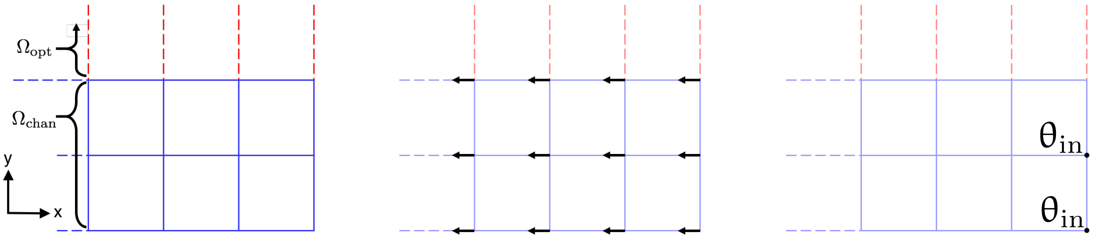

(a) 2D representation of elements in the sub-domain Ω_{chan}.

(b) Prescribed velocities in Ω_{chan}.

(c) Prescribed temperatures on Γ_{inlet}. Note that the temperature is not prescribed on the boundary Γ_{conv}.

Figure 4.6: Zoomed-in view of the asymmetric mesh. The field of view is on the bottom right corner of Ω_{chan}, where the channel inlet (Γ_{inlet}) boundary conditions are prescribed.

When $\lim_{v_{\text{in}} \to 0}$ the advection contribution reduces to a point where it no longer influences the thermal system. At this point the thermal problem, like in the previous chapter, reduces to the diffusivity (conductive) contribution of the PDE. It tends to the prescribed temperature boundary conditions at Γ_{inlet} while no flux leaves the system at Γ_{outlet}. Here, only the conduction of the solid structure and fluid make up the thermal problem.

In Table 4.1 a comparison is made of the thermal effects the $\theta = 0$ boundary condition placement has on the system. The correct placement of the boundary conditions forces the thermal problem to convect heat through the flow channel. This is reflected in the (magnitude of the) gradients, where the largest gradients occur beneath Γ_{conv} downstream of the prescribed temperature nodes. If applied incorrectly, the thermal gradients are highest above the Γ_{conv} boundary, meaning that heat is primarily being conducted out of the system through the prescribed node on the boundary. Prescribed temperature nodes on the boundary allows for heat to leave the system purely through the solid domain, which is the path of least thermal resistance. This will most likely have an effect on the final design as the optimizer will seek to leverage this phenomenon. A "direct" path to the heat sink will also artificially lower the average temperature of the system due to the lower resistance. This can be seen in the lower maximum temperature in the temperature plots of the incorrectly placed boundary conditions compared to the higher temperatures when placed correctly.

Table 4.1: Comparison of correct and incorrect placement of the $\theta = 0$ Dirichlet boundary condition on both the "symmetric" and "asymmetric" model. The flow direction is for both models from right to left. • indicates the node is prescribed with a $\theta = 0$ boundary condition. ---- indicates the Γ_{conv} boundary. This model is simulated under the assumption that Ω_{opt} is completely solid ($\rho = 1$).

	Correct BC placement		Incorrect BC placement		Location
	Temperature (K)	Gradient (K/m)	Temperature (K)	Gradient (K/m)	(indicated by □)
Symmetric	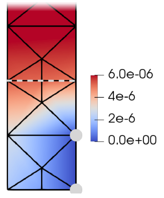	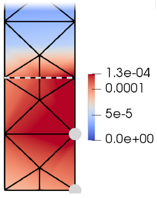	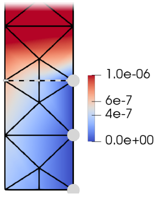	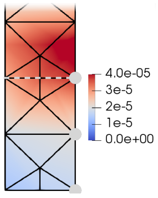	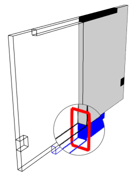
Asymmetric	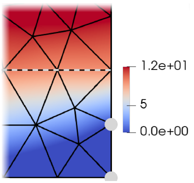	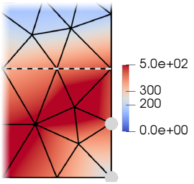	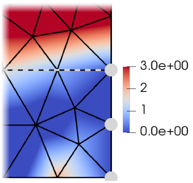	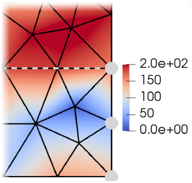	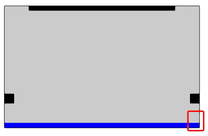

4.2. State equations

The thermo-mechanical relation from Chapter 3 remains the same, but this chapter adds a convective component to the problem. The fluid problem is not an active part of the optimization therefore it is sufficient to simply supply the fluid velocity vector $\mathbf{v} = (v_x, v_y, 0)$ to the convective contribution. The z-component of the fluid velocity is to zero to ensure flow within Ω_{chan}. The convective FE discretisation is shown in Appendix A.2. The state equations from Equation 3.5 of the thermal and mechanical system expand therefore to:

$$\begin{bmatrix} (\mathbf{K}_{\mathrm{C}}[\mathbf{v}] + \mathbf{K}_{\mathrm{D}}) & \mathbf{0} \\ -\mathbf{A} & \mathbf{K}_{\mathrm{U}} \end{bmatrix} \begin{bmatrix} \theta \\ \mathbf{u} \end{bmatrix} = \begin{bmatrix} \mathbf{q} \\ \mathbf{f} \end{bmatrix} \tag{4.7}$$

where $\mathbf{K}_{\mathrm{C}}[\mathbf{v}]$ is the convection matrix dependent on the velocity vector.

4.3. Material interpolation

The same RAMP penalisation scheme as in the previous chapter is used to scale the material properties of the solid and fluid. The thermo-mechanical scaling remains largely the same, however the conductive matrix $\mathbf{K}_{\mathrm{D}}$ now has the added contribution from the fluid shown in Equation 4.8. The two "full material" conductive matrices are given as $K^0_{\mathrm{D,solid}}$ and $K^0_{\mathrm{D,fluid}}$. The convection contribution is interpolated the same as the the fluid conduction. The interpolation is given as follows:

$$K^i_{\mathrm{U}} = \rho_i K^0_{\mathrm{U}} \qquad K^i_{\mathrm{C}} = (1-\rho_i) K^0_{\mathrm{C}} \qquad K^i_{\mathrm{D}} = \rho_i K^0_{\mathrm{D,solid}} + (1-\rho_i) K^0_{\mathrm{D,fluid}} \qquad A^i = \rho_i A^0. \tag{4.8}$$

As shown in Equation 4.8, ρ_i is still used to interpolate the element matrices of the solid regions whereas $(1-\rho_i)$ is used for the flow regions in Ω_{chan}. This scheme ensures that the fluid material properties vanish in the solid domain and vice versa.

4.4. Optimization problem

In this chapter the "symmetric" and "asymmetric" models will be compared for a range of Péclet values. A larger Péclet number represents an improved advective-to-diffusive transport rate of convection which can be considered as increasing the degree of convection of the system. This improvement in the degree of convection will be compared in both the symmetric and asymmetric setting. Thereafter the final thermo-mechanical structures will be compared for the "symmetric" model with varying numbers of cooling channels. This can all be done using the same optimization problem.

4.4.1. Optimization problem 4: Volume minimisation with surface deformation constraint

An alteration is made to Optimization problem 3 of Chapter 3 to account for the added convection to the thermal problem. Therefore, the objective is to minimise volume subject to surface deformation, mechanical compliance and thermal compliance constraints:

$$
\begin{aligned}
\min_{s} \quad & f = \frac{1}{V}\sum_{i} V_i \rho_i \\
\text{s.t.} \quad & \begin{bmatrix} (\mathbf{K}_{\mathrm{C}}[\mathbf{v}] + \mathbf{K}_{\mathrm{D}}) & \mathbf{0} \\ -\mathbf{A} & \mathbf{K}_{\mathrm{U}} \end{bmatrix} \begin{bmatrix} \boldsymbol{\theta} \\ \mathbf{u} \end{bmatrix} = \begin{bmatrix} \mathbf{q} \\ \mathbf{f} \end{bmatrix} \\
& g_1 = \frac{1}{\log_{10}(C c_{\mathrm{SD,max}})} \log_{10}\left(C \frac{1}{m} \sum_{j=1}^{m} (x_j - \bar{x}_j)^2 + 1 \right) - 1 \leq 0 \\
& g_2 = \frac{\mathbf{u}_{\mathrm{m}}^{\top} \mathbf{K}_{\mathrm{U}} \mathbf{u}_{\mathrm{m}}}{c_{\mathrm{u,max}}} - 1 \leq 0 \\
& g_3 = \frac{\boldsymbol{\theta}^{\top} \mathbf{K}_{\mathrm{D}} \boldsymbol{\theta}}{c_{\mathrm{t,max}}} - 1 \leq 0 \\
& \rho_{\min} \leq \rho \leq 1
\end{aligned}
\tag{4.9}
$$

where $\mathbf{v}$ in the convection matrix is prescribed.

The thermal compliance constraint is with respect to the conduction matrix $\mathbf{K}_{\mathrm{D}}$ which includes the material properties of the solid and liquid. It is however recommended that it be the scope of another study to see what the precise influences are of considering all contributing factors (e.g. $\boldsymbol{\theta}^{\top}(\mathbf{K}_{\mathrm{D}} + \mathbf{K}_{\mathrm{C}})\boldsymbol{\theta}$) to the thermal domain in the calculation of the thermal compliance constraint.

4.5. Results

First the variation of the non-dimensional Péclet number is considered in the symmetric and asymmetric setting. The density distribution of the thermo-mechanical structure adapts itself to different values of the Péclet number. The bulk temperature of the fluid flow at the outlet Γ_{outlet} is also compared for the varying Péclet values. The density distributions will subsequently be compared for the symmetric model with varying channel numbers. The plots of the objective and constraints - shown next to the designs in the results of Chapter 3 - have been negated, as there is little to comment on their convergence plots. One can therefore assume that the constraints are feasible and that the volume objective attained a steady value.

4.5.1. Symmetric model: Variation of Péclet

The results of the "symmetric" case are given in Table 4.2. Each subsequent column corresponds to an increasing Péclet number. Péclet numbers were chosen heuristically where a range from 1.0 to 5.0 offered a spread of results which show a clear design progression. The density distributions given in the first row are not perfectly symmetrical likely due to the unstructured 3D mesh used. The 3D unstructured mesh (explained in Section 4.1.1) in this chapter has been made coarser (larger elements than the 2D mesh used in the thermo-mechanical model) which is therefore more prone to mesh dependency. Furthermore, the region below the mirror layer has converged to grey regions, likely an attribute of the coarser mesh. This region is highly sensitive to the surface deformation constraint, therefore discrete convergence is slow or unattainable at the current mesh size.

The mechanical compliance constraint has achieved a uniform "mechanical strut" (arms holding the mirror to the base), seen in the row with density distributions, throughout the Péclet range. This has led to the main deformation, the vertical piston action, to be almost the same across the Péclet range.

The thermal compliance constraint imposed on the optimization problem imposes a minimum thermal performance on the conductive properties system. This performance target is reached with less volume (seen by the narrowing thermal members leading to the flow channels) with increasing Péclet. This would indicate that the improving rate of advection to diffusion in the fluid flow improves the thermal compliance therefore less material is required to reach the same minimum thermal compliance constraint.

The highest temperature gradients occur at the interface between the thermo-mechanical structure and the fluid channel. As the surface area of this interface decreases with increasing the Péclet number, the temperature gradient peaks do not increase in magnitude until the last case (Pe = 5.0) although the difference is subtle. However, the high temperature gradients appear to echo the location of the high temperatures in the channel regions. The channel length is one element thick which results in a relatively small contact surface area. This is why the temperature in the fluid channel varies considerably in the cross-section. The bulk temperature was taken as the average temperature at Γ_{out} and plotted against the varying Péclet values. A lower outlet temperature was expected with an improved heat transfer coefficient h_c (Section 4.1), and this trend does hold true when the surface area A_{surface} is constant between $1 \leq \text{Pe} \leq 1.5$, this trend however diminishes when the surface area reduces for $\text{Pe} > 1.5$.

4.5.2. Asymmetric model: Variation of Péclet

The results of the "asymmetric" case are shown in Table 4.3. As in the previous section, each subsequent column is representative of increasing the Péclet number. Again the Péclet numbers were chosen heuristically to offer a spread of results which show a clear design progression. The asymmetric flow entering the domain Ω_{chan} from the right has had an obvious effect on all the designs when compared to the "symmetric" model. The resulting designs all share a slant from the mirror surface towards the colder side of the fluid channel. Most material is placed on this cooler side of the domain, although the proportion changes as the Péclet number increases. The optimization has converged reasonably discretely for all the variations of the Péclet number. In Appendix D.1 the density distribution of the asymmetric model is plotted with a more stringent $c_{\text{SD,max}} = 1 \times 10^{-11}\,\text{m}^2$ surface deformation constraint, which hasn't been provided here due to the noticeably poorer convergence. What is apparent is that the asymmetry in the final design has largely disappeared (and becomes even less for larger Péclet values). This would indicate that surface flatness does benefit from symmetry irrelevant of the asymmetric temperature field or flow conditions.

Whereas in previous optimizations, the mechanical "struts" connecting the mirror to the base were reasonably symmetrical this has been altered to favour conducting heat to the cooler side of the domain. As a consequence, the trajectory of the vertical piston motion of the structure has gained a subtle horizontal displacement to the left.

As a result of the asymmetric setup, the temperature field of the structure is tilted, the cooler (blue) region extends further up on the right hand side of the domain than on the left. This temperature asymmetry also extends up towards the mirror surface where the left portion is warmer.

The temperature gradients given in the fourth row again show peaks at the channel-structure interface. All the cases share a temperature gradient peak at the channel inlet. If this were briefly considered a measure of the heat transfer, comparing the temperature in the channel, from right to left, the blue sliver of cold flow entering gradually gets larger, therefore the heat transfer rate smaller. The centre leg of case Pe = 5 shows a second heat transfer peak, also very evident in the channel temperature graph, by the sudden increase in temperature. This magnitude of the heat transfer gradually diminishes with reducing Péclet, which is also why the outlet temperature θ_{out} reduces in magnitude.

4.5.3. Symmetric model: Variation of channel numbers

The results for the "symmetric" channel variation case are shown in Table 4.4. The channels share the same total channel volume, however they are subdivided evenly throughout the sub-domain Ω_{chan}. The top half of the density distributions shown in the first row share a similar design: poorly defined regions directly beneath the mirror surface followed by a hole in the centre. The poor definition is again partly due to the coarser mesh needed to be able to model with 3D elements. The bottom half of the density distributions show the forking necessary to reach the fluid channels. For Pe = 1, the final design covered the full surface of all the fluid channels, therefore all designs are based on a Péclet value of one. Raising the Péclet value would have meant that the optimizer would not have converged to all the heat sinks, as it would have met the thermal compliance constraint with a more volume efficient final design.

The temperature contour lines have been plotted in the fourth row to more easily compare the affect the channels have on the thermal symmetry of the structure. The increasing number of channels does not appear to vary the contour lines near the mirror surface considerably. The temperature gradient at the convection interface of the "one channel" case appears to be the highest compared to the other cases.

Table 4.2: Results of the "symmetric" model, subject to varying Péclet numbers. The first row represents the density distributions of the final optimization iteration, where the fluid channel runs along the bottom of the thermo-mechanical structure. The second row shows the deformed and undeformed states of the thermo-mechanical structure. The third row represents the surface deformations of the mirror. The fourth row shows the temperature field throughout the thermo-mechanical structure. The fifth row shows the temperature gradients, where the high gradients are seen to be found at the interface between the structure and flow channel. The sixth row is the temperature at the outlet of the channel Γ_{outlet} it has been scaled vertically to better show the temperature field.

Péclet	1.0	1.5	2.0	3.0	5.0
Density distribution $\rho_i = 0$ 1	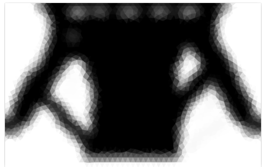	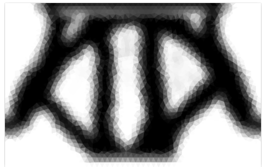	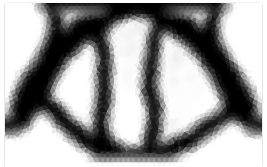	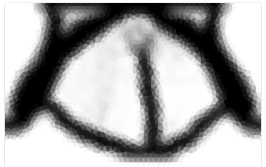	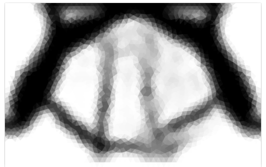
Deformed state ▨ Undeformed ■ Deformed	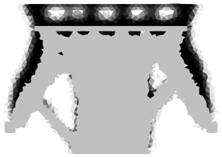	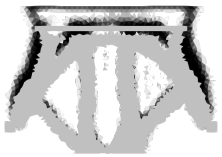	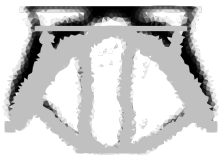	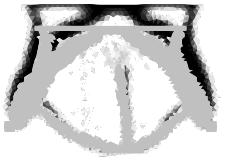	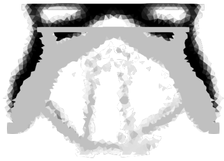
Surface deformation (m)	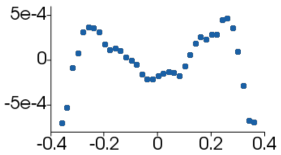	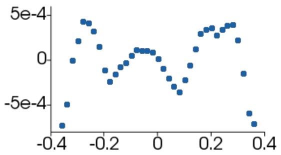	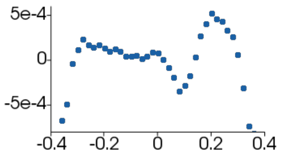	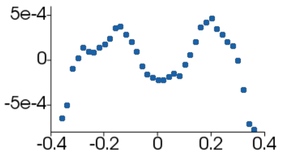	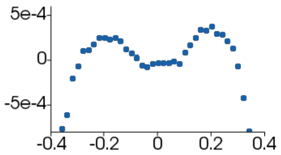
Temperature field (K) $\theta = 0$ 0.07	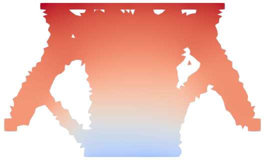	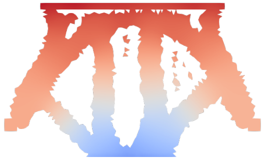	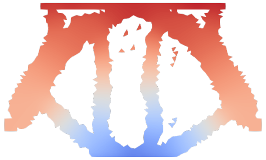	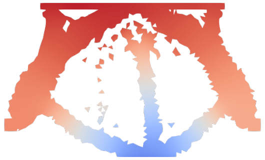	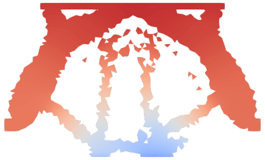
Magnitude of temperature gradient (K/m) $\nabla\theta = 0$ 0.6	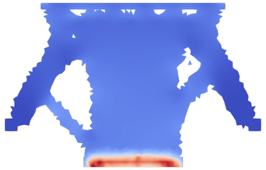	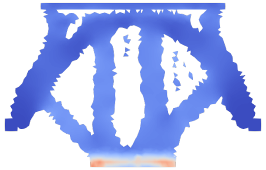	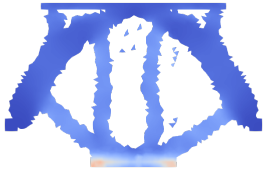	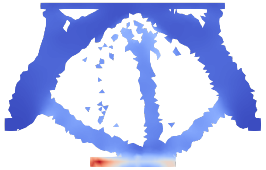	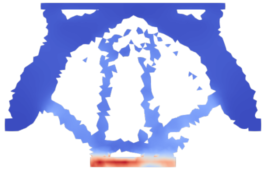
Channel temperature (K) $\theta = 0$ 0.025	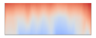	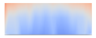	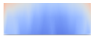	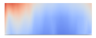	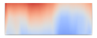

Table 4.3: Results of the "asymmetric" model, subject to varying Péclet numbers. The first row represents the density distributions of the final optimization iteration, where the fluid channel runs along the bottom of the thermo-mechanical structure. The second row shows the deformed and undeformed states of the thermo-mechanical structure. The third row shows the surface deformations of the mirror. The fourth row shows the temperature field throughout the thermo-mechanical structure. The fifth row shows the temperature gradients, where the high gradients are seen to be found at the interface between the structure and flow channel. The fifth row is the temperature along the channel Ω_{chan} it has been scaled vertically to better depict the temperature field. The final row is a graph of the bulk temperatures at the outlet of the channel as a function of the Péclet number.

Péclet	2.5	3.0	3.5	4.0	5.0
Density distribution $\rho_i = 0$ 1	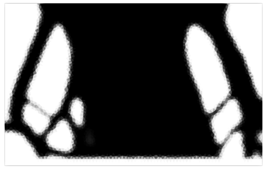	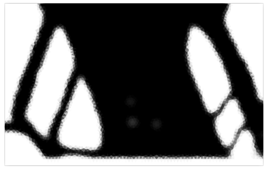	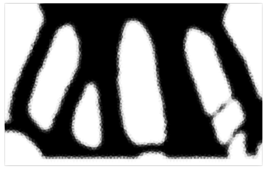	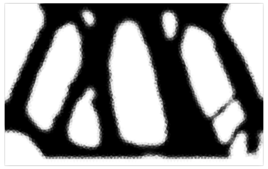	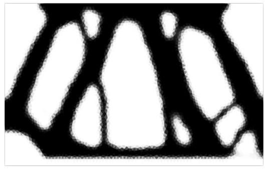
Deformed state ▨ Undeformed ■ Deformed	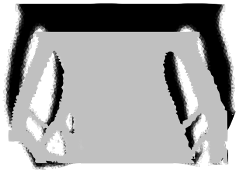	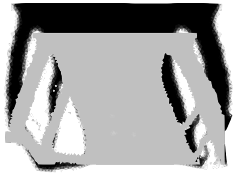	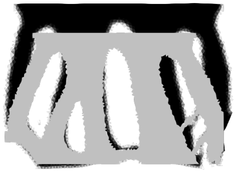	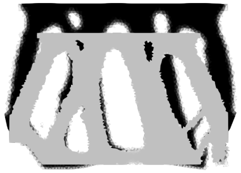	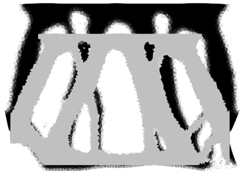
Surface deformation (m)	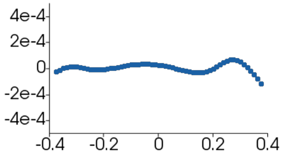	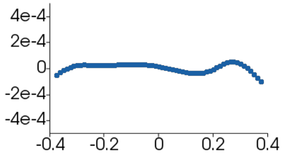	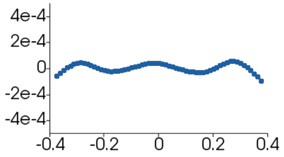	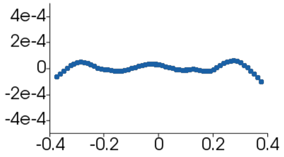	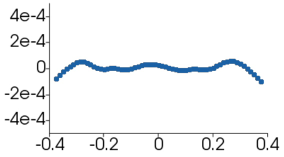
Temperature field (K) $\theta = 0$ 0.01	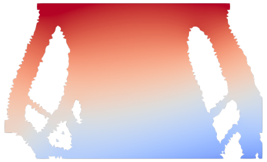	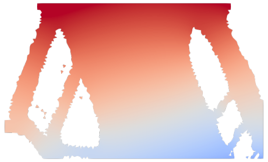	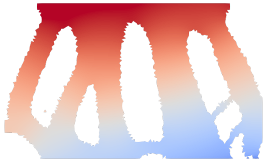	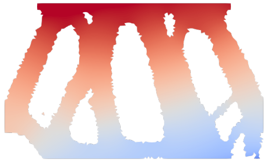	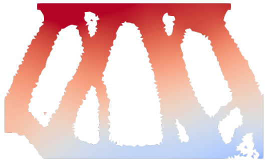
Magnitude of temperature gradient (K/m) $\nabla\theta = 0$ 0.03	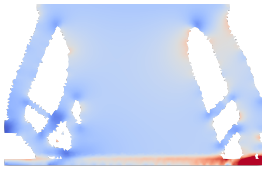	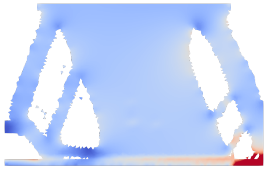	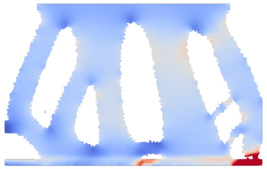	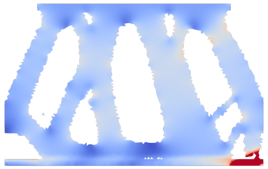	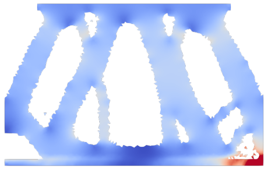
Channel temperature (K) $\theta = 0$ 0.005	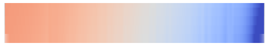	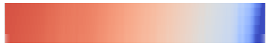	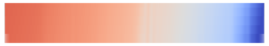	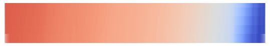	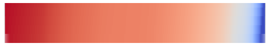

Table 4.4: Results of the "symmetric" model, subject to varying channel numbers. The first row represents the density distributions of the final optimization iteration, where the fluid channel runs along the bottom of the thermo-mechanical structure. The second row shows the deformed and undeformed states of the thermo-mechanical structure. The third row shows the surface deformations of the mirror. The fourth row shows the temperature throughout the thermo-mechanical structure. The fifth row shows the temperature gradients, where the high gradients are seen to be found at the interface between the structure and flow channel. The sixth row is the temperature at the outlet of the channel Γ_{outlet} it has been scaled vertically to better show the temperature field.

Channels	1	2	3	4
Density distribution $\rho_i = 0$ 1	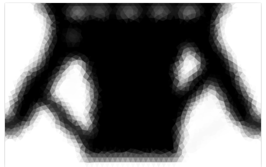	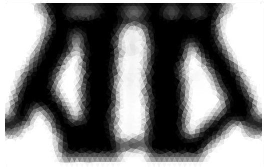	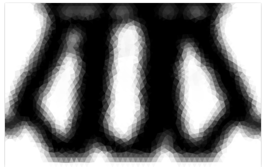	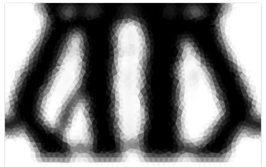
Deformed state ▨ Undeformed ■ Deformed	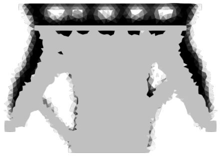	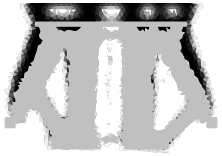	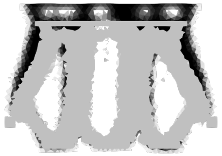	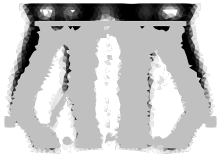
Surface deformations (m)	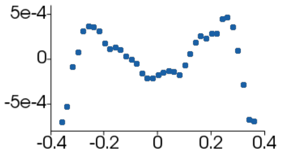	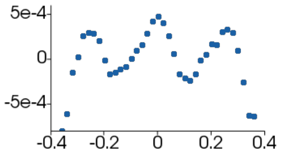	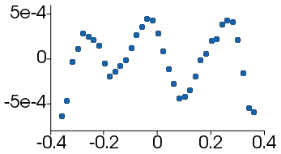	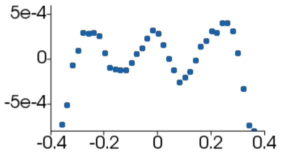
Temperature field (K) $\theta = 0$ 0.07	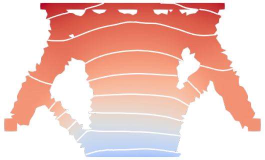	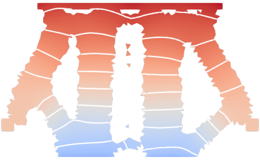	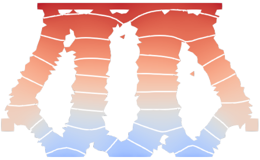	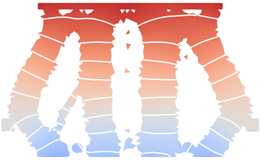
Magnitude of temperature gradient (K/m) $\nabla\theta = 0$ 0.6	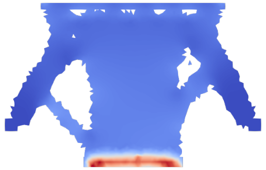	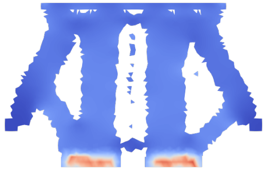	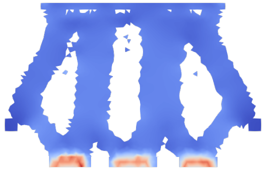	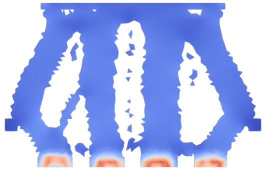
Channel temperature (K) $\theta = 0$ 0.025	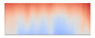	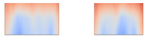	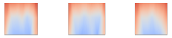	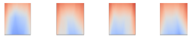

4.6. Discussion

The addition of convection to the thermo-mechanical system has successfully been implemented in a "symmetric" model where 3D elements are used and an "asymmetric" model with 2D elements. The use of 3D elements, due to the coarser mesh, had a deteriorating effect on the convergence of the regions directly beneath the mirror. This resulted in designs which met the surface deformation constraint, but converged to grey regions likely due to the high sensitivity of this region with respect to the constraint. This can most likely be ameliorated by refining the mesh to allow for smaller feature sizes, or possibly increasing the $c_{\text{SD,max}}$ value of the surface deformation constraint. Currently the grey regions have an ideal stiffness, conduction or expansion ratio which permit the surface deformation constraint from being met. The "asymmetric" model maintained the use of 2D elements, as in the previous chapter, returning well discretised convergence in the regions where the 3D elements faltered.

The use of the volume minimisation objective throughout this chapter produced reliably converging designs. A certain pitfall did however arise, in that the increased Péclet value allows the thermal compliance constraint to be met with minimal thermal contact with the convective heat sink. Increasing the Péclet values for a case with four channels would therefore eventually mean that the final design does not connect to all the convective heat sinks, and therefore is not using all the heat extraction regions effectively.

Although not expected, the thermal compliance constraint, interestingly, did not have a residing effect on the outlet temperature, as can best be seen in the "asymmetric" model. Where if one were to decrease the Péclet value with a constant thermal compliance constraint, the surface area in contact with the fluid channel increases in order to meet the thermal compliance constraint. The effect of the Péclet number on the temperature in the fluid channel was especially evident in the "asymmetric" model, where the contact areas showed more dramatic temperature variations in the fluid channel. Redefining the thermal compliance to include the contribution of the convective matrix may allow for more control of the outlet temperature and would be an interesting topic for study.

A series of graphs are plotted in Figure 4.7 of the "symmetric" and "asymmetric" model, analysing the convective part of the system. In Figures 4.7a and 4.7b the bulk temperature at the outlet θ_{out} is plotted against the Péclet number. Equation 4.2 suggested that with an improving heat transfer coefficient the outlet temperature would reduce. This is seen for $1 \leq \text{Pe} \leq 1.5$ for the "symmetric" model in Figure 4.7a where the outlet temperature decreases, however for $\text{Pe} > 2$ no further decrease occurs. The "asymmetric" model shows the opposite: an increasing outlet temperature for an increasing Péclet number. The effective heat transfer coefficient (shown in Figures 4.7c and) is not just dependent on the Péclet number but also the surface area in contact with the fluid channel. Meaning that as the Péclet number is increased, which improves the heat transfer coefficient, the contact surface area may decrease due to the volume minimisation objective, reducing the heat transfer coefficient. The surface area decreases because with an increasing Péclet number the thermal compliance constraint is more readily met with less surface area in contact with the fluid channel. This contact surface area remains the same between $1 \leq \text{Pe} \leq 1.5$ (as seen in Table 4.2), therefore the expected trend given in Equation 4.2 holds true. The moment the surface area decreases, the outlet temperature stabilises, as opposed to increasing again as seen in Table 4.2. This is most likely due to the short channel length providing less design dependent temperature variation (apparent in the long channel length of the "asymmetric" model).

The "symmetric" model returned similar designs to the "separated" designs of the previous chapter, where the variation of the Péclet number of the fluid flow in a newly introduced cooling channel provided a similar effect to the variation of the thermal compliance constraint. This in itself was not a goal, as this was to see the effect the degree of convection has on the resulting topology. The "asymmetric" model allowed us to study this question in a different context, namely with a convective channel running in-plane. This produced results with members leaning towards the cold fluid inlet. Optimal configurations were found which satisfied the surface deformation constraint, albeit with the addition of a small horizontal displacement. The next chapter adapts the optimization problem to include the fluid domain. This will allow the optimizer to choose a fluid channel layout that together with the thermo-mechanical problem can be used to satisfy the surface deformation constraint.

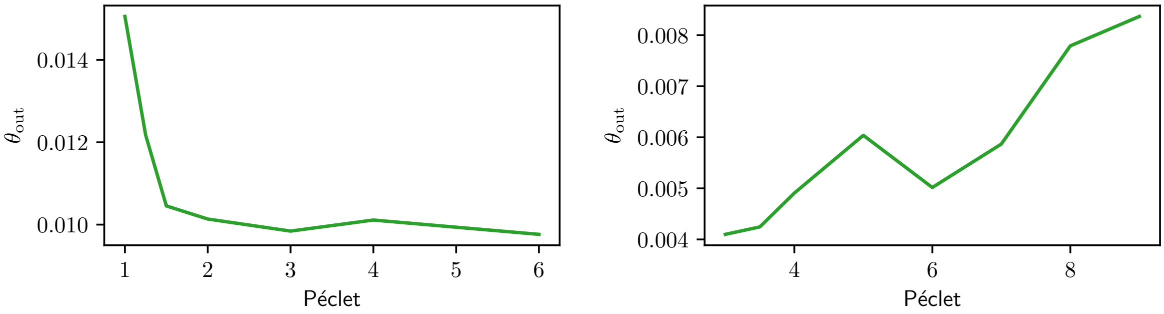

(a) The bulk temperature at the outlet of the "symmetric" model.

(b) The bulk temperature at the outlet of the "asymmetric" model.

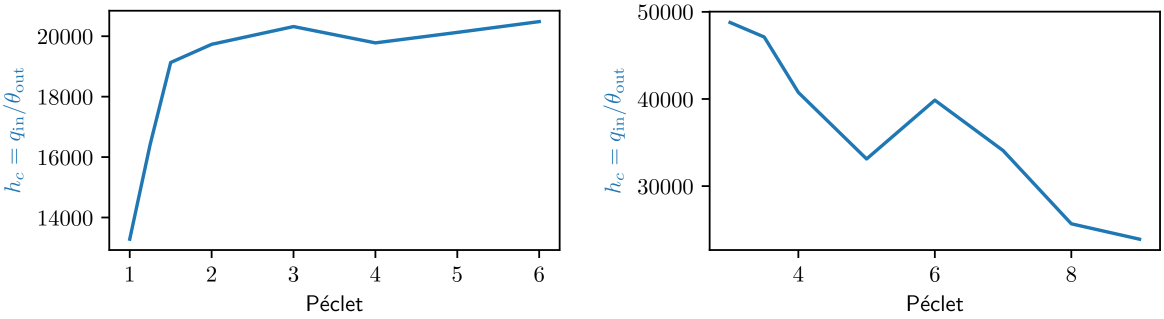

(c) The heat transfer coefficient of the "symmetric" model with respect to an increasing Péclet number.

(d) The heat transfer coefficient of the "asymmetric" model with respect to an increasing Péclet number.

Figure 4.7: Convective analysis of the "symmetric" and "asymmetric" models for varying Péclet numbers.

5

Thermo-mechanical, convective and flow based optimization

In this chapter the fluid domain which was fixed in the previous chapter is included in the optimization problem. This allows the optimizer to designate regions of flow along a fixed interface between the thermo-mechanical structure and cooling fluid flow where convection can increase the total system performance. Where in the previous chapter this was only achieved on the side of the thermo-mechanical domain, including the fluid domain in the optimization problem allows the interaction between these two domains to be evaluated. The location of the inlet and outlet of the fluid flow into the fluid domain are set as boundary conditions. The optimizer is therefore to set internal "channel walls", directing the fluid flow through the fluid domain as seen in Figure 5.1.

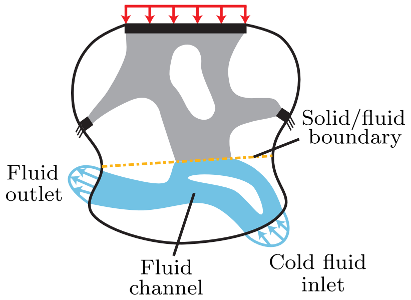

Figure 5.1: Interpretation of the modelling elements, now including a thermo-fluid domain to extract heat from the system.

Computational restrictions require further concessions to be made to the modelling of the optimization problem. An extension of the 3D mesh used in the "symmetric" model of Chapter 4 is adopted with a larger fluid domain. This "pseudo 3D" model connects a thermo-mechanical and thermo-fluid plane perpendicular to each other, interfaced at a convective boundary similar to that used in Chapter 4. The element size will therefore be increased to rein in the computation time.

The mechanical and thermal compliance constraints will again be used in this configuration to ensure that designs with realistic mechanical and thermal performance are generated. However the inclusion of the fluid flow in the optimization calls for a method to quantify flow performance and constrain it. This is done by means of a pressure drop constraint on the fluid domain, also referred to in literature as an energy dissipation constraint [Gersborg-Hansen et al., 2005].

The main variations to the optimization problem will be the positions of the inlet and outlet of the fluid flow into the fluid domain. Due to the coarser mesh, the region directly beneath the mirror in the thermo-mechanical domain will have a hard time to converge to a discrete design. Therefore the focus of this chapter will be more global. Where ultimately, the final topologies of the two interacting domains, constrained to meet a certain surface deformation threshold, will be of interest.

5.1. Thermo-mechanical, convective and flow domain and model definition

Although a fluid flow was present in the previous chapter, its position was fixed and its purpose was to serve as a convective medium to remove heat from the system. The thermo-fluid domain in this chapter is enlarged giving the optimizer more room to generate channels and better exploit the interaction between the thermo-mechanical structure and the fluid channels. In Figure 5.2 the different sub-domains and boundaries are shown. Figure 5.2a is a 3D representation of how the thermo-mechanical and thermo-fluid sub-domains intersect. Figure 5.2b is the thermo-mechanical plane which connects to the thermo-fluid plane shown in Figure 5.2c at Γ_{conv}. The positions of Γ_{in} and Γ_{out} are set by the user and their positions define the placement of the inlet and outlet of the fluid flow. Both sub-domains Ω_{TM} and Ω_{TF} (seen in Figure 5.2) make up the optimization domain for this optimization problem.

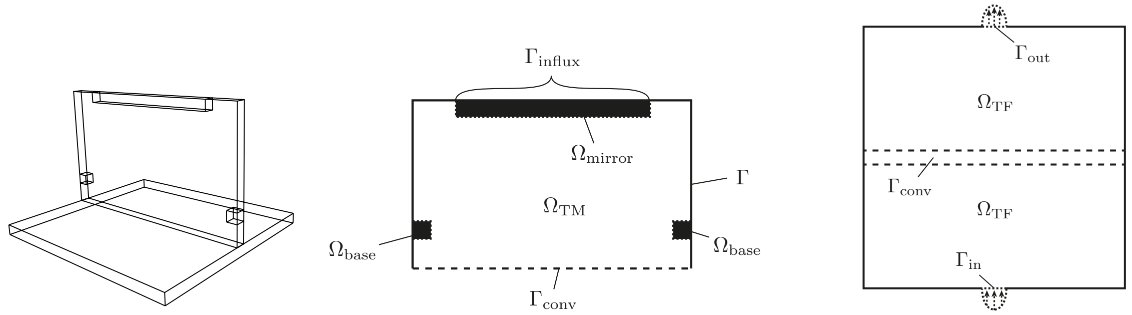

(a) 3D representation of the thermo-mechanical and thermo-fluid domains.

(b) Thermo-mechanical domain of the optimization problem.

(c) Thermo-fluid domain of the optimization problem.

Figure 5.2: Domain designation of thermo-mechanical and thermo-fluid optimization problem, where Ω_j represents the domain j and Γ_j represents the boundary j.

The inclusion of a fluid domain as part of the topology optimization problem requires changes to the fluid model and the fluid domain. The fluid model was not covered in the previous chapter in order to lay more focus on the convective aspect. Stokes flow is modelled in the fluid domain as:

$$\nu\nabla^2\mathbf{v} + \nabla p = \mathbf{b} \tag{5.1}$$

where ν is the kinematic viscosity, $\mathbf{v}$ the velocity vector, p the pressure and $\mathbf{b}$ the volume force per unit mass. Modelling Stokes flow in this way would bring about an unobstructed velocity and pressure distribution with no visible channel formation other than the boundary of the fluid domain. A channelling technique is needed whereby the design variables of the topology optimization are able to manipulate the domain to divert flow within it. Darcy flow is therefore added to the Stokes flow model, which ties the design variable of the topology optimization to a permeability term within the domain. A linear interpolation is used to scale between permeable regions modelled with Stokes flow and impermeable regions modelled with Darcy flow as shown in Equation 2.7. The dependence on ρ and μ is combined under the kinematic viscosity term in line with Equation 5.1:

$$\left((1-\rho)\nu\nabla^2 - \rho\frac{\nu}{\kappa}\mathbf{I}\right)\mathbf{v} - \nabla p = \mathbf{b} \qquad \text{in } \Omega_{\text{TF}}. \tag{5.2}$$

The thermo-mechanical and convective contributions are modelled as shown in Chapters 3 and 4.

5.2. Models with varying flow configurations

The thermo-mechanical portion of the models shown in Figure 5.3 remains the same as the previous chapter. The thermo-mechanical contribution is therefore not modelled in Ω_{TF} and thermo-mechanical sensitivities are set to zero in this region.

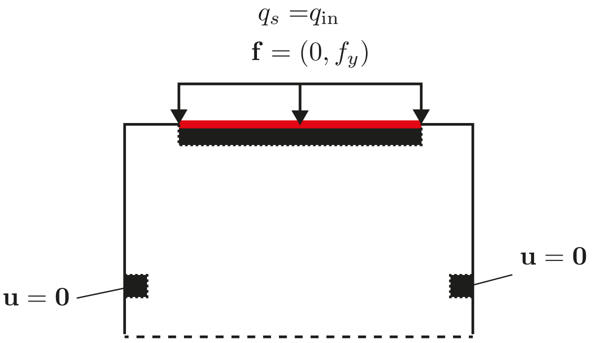
$q_s = q_{\text{in}}$
$\mathbf{f} = (0, f_y)$
$\mathbf{u} = \mathbf{0}$
$\mathbf{u} = \mathbf{0}$

Figure 5.3: Thermo-mechanical portion of the models.

The variations between the models in this chapter will be changes in the locations of the outlet with respect to the inlet of the fluid flow shown in Figure 5.4. These variations are expected to affect the converged design of the cooling channel layout and the thermo-mechanical structure.

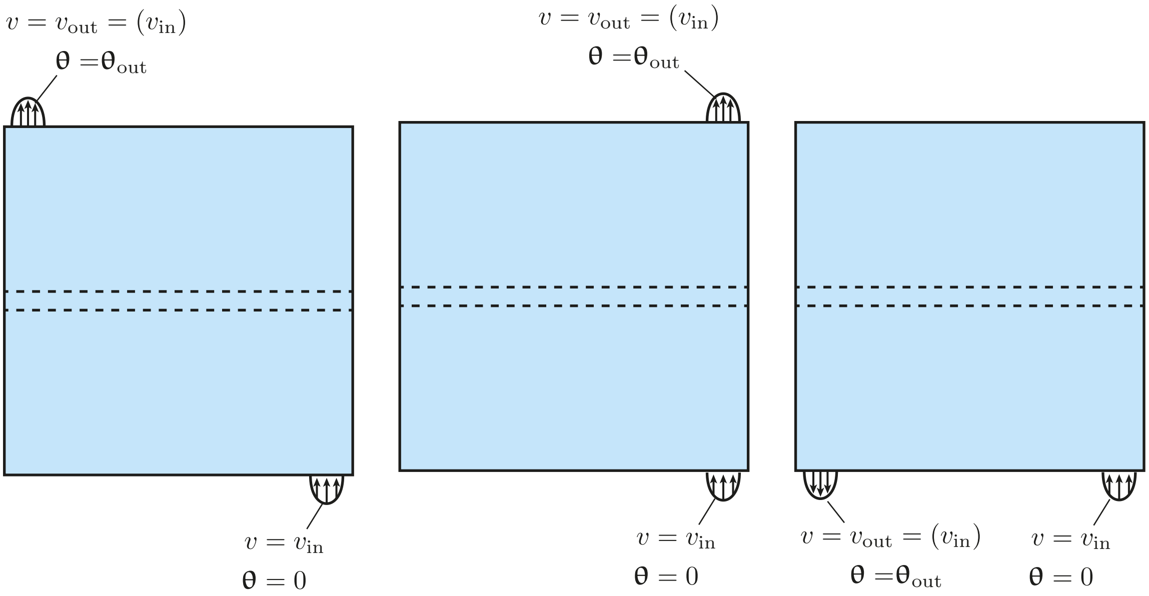
$v = v_{\text{out}} = (v_{\text{in}})$
$\theta = \theta_{\text{out}}$
$v = v_{\text{in}}$
$\theta = 0$
$v = v_{\text{out}} = (v_{\text{in}})$
$\theta = \theta_{\text{out}}$
$v = v_{\text{in}}$
$\theta = 0$
$v = v_{\text{out}} = (v_{\text{in}})$
$\theta = \theta_{\text{out}}$
$v = v_{\text{in}}$
$\theta = 0$

(a) Model 1. (b) Model 2. (c) Model 3.

Figure 5.4: Different flow layouts, where Figure 5.4b and 5.4c have been reduced in size, but represent the full domain shown in Figure 5.4a. Dimensions can be found in Appendix C.

The flow velocity at the fluid outlet is not prescribed, but it can be assumed $|\mathbf{v}_{\text{out}}| = |\mathbf{v}_{\text{in}}|$ as all other velocities on Γ are set to $\mathbf{v} = \mathbf{0}$. All velocities in the vertical z-direction are set to zero in Ω_{TF}. The pressure variable is the 'relative' pressure, where at the outlet of the system it is prescribed as $p = 0$.

The extra consideration given to the placement of the temperature boundary constraints at the fluid inlet in the previous chapter does not have to be considered in this chapter, as the pressure drop constraint (explained in Section 5.5.1) should prevent the solid regions in the thermo-fluid domain from contacting the inlet boundary. This constraint would work to open the channel and therefore the inlet boundary as well. If contact is made with the solid domain an area around the inlet can be forced to adopt "no material" ($\rho = \rho_{\text{min}}$) throughout the optimization.

5.3. State equations

The thermo-mechanical and convective relation from Chapter 4 remains the same. The flow contribution is provided by discretising the Stokes flow and Darcy flow equations (the full derivation can be found in Appendix A.3). For the Stokes flow system matrix a stabilisation term is introduced for it to function with *T4 elements* or four node tetrahedral elements, this is also discussed in more detail in Appendix A.3.

The complete system is therefore given as:

$$\begin{bmatrix} \mathbf{K}_{\text{DaS}} & \mathbf{B}_{\text{DaS}} & \mathbf{0} & \mathbf{0} \\ \mathbf{B}_{\text{DaS}}^{\top} & \mathbf{M}_{\text{DaS}} & \mathbf{0} & \mathbf{0} \\ \mathbf{0} & \mathbf{0} & \mathbf{K}_{\text{D}} + \mathbf{K}_{\text{C}} & \mathbf{0} \\ \mathbf{0} & \mathbf{0} & -\mathbf{A} & \mathbf{K}_{\text{U}} \end{bmatrix} \begin{bmatrix} \mathbf{v} \\ \mathbf{p} \\ \theta \\ \mathbf{u} \end{bmatrix} = \begin{bmatrix} \mathbf{f}_{\text{v}} \\ \mathbf{f}_{\text{p}} \\ \mathbf{q} \\ \mathbf{f} \end{bmatrix} \tag{5.3}$$

where $\mathbf{K}_{\text{DaS}}$ is the combined Darcy-Stokes viscosity matrix, $\mathbf{B}_{\text{DaS}}$ is the gradient matrix, $\mathbf{B}_{\text{DaS}}^{\top}$ is the divergence matrix and $\mathbf{M}_{\text{DaS}}$ is the stabilisation matrix. The unknown nodal velocity (in x, y, and z) and pressure are given by $\mathbf{v}$ and $\mathbf{p}$, and their respective nodal forces $\mathbf{f}_{\text{v}}$ and $\mathbf{f}_{\text{p}}$.

5.4. Material interpolation

The interpolation of the flow is given as follows:

$$\begin{aligned} K_{\text{DaS}}^{i}(\rho_i) &= \left((1-\rho_i)K_{\text{S}}^{i} + \rho_i K_{\text{Da}}^{i}\right) \\ B_{\text{DaS}}^{i}(\rho_i) &= \left((1-\rho_i)B_{\text{S}}^{i} + \rho_i B_{\text{Da}}^{i}\right) \\ B_{\text{DaS}}^{i^{\top}}(\rho_i) &= \left((1-\rho_i)B_{\text{S}}^{i^{\top}} + \rho_i B_{\text{Da}}^{i^{\top}}\right) \\ M_{\text{DaS}}^{i}(\rho_i) &= \left((1-\rho_i)M_{\text{S}}^{i} + \rho_i M_{\text{Da}}^{i}\right) \end{aligned} \tag{5.4}$$

where Stokes flow (denoted by subscript 'S') is interpolated similarly to the convective element matrix (shown in Equation 4.8). $(1-\rho_i)$ interpolation means that void regions primarily have a Stokes flow contribution and therefore due to the presence of flow velocities the convection matrix becomes active due to its dependence of said velocities ($\mathbf{K}_{\text{C}}[\mathbf{v}]$). The solid (or full material) regions in the flow domain are dominated by the impermeable Darcy term (denoted by subscript 'Da') where the velocities of the fluid flow are approximately zero. The permeability of the Darcy term has to be tuned per mesh size. This is an iterative process and is further explained in Guest and Prévost [2006].

5.5. Optimization problem

A new constraint is introduced in to the optimization problem to control the flow performance of the fluid channels. Subsequently the optimization problem is introduced with new fluid flow contributions. Thereafter, the adjoint sensitivities of the surface deformation constraint will be treated.

5.5.1. Flow energy dissipation (pressure drop) constraint

An energy dissipation constraint on the fluid flow essentially ensures that the topology of the fluid channels allows for sufficient flow between the inlet and outlet. This can also be seen as restricting the pressure drop between the inlet and outlet. The topology optimization can at times "cave-in" the channel walls, effectively blocking the fluid flow. Energy dissipation of the fluid flow is taken from the Stokes flow system matrix and is given as:

$$c_{\text{f}} = \mathbf{v}^{\top}\mathbf{K}_{\text{S}}\mathbf{v} \tag{5.5}$$

where a low value of c_{f} would signify (perhaps counter-intuitively) "freer" flow. To limit the pressure drop would therefore require there to be a maximum permissible $c_{\text{f,max}}$. A high value of c_{f} raises the velocities, as the mass transfer remains the same for a narrowing channel. This can be incorporated into a constraint similarly to the mechanical and thermal compliance constraints:

$$g_4 = \frac{c_{\text{f}}}{c_{\text{f,max}}} - 1 \leq 0 \tag{5.6}$$

where $c_{\mathrm{f,max}}$ is the maximum permissible fluid compliance. The sensitivities of the constraints are taken as follows:

$$\frac{\partial g_4}{\partial \rho_i} = \frac{1}{c_{\mathrm{f,max}}} \mathbf{v}^\top \frac{\partial \mathbf{K}_{\mathrm{Da}}}{\partial \rho_i} \mathbf{v} \tag{5.7}$$

where the sensitivities are taken of $\mathbf{K}_{\mathrm{Da}}$, the Darcy viscosity matrix. More information is given in Appendix B.7.

In Table 5.1 a comparison of the final channel flow layout is shown for varying values of $c_{\mathrm{f,max}}$ on Model 1. The general trend shows a narrowing channel and an increase of material around the fluid inlet for a relaxing pressure drop constraint. The general channel layout beyond the inlet remains largely the same, due to the surface deformation constraint, which is satisfied when the cooling channel passes beneath the centre of Ω_{TM}. The pressure drop constraint works to provide a "clear path" from the inlet to the outlet.

Table 5.1: A comparison of the final fluid domain design for changing values of $c_{\mathrm{f,max}}$ of the energy dissipation constraint on the fluid flow. An optimization with a stringent surface deformation constraint is performed on Model 1. The domain Ω_{TM} is fully solid ($\rho = 1$) to improve homogeneity between the examples. Therefore, the optimization is only searching for a cooling channel layout (and not a thermo-mechanical structure) which provides the best surface deformation performance. Black represents solid regions and voids represent flow regions.

$c_{\mathrm{f,max}}$	215.0	215.4	215.6	215.8
	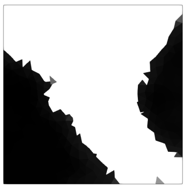	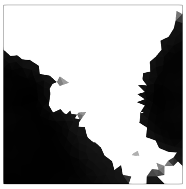	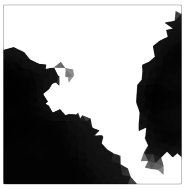	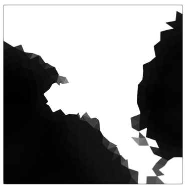

5.5.2. Optimization problem 5: Volume minimisation of a combined thermo-mechanical and thermo-fluid system

This optimization problem is based on the volume minimisation formulation of the previous chapters. In this chapter the fluid state equations and the pressure drop constraint are added:

$$\begin{aligned}
\min_{s} \quad & f = \frac{1}{V}\sum_i V_i \rho_i \\
\text{s.t.} \quad & \begin{bmatrix} \mathbf{K}_{\mathrm{DaS}} & \mathbf{B}_{\mathrm{DaS}} & \mathbf{0} & \mathbf{0} \\ \mathbf{B}_{\mathrm{DaS}}^\top & \mathbf{M}_{\mathrm{DaS}} & \mathbf{0} & \mathbf{0} \\ \mathbf{0} & \mathbf{0} & \mathbf{K}_{\mathrm{D}} + \mathbf{K}_{\mathrm{C}} & \mathbf{0} \\ \mathbf{0} & \mathbf{0} & -\mathbf{A} & \mathbf{K}_{\mathrm{U}} \end{bmatrix} \begin{bmatrix} \mathbf{v} \\ \mathbf{p} \\ \theta \\ \mathbf{u} \end{bmatrix} = \begin{bmatrix} \mathbf{f}_{\mathrm{v}} \\ \mathbf{f}_{\mathrm{p}} \\ \mathbf{q} \\ \mathbf{f} \end{bmatrix} \\
& g_1 = \frac{1}{\log_{10}(C c_{\mathrm{SD,max}})} \log_{10}\left(C\frac{1}{m}\sum_{j=1}^{m}(x_j - \bar{x}_j)^2 + 1 \right) - 1 \leq 0 \\
& g_2 = \frac{\mathbf{u}_{\mathrm{m}}^\top \mathbf{K}_{\mathrm{U}} \mathbf{u}_{\mathrm{m}}}{c_{\mathrm{u,max}}} - 1 \leq 0 \\
& g_3 = \frac{\theta^\top \mathbf{K}_{\mathrm{D}} \theta}{c_{\mathrm{t,max}}} - 1 \leq 0 \\
& g_4 = \frac{\mathbf{v}^\top \mathbf{K}_{\mathrm{S}} \mathbf{v}}{c_{\mathrm{f,max}}} - 1 \leq 0 \\
& \rho_{\min} \leq \rho \leq 1.
\end{aligned} \tag{5.8}$$

This formulation ensures a minimum effective thermal conductance and a minimum mechanical stiffness in the thermo-mechanical structure, whilst guaranteeing limited pressure drop in the fluid domain.

Adjoints of surface deformation constraint

Due to the complexity of the system, the adjoint sensitivities of the surface deformation constraint are extensive. The full derivation has been derived in Appendix B.4 for the state equations in the adjoint problem. The final adjoint sensitivities are given as:

$$\frac{\partial g_1^*}{\partial \rho_i} = \lambda_1^\top \frac{\partial \mathbf{K}_\mathrm{D}}{\partial s_i} \theta + \lambda_2^\top \left(\frac{\partial \mathbf{K}_\mathrm{U}}{\partial s_i} \mathbf{u} - \frac{\partial \mathbf{A}}{\partial s_i} \theta \right) + \lambda_3^\top \left(\frac{\partial \mathbf{K}_\mathrm{DaS}}{\partial s_i} \mathbf{v} + \frac{\partial \mathbf{B}_\mathrm{DaS}}{\partial s_i} \mathbf{p} \right) + \lambda_4^\top \left(\frac{\partial \mathbf{B}_\mathrm{DaS}^\top}{\partial s_i} \mathbf{v} + \frac{\partial \mathbf{M}_\mathrm{DaS}}{\partial s_i} \mathbf{p} \right) \tag{5.9}$$

where the adjoints are calculated by solving:

$$\begin{bmatrix} (\mathbf{K}_\mathrm{C} + \mathbf{K}_\mathrm{D})^\top & -\mathbf{A}^\top & 0 & 0 \\ 0 & \mathbf{K}_\mathrm{U}^\top & 0 & 0 \\ \left(\frac{\partial \mathbf{K}_\mathrm{C}}{\partial \mathbf{v}} \theta \right)^\top & 0 & \mathbf{K}_\mathrm{DaS}^\top & \mathbf{B}_\mathrm{DaS} \\ 0 & 0 & \mathbf{B}_\mathrm{DaS}^\top & \mathbf{M}_\mathrm{DaS}^\top \end{bmatrix} \begin{bmatrix} \lambda_1 \\ \lambda_2 \\ \lambda_3 \\ \lambda_4 \end{bmatrix} = \begin{bmatrix} 0 \\ -\frac{\partial g_1}{\partial \mathbf{u}} \\ 0 \\ 0 \end{bmatrix}. \tag{5.10}$$

The derivation of $\frac{\partial g_1}{\partial \mathbf{u}}$, the response of the constraint with respect variations of each deformation DOF is found in Appendix B.1. The term $\left(\frac{\partial \mathbf{K}_\mathrm{C}}{\partial \mathbf{v}} \theta \right)^\top$ is not quite as trivial to derive due to the dependence of the convection matrix on the velocity DOFs, which in turn are dependent on the density distribution in the fluid domain. A pseudo-code for its implementation is given in Appendix B.4.1.

5.6. Results

Firstly a comparison will be made of selectively optimizing the different domains. Thereafter the results of the topology optimization of Models 1, 2 and 3 (shown in Figure 5.4) subject to Optimization problem 5 (Equation 5.8) are shown in this section. The optimization is performed on a coarser mesh than used previously. This will inevitably lead to less definition than in previous chapters.

5.6.1. Selective domain optimization

As a test to see what impact either domain has on attaining good surface deformation performance, the domains being optimized are alternated. A surface deformation minimisation is performed on Model 1, as it allows for a better comparison to be made with regards to surface deformation performance. This can best be seen in Table 5.2 for when the thermo-mechanical domain is not optimized it is left completely solid, and for when the thermo-fluid domain is not being optimized it is left void to allow fluid flow. Because of the surface deformation objective, convergence is not as discrete as is the case in the volume minimisation, especially in the fluid domain.

The top left case, where no optimization occurs, can be seen as a benchmark. Its MSE is therefore the highest of all the cases. When only optimizing the fluid domain (top right case), the MSE improves by three orders of magnitude. The channel layout is not very clearly visible, however two "dimples" are present which very gently steer the fluid flow but also function as points for convection. One should note that the dimples are placed quite symmetrically.

When only optimizing the thermo-mechanical domain (bottom left), the MSE rises again. This suggests that optimizing the thermo-fluid domain has a greater impact on improving the MSE. Strangely, in the contact areas where the thermo-mechanical structure meets the convective boundary, the flow velocity is the lowest. As a consequence the temperature of the flow is higher, due to the poorer heat transfer caused by lower fluid velocities.

Optimizing both domains clearly shows the best results. The design space is larger which allows for more ways to improve the MSE. The thermo-mechanical-structure has changed somewhat compared to the bottom left case, and the channel layout does not share any commonalities with the top right case. The fluid flow is clearly steered to pass beneath the centre of the mirror, where it convects heat along the solid-fluid interface in the thermo-fluid domain. This case has almost achieved an order of magnitude improvement on the next best case. The temperature of the fluid flow is also seen to be much lower than the other cases, due to the improved heat transfer of the system.

This method, whereby a surface deformation objective was used, produced designs with bad definition and should therefore be seen as a mere test with interesting results. The following sections will utilise a volume minimisation objective which improves the convergence of the optimization.

Table 5.2: Comparison of selectively choosing the domains undergoing a topology optimization. In order to compare their surface deformation performance, the objective is a surface deformation minimisation and not a volume minimisation. The plots of the solid domain show the density distribution, whereas the fluid domain also shows the velocity vector, coloured with respect to the temperature of the fluid

		Thermo-fluid domain	
		Void	Optimized
Thermo-mechanical domain	Solid	TM Domain TF Domain 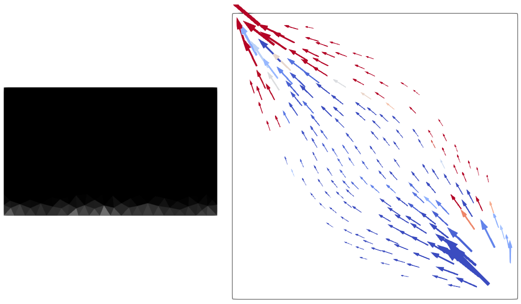 MSE = $1.2 \times 10^{-6}\,\mathrm{m}^2$	TM Domain TF Domain 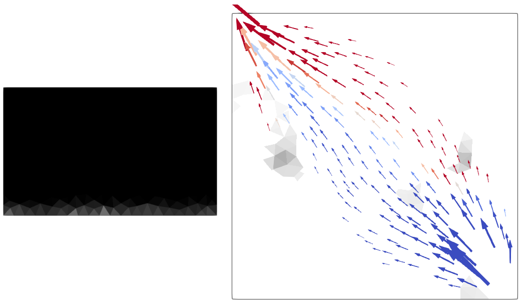 MSE = $1.2 \times 10^{-9}\,\mathrm{m}^2$
	Optimized	TM Domain TF Domain 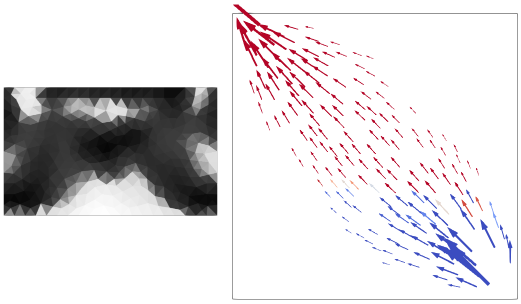 MSE = $3.5 \times 10^{-9}\,\mathrm{m}^2$	TM Domain TF Domain 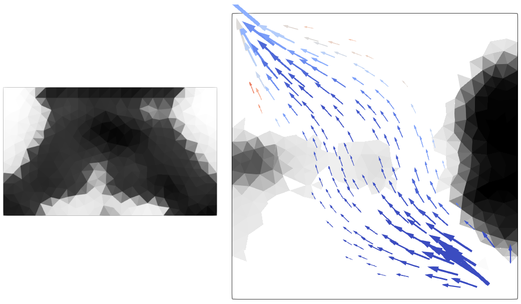 MSE = $3.0 \times 10^{-10}\,\mathrm{m}^2$

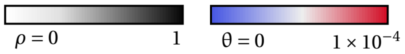

5.6.2. Model 1

The results of Optimization problem 5 performed on Model 1 are shown in Table 5.3. The thermo-mechanical domain has struggled to converge to a discrete design due to the coarser mesh, although the general makeup of the structure is partly visible. The thermo-fluid domain has however converged reasonably successfully. A distinct channel has been formed which guides the fluid flow beneath the centre of the structure. The structure however does not seem to provide a large surface area to convect heat from, rather, heat is guided down the sides of the structure to within the thermo-fluid domain, where the heat is convected along the solid-fluid interface.

5.6.3. Model 2

The results of Optimization problem 5 performed on Model 2 are shown in Table 5.4. The thermo-mechanical structure has again struggled to converge to a discrete design, although it appears to have converged to a similar design as in Table 5.3. The bottom half of the flow domain has remained largely similar: flowing directly from the inlet to the region beneath the centre of the mirror. The top half, more so than in the previous model has been diverted more aggressively towards the outlet, therefore keeping the walls slightly closer to the bulk flow. The surface deformation constraint has been met and this is reflected in the plot, although the sides of the mirror do, like in all the models, show the largest errors.

Table 5.3: Results of Optimization problem 5 performed on Model 1. Where the fluid inlet is located on the bottom right and the outlet on the top left of the fluid domain. Arrow dimensions correspond to velocity vector, and their colour correspond to the temperature of the fluid

Thermo-mechanical domain	Thermo-fluid domain	Surface deformation
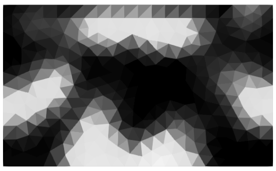	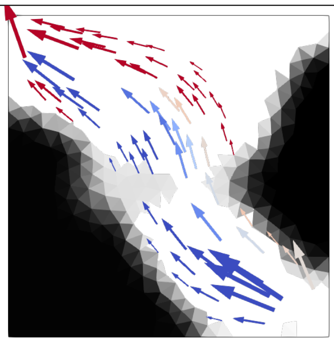	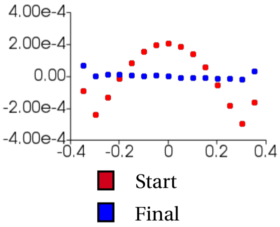

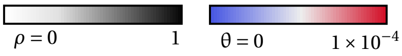

Table 5.4: Results of Optimization problem 5 performed on Model 2. Where the fluid inlet is located on the bottom right and the outlet on the top right of the fluid domain. Arrow dimensions correspond to velocity vector, and their colour correspond to the temperature of the fluid

Thermo-mechanical domain	Thermo-fluid domain	Surface deformation
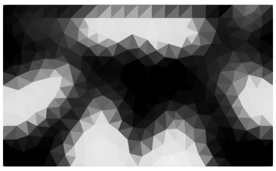	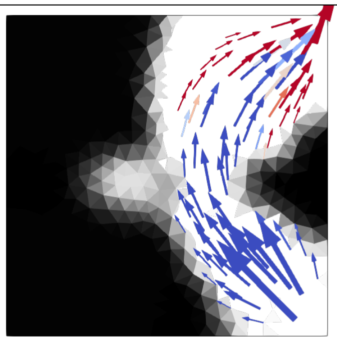	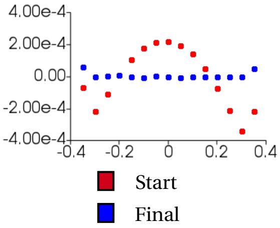

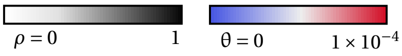

5.6.4. Model 3

The results of Optimization problem 5 performed on Model 3 are shown in Table 5.5. The thermo-mechanical structure has not changed significantly in this model compared to the last two. The cooling channel has however changed to accommodate the new outlet location. This model has similarities with the "asymmetric" model of the previous chapter, however the structure does not resemble the asymmetric designs from the previous chapter. The thermo-fluid domain has, perhaps oddly for a "volume minimisation", converged to a quite peculiar layout in the upper half of the flow domain. Its purpose is inconclusive as there is no flow in that region and it does not appear to serve any thermal purpose.

5.7. Discussion

The results of this chapter have been quite visibly inhibited by the modelling concessions made, such as the need to use a coarser mesh than in previous chapters or the pseudo 3D approach to further simplify the model. However, the method clearly shows merit, and in optimizing both the thermo-mechanical and thermo-fluid domain in tandem, it has shown to improve the surface deformations.

The thermo-mechanical structure has changed in comparison to previous chapters. This is like due to a

Table 5.5: Results of Optimization problem 5 performed on Model 3. Where the fluid inlet is located on the bottom right and the outlet on the bottom left of the fluid domain. Arrow dimensions correspond to velocity vector, and their colour correspond to the temperature of the fluid

Thermo-mechanical domain	Thermo-fluid domain	Surface deformation
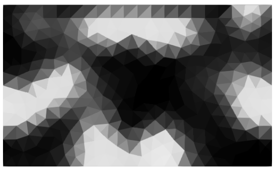	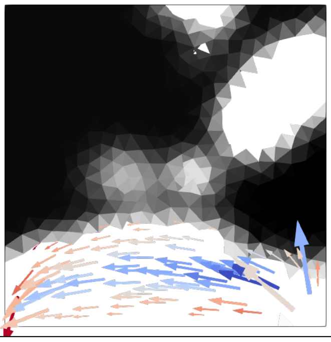	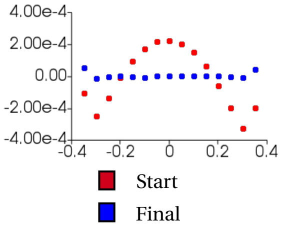

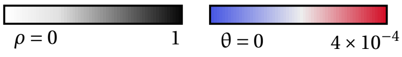

combination of the new configuration and the higher mechanical and thermal compliance constraints needed to return designs with more intricate details (reducing the permissible compliance left few details to discern). The compliance constraints were still required to prevent the mirror from detaching itself completely, therefore the values of $c_{\mathrm{u,max}}$ and $c_{\mathrm{t,max}}$ chosen were larger than previous chapters.

Heat was not convected into the fluid flow as first intended: through the bottom of the thermo-mechanical structure as in previous chapters. Instead, it was conducted through the structure and into the solid regions of the thermo-fluid domain, where it eventually convected out at the solid-fluid interface. This in itself does not disprove the work of this chapter or those previously, it simply means that the optimizer found a more volume efficient method of convecting heat. If expanded to a full 3D model this will cease to be an issue.

In Tables 5.3, 5.4 and 5.5 one may notice that the warm regions of the fluid flow are restricted to narrow areas on the outer sides of the flow channel near the outlets. This lack of thermal "mixing" along the flow cross-section is to be expected at high Péclet numbers, where the internal conduction within the fluid is low. This can be improved by reducing the Péclet number, which in practice one would have little control over. Otherwise a formulation or a constraint would be needed to try to increase the number of channels. This would as a consequence reduce the channel widths, and therefore increase the rate of convection because of the increased surface area for convection. Yaji et al. [2015] proposed a method of improving the heat transfer of a thermo-fluid system by reducing temperature deviations from the mean in the domain. However, maximising heat transfer would not necessarily improve the surface deformation performance as these two are not necessarily related. Improving heat transfer would have to be introduced as a seperate thermal performance constraint.

Further improvements could be made if the fluid inlet location would not have to be defined a priori. This may lead to a more symmetric temperature field as the inlet placement would then not have to be placed on an outer boundary but perhaps in the centre of the thermo-fluid domain.

Expanding the fluid model to the full Navier-Stokes equations could allow for more control of different flow aspects. Channel widths could then be tied to the flow conditions or non-dimensional numbers. Differentiating the Stokes and Navier-Stokes formulations is a momentum term, which is missing in the current formulation. Due to the wide channels, one may expect higher flow velocities at the outer radii of channel bends, which in turn would increase convection in these regions. It is not certain whether this would make a large impact on convection (and therefore the surface deformations), however, narrowing these channels would reduce the momentum related velocity variations.

6

Conclusions and Recommendations

In the Conclusions a general summary will be made of the research project, where the most important learning outcomes will be highlighted. Thereafter, in the Recommendations, possible directions to further the research and improve the optimization problem will be mentioned.

6.1. Conclusions

In Chapter 3, three different optimization problems for controlling the MSE of a set of surface deformations with respect to the mean displacement were tested against varying mechanical and thermal compliance constraints. Of the three optimization problems, only the last one consistently produced well converged designs by minimising the volume and constraining the surface deformations. If the aim were to produce a mirror structure with the lowest possible surface deformations, as opposed to achieving a certain performance threshold, the first two optimization problems would be needed to ascertain the surface deformation limits of any configuration, and based on this early insight a more well established choice can be made for the permissible surface deformation in the constraint formulation.

The volume minimisation objective function alone tends to designs of high mechanical compliance and high thermal resistance, undesirable performance characteristics in precision optics. Whereas the mechanical and thermal compliance constraints were first intentioned as a means to resist the inclination of the optimizer to decouple the mirror surface (the optimizer sought high compliance for improved surface deformation performance), they served the purpose in the volume minimisation of preventing the volume fraction from vanishing by imposing mechanical and thermal performance measures. The constraints also assisted in bounding the optimization problem, seen in the least stringently constrained cases, which due to the comparatively low threshold of meeting the constraints, struggles more to converge.

The MSE formulations for characterising the surface deformation performance with respect to its mean displacement worked as intended in minimising or constraining the surface deformation error. As an objective function the standard formulation of the MSE worked accordingly, however when implemented as a constraint, significant performance improvements were noticed when reformulated as a logarithm. Due to the MSE often improving by many orders of magnitude, the standard formulation would often not exhibit the required precision to converge, as the applied MMA optimizer is sensitive to constraint scaling. The broader appeal of the MSE is that it can also be used to determine the error with respect to predefined shapes or curves. This would therefore permit curved mirrors to be optimized in a similar fashion, broadening the scope with which the MSE can be utilised as an objective or constraint.

In Chapter 4 the heat sink was removed and replaced with a cooling channel to extract heat from the system. The location of the fluid flow was fixed throughout the optimization, however it was introduced in two different orientations: out-of-plane and in-plane. The first flow direction labelled, the "symmetric" model, functioned primarily as a link to the previous chapter, and sought to validate whether the models differed greatly when the method of heat extraction was changed. The second flow direction labelled, the "asymmetric" model, tested how the optimizer would perform when the "caloric" effect of the warming fluid channel was present. The asymmetric temperature field in the model lead to asymmetric designs. However the asymmetry becomes less noticeable when the surface deformation constraint is made more stringent. This would imply that structure symmetry helps in attaining flat designs.

Both models were tested against the non-dimensional Péclet number as a means of varying the rate of heat transfer into the fluid. Lower Péclet values produced designs with lower effective thermal resistance (larger cross-sections) to meet the thermal compliance constraint, whereas the higher Péclet values satisfied the thermal compliance constraint with a higher effective resistance (smaller cross-sections). This could be expected as a higher heat transfer would reduce the temperature gradient between the mirror and the flow channel, allowing the thermal compliance constraint to be met with a smaller cross-section.

The "symmetric" model was further used to investigate the effect on the final design when the cooling channel was sub-divided and spread out. Design uniformity was very consistent after the first sub-division, where the majority of the structure remained largely identical until just before reaching the cooling channels, where the thermal members branched away to the cooling channels.

In Chapter 5 the fluid domain was expanded and included as a design domain in the topology optimization. Optimizing both the thermo-mechanical structure and cooling channel together were shown to provide better results than just optimizing each part individually. This is due to the truly *holistic* and integrated nature of the approach, which allows the two domains to work together to produce topologies which minimise the surface deformation error. A clear difference was seen in the resulting topologies when the integrated approach is used as opposed to individually optimizing the different parts.

Three further models were studied with varying inlet and outlet locations, which showed the resulting cooling channel adapt to each flow configuration. The thermo-mechanical structure only featured subtle variations between the different flow configurations. This was mainly due to the fact that the optimizer found the highest performance in prioritising heat transfer to the fluid through sidewalls of the cooling channels. Heat would therefore be conducted into the solid regions of the thermo-fluid domain through the solid-solid interface between the two domains. This interface location was largely the same between the different models, leading to a the thermo-mechanical structure that was largely the same.

6.2. Recommendations

For the aim of industrialising the approach shown in Chapter 5 where both the thermo-mechanical and thermo-fluid domains are optimized in tandem, certain improvements have to be made. These improvements mainly concern implementation, where currently, computation time and memory limits are the main inhibitors to expanding the problem into a full 3D model.

- The current code is limited to single-core implementation, which will most likely have to be rewritten or another package has to be found that can be deployed across multiple processors. A more powerful computational framework is needed to enable higher resolutions and 3D problems.
- The domain size, and more importantly the spacing (in the undeformed/reference state) between the mirror and the heat sink were kept constant throughout the thesis. The optimizer cannot currently change these dimensions, which may be of interest. Reducing the spacing between the mirror and heat sink would lower temperatures on the mirror surface due to the reduced effective thermal resistance in the system. In a transient setting one would see a reduction in time constants by doing this. However, local temperature gradient effects become more visible on the mirror surface as the this gap closes in, due to the point source nature of the cooling channels.
- Expanding the optimization to a transient problem would be of interest to test surface deformation performance under varying temperature loads, or more specifically to test the response to certain temperature frequency variations. Preliminary tests can be made with the current model results under varying static loads. The predominant deformation would be the piston mode - the up and down motion of the entire structure. However, of interest to optical performance would be whether higher mode deformations would emerge, resulting in the optical performance to be negatively affected. To improve the static performance under different heat loads, one could incorporate a method in to the optimization problem which can account for multiple static temperature fields [Li et al., 2001]. Otherwise, a first step towards incorporating the transient effects could be achieved with the equivalent static load

method. Here the temperature field mimics a dynamic heat load at multiple time steps [Park and Kang, 2003; Zhuang and Xiong, 2015]. This method has been seen in structural mechanics and thermal conduction, but not yet applied to thermal-mechanics or convection. No issues would be expected, however, academically it would be of interest to again carefully build up the model (similar to Chapters 3-5) to see the resulting topologies of transient contributions of the different physics. The computation time of transient problems could form a considerable obstacle. In Appendix F, a showcase of the modal decomposition of the advection-diffusion equation is shown in a 1D and 2D setting. This can be seen as a first step towards a transient approach using *modal order reduction*.

- Another method of reducing the computational size of the optimization could be to exploit model symmetries. By choosing domain configurations which can be sub-divided into thirds using axisymmetry (this would require translating the model in to polar coordinates) or quarters (where a normal cartesian grid is used), significant reductions could be made to the problem size. The most significant changes that would arise would be symmetric flow layouts. Where one would most likely position the inlet at the centre of the symmetrical domain, requiring an outlet be defined for each portion of the sub-divided domain.

  This is contrary to the status quo, where normally heat extraction from mirrors is performed with spiral like flow layouts which are used to bring upon the most uniform temperature distributions in fully solid mirror structures [Dye et al., 1982; Mansell and Force, 1973]. However topology optimization is unlikely to form spiral topologies. To achieve this, hybrid techniques would have to be developed [Wang et al., 2015] and moreover the need for spiral flow layouts would also be unlikely. This is mainly due to material placement as seen in the final density distributions of the optimization flow channels, rarely covering the full available surface area (although this could also be due to parameter choice).

- Current material penalisation only appears to provide well converged designs in the thermo-mechanical domain when a volume minimisation objective is applied to a fine mesh. In the thermo-fluid domain, a volume minimisation is not ideal as one would prefer to maximise the volume fraction in order to have more predictable and uniform control of the channel widths by varying the pressure drop constraint. The limits of the present formulation can be seen when optimizing the cooling channels, where the channel widths in the thermo-fluid domain are not so much widened as obstructions between the inlet and outlet removed. After passing the mirror plane, the need to accurately channel the fluid flow to meet the surface deformation constraint is superseded by the need to reduce the volume in the thermo-fluid domain. The channel therefore widens considerably, as this has little consequence on the surface deformations. Although this does not have a negative impact on the surface deformations, the fact that both the volume minimisation and pressure drop constraint aim to widen the channels, means that there is likely to remains a feature with the current forumlation. Constraining both the minimum and maximum pressure drop resulted in the entire thermo-fluid domain taking on different shades of grey, making convergence even worse.

  It may therefore be of interest to reformulate the optimization problem to multiple objectives, where a volume minimisation is sought in the thermo-mechanical domain and a volume maximisation in the thermo-fluid domain. Incorporating such a formulation in to the optimization problem would benefit convergence in both domains as opposed to just the one as done currently.

- A mechanical force is currently in place on the mirror surface to cause the deformation for the mechanical compliance constraint. The magnitude of the force used in all the examples was set at a very low value, to ensure the main deformation was caused by the thermo-mechanical deformation. Although this worked quite successfully in producing results with a set mechanical compliance in the direction of the force, it may be of interest to replace the force with gravity. This would mean that the body force becomes design variable dependent, which would add a term to the adjoint sensitivities of the surface deformation constraint and change the formulation of the mechanical compliance constraints from $\mathbf{u}_{\mathrm{M}}^{\top}\mathbf{K}_{\mathrm{U}}\mathbf{u}_{\mathrm{M}}$ to $\mathbf{u}_{\mathrm{M}}^{\top}\mathbf{f}$.

A

Finite element discretisations

The aim in this section is to show the discretisations of the different partial differential equations used in the topology optimization.

The mesh used in the 2D problems are composed of unstructured 't3' or triangular elements. The 3D mesh is composed of unstructured 'T4' or tetrahedral elements. Both meshes use P1 linear elements which coincides with one node per point of the element.

A.1. Thermo-mechanical

This discretisation is based on the work of Rixen [2011] and adapted for the steady state. The derivation starts with stating the conservation of energy in domain Ω is:

$$\frac{\partial q_i}{\partial x_i} - Q = 0 \quad \text{in}\,\Omega \tag{A.1}$$

Thermal energy Q is therefore equal to the gradient $\frac{\partial}{\partial x_i}$ of flux q_i. For isotropic materials we assume that flux is relative to k the isotropic conductivity and $\frac{\partial T}{\partial x_i}$ the temperature gradient as $q_i = -k\frac{\partial T}{\partial x_i}$, therefore the thermal equation can be written as:

$$-\frac{\partial}{\partial x_i} k \frac{\partial T}{\partial x_i} = Q \quad \text{in}\,\Omega \tag{A.2}$$

Discretisation of the temperature field takes the following form: $T(x_1, x_2, x_3) = \mathbf{N}(x_1, x_2, x_3)\mathbf{T}$. Where $\mathbf{N}$ are the shape functions and $\mathbf{T}$ the nodal temperature values. Substituting this into A.2 and adding the error contribution of discretisation both in the domain Ω and at the boundary Γ:

$$\begin{aligned} -\frac{\partial}{\partial x_i} k \frac{\partial \mathbf{N}}{\partial x_i}\mathbf{T} &= Q + q_{\text{error},\Omega} \quad \text{in}\,\Omega \\ -kn_i \frac{\partial \mathbf{N}}{\partial x_i}\mathbf{T} + q_{\text{error},\Gamma} &= q_s \quad \text{on}\,\Gamma_{\text{influx}} \end{aligned} \tag{A.3}$$

The second equation is the flux normal to the boundary. By projecting the flux error over the domain and boundaries gives:

$$\begin{aligned} \int_\Omega \mathbf{N}^\top q_{\text{error},\Omega}\,\mathrm{d}\Omega + \int_{\Gamma_{\text{influx}}} \mathbf{N}^\top q_{\text{error},\Gamma}\,\mathrm{d}\Gamma = 0 \\ \int_\Omega \mathbf{N}^\top \left(-\frac{\partial}{\partial x_i} k \frac{\partial \mathbf{N}}{\partial x_i}\mathbf{T} - Q\right)\mathrm{d}\Omega + \int_\Gamma \mathbf{N}^\top \left(q_s + kn_i \frac{\partial \mathbf{N}}{\partial x_i}\mathbf{T}\right)\mathrm{d}\Gamma = 0 \end{aligned} \tag{A.4}$$

Performing integration by parts introduces a new term $\mathbf{B}$ the derivatives of the shape equations gives:

$$\int_\Omega \mathbf{B}^\top k\mathbf{B}\,\mathrm{d}\Omega\,\mathbf{T} = \int_\Omega \mathbf{N}^\top Q\,\mathrm{d}\Omega - \int_\Gamma \mathbf{N}^\top q_s\,\mathrm{d}\Gamma \tag{A.5}$$

Equation A.5 is the discretised equation for flux propagation through a domain. The temperature now has to be linked to thermal expansion through the system. And we can expand Hooke's law to include the thermal expansion contribution for strain and stress:

$$\begin{aligned} \varepsilon &= \mathbf{H}^{-1}\boldsymbol{\sigma} + \boldsymbol{\alpha}(T - T_{\text{ref}}) \\ \boldsymbol{\sigma} &= \mathbf{H}\varepsilon - \mathbf{H}\boldsymbol{\alpha}(T - T_{\text{ref}}) \end{aligned} \tag{A.6}$$

Where **H** is Hooke's matrix and $\boldsymbol{\alpha} = \begin{bmatrix} \alpha & \alpha & \alpha & 0 & 0 & 0 \end{bmatrix}$ the thermal expansion vector where the last three zero values show that there are no contributions to shear.

Based on A.5 and A.6 where we take $\theta = (\mathbf{T} - T_{\text{ref}})$ the relative temperature and **u** the displacements, the discretised matrix formulations can be written as:

$$\begin{bmatrix} \mathbf{K}_{\text{D}} & \mathbf{0} \\ -\mathbf{A} & \mathbf{K}_{\text{U}} \end{bmatrix} \begin{bmatrix} \theta \\ \mathbf{u} \end{bmatrix} = \begin{bmatrix} \mathbf{q} \\ \mathbf{f} \end{bmatrix} \tag{A.7}$$

Where the matrix definitions are:

$$\mathbf{K}_{\text{D}} = \int_{\Omega} \mathbf{B}_{\theta}^{\top} k \mathbf{B}_{\theta} \, \mathrm{d}\Omega \qquad \mathbf{A} = \int_{\Omega} \mathbf{B}_{u}^{\top} \mathbf{H} \boldsymbol{\alpha} \mathbf{N}_{\theta} \mathrm{d}\Omega \qquad \mathbf{q} = \int_{\Omega} \mathbf{N}_{\theta}^{\top} Q \, \mathrm{d}\Omega - \int_{\Gamma} \mathbf{N}_{\theta}^{\top} q_s \, \mathrm{d}\Gamma \tag{A.8}$$

Where from now on we will designate $\mathbf{K}_{\text{D}}$ the diffusivity (conduction) matrix, **A** thermal expansion matrix and $\mathbf{K}_{\text{U}}$ the mechanical stiffness matrix. Where the force terms are **q** the flux and **f** the mechanical forces.

A.2. Advection-diffusion

This discretisation is based on the work of Zienkiewicz et al. [2014]. It involves discretising the steady state transport equations and eventually introducing the temperature term. The balance equation uses the generalised term ϕ and contains contributions from convection and diffusion:

$$v_i \frac{\partial \phi}{\partial x_i} - \frac{\partial}{\partial x_i}\left(k \frac{\partial \phi}{\partial x_i}\right) + Q = 0 \tag{A.9}$$

ϕ can be rewritten in terms of its shape function **N** and approximation $\tilde{\boldsymbol{\phi}}$:

$$\phi \approx \hat{\phi} = \mathbf{N}\hat{\phi} = \sum N_a \tilde{\phi}_a \tag{A.10}$$

Presented in matrix form as $\mathbf{H}\tilde{\boldsymbol{\phi}} = \mathbf{q}$ where the matrix **H** and vector **q** are:

$$\begin{aligned} H_{ab} &= \int_{\Omega} \left(\underbrace{W_a v_i \frac{\partial N_b}{\partial x_i}}_{\mathbf{K}_{\text{C}}} + \underbrace{\frac{\partial W_a}{\partial x_i} k \frac{\partial N_b}{\partial x_i}}_{\mathbf{K}_{\text{D}}} \right) \mathrm{d}\Omega \\ f_a &= \int_{\Omega} W_a Q \, \mathrm{d}\Omega + \int_{\Gamma_q} W_a \bar{q}_n \, \mathrm{d}\Gamma \end{aligned} \tag{A.11}$$

here W_a is the weighting function. Important to note is that the convection matrix $\mathbf{K}_{\text{C}}$ is asymmetric. The conduction matrix $\mathbf{K}_{\text{D}}$ is the same as that mentioned in the A.1.

A.3. Flow

Stokes flow is derived from Donea and Huerta [2005]; Masud and Hughes [2002] where the convective term in the Navier-Stokes is negated due to the highly viscous assumption of the flow. This leaves us with the following starting partial differential equation for Stokes flow in the steady state and the mass-conservation term:

$$\begin{aligned} -\nu\nabla^2\mathbf{v} + \nabla p &= \mathbf{b} \quad \text{in } \Omega \\ \nabla \cdot \mathbf{v} &= 0 \quad \text{in } \Omega \\ \mathbf{v} &= \mathbf{v}_{\text{D}} \quad \text{on } \Gamma_D \\ -p\mathbf{n} + \nu(\mathbf{n}\cdot\nabla)\mathbf{v} &= \mathbf{t} \quad \text{on } \Gamma_N \end{aligned} \tag{A.12}$$

where ν is the kinematic viscosity, **v** the velocity vector, p the pressure, **b** a force term applied to the volume, **n** the normal unit vector to the boundary and **t** a pseudo-traction. Although pressure has no effect on convection, it is needed as an extra "degree of freedom to satisfy the incompressibility constraint". The last two terms are boundary terms where the first are the prescribed velocities which can be seen as a Dirichlet condition, the last term is the Neumann condition.

$$\begin{aligned} \underbrace{\int_{\Omega} \nabla \mathbf{w} : \nu \nabla \mathbf{v} \, \mathrm{d}\Omega}_{\mathbf{K}_{\mathrm{S}}} \underbrace{- \int_{\Omega} p \nabla \cdot \mathbf{w} \, \mathrm{d}\Omega}_{\mathbf{B}} &= \underbrace{(\mathbf{w}, \mathbf{b}) + (\mathbf{w}, \mathbf{t})_{\Gamma_N} - (\mathbf{w}, \mathbf{v}_D)}_{\mathbf{f}_{\mathrm{v}}} \\ \underbrace{- \int_{\Omega} q \nabla \cdot \mathbf{v} \, \mathrm{d}\Omega}_{\mathbf{B}^{\top}} &= \underbrace{-b(\mathbf{v}_D, q)}_{\mathbf{f}_{\mathrm{p}}} \end{aligned} \tag{A.13}$$

where we define **w** and q as the associated weighting functions of **v** and p. This gives the following matrix representation:

$$\begin{bmatrix} \mathbf{K}_{\mathrm{S}} & \mathbf{B} \\ \mathbf{B}^{\top} & \mathbf{0} \end{bmatrix} \begin{bmatrix} \mathbf{v} \\ \mathbf{p} \end{bmatrix} = \begin{bmatrix} \mathbf{f}_{\mathrm{v}} \\ \mathbf{f}_{\mathrm{p}} \end{bmatrix} \tag{A.14}$$

Here **B** is the gradient operator and $\mathbf{B}^{\top}$ the divergence operator. Because of the use of linear elements a stabilisation term is added to the Stokes flow formulation. This term is also derived from Donea and Huerta [2005] but originates from Hughes et al. [1986] and its purpose is to keep the system matrix positive definite. The method described here is the Galerkin/Least-Squares (GLS) method.which has two contributions **L** and **M** in literature but only the latter that need be implemented because of the use of linear FEM elements. **M** is introduced as follows:

$$\begin{bmatrix} \mathbf{K}_{\mathrm{S}} & \mathbf{B} \\ \mathbf{B}^{\top} & \mathbf{M} \end{bmatrix} \begin{bmatrix} \mathbf{v} \\ \mathbf{p} \end{bmatrix} = \begin{bmatrix} \mathbf{f}_{\mathrm{v}} \\ \mathbf{f}_{\mathrm{p}} \end{bmatrix} \tag{A.15}$$

Where the element matrix of the stabilisation term **M** is defined as follows:

$$\mathbf{m}^e_{ab} = \frac{\alpha^e (h^e)^2}{4\mu} \int_{\Omega^e} \sum_{k=1}^{n_{\mathrm{sd}}} (N^e_{a,k}, N^e_{b,k}) \, \mathrm{d}\Omega. \tag{A.16}$$

The stabilisation term is in fact the negative discrete Laplacian. Here we have introduced a few terms which need to be defined, e represents element notation, a and b represent the local pressure-element node numbers, α is stabilisation parameter set to 1/3, h the element length, μ the dynamic viscosity, n_{sd} is the number of spatial dimensions, N are the shape functions associated with pressure-element node a or b.

For topology optimization of the fluid channels, Darcy flow is modelled in parallel with Stokes flow with a linear interpolation between the two types of flow. Darcy is characterised as a highly viscous flow which is introduced into the fluid domain to avoid having to introduce internal force regions to satisfy Stokes flow. This *braking* effect essentially channels fluid to flow around regions where the Darcy term is predominant. Borrvall and Petersson [2003] originally used this combination of flow regimes based on Sanchez-Palencia [1980] work on homogenisation of Darcy flow. Subsequently Guest and Prévost [2006] provided the matrix formulation based on the following partial differential equation:

$$\begin{aligned} \Big((1-\rho)\mu\nabla^2 - \rho\frac{\mu}{\kappa}\mathbf{I}\Big)\mathbf{v} - \nabla p &= \rho_f \mathbf{b} \\ \nabla \cdot \mathbf{v} &= 0 \end{aligned} \tag{A.17}$$

Where Stokes flow dominates in void regions and Darcy in solid regions. Integrating this into matrix representation:

$$\begin{bmatrix} \mathbf{K}_{\mathrm{DaS}} & \mathbf{B}_{\mathrm{DaS}} \\ \mathbf{B}^{\top}_{\mathrm{DaS}} & \mathbf{M}_{\mathrm{DaS}} \end{bmatrix} \begin{bmatrix} \mathbf{v} \\ \mathbf{p} \end{bmatrix} = \begin{bmatrix} \mathbf{f}_{\mathrm{vDaS}} \\ \mathbf{f}_{\mathrm{pDaS}} \end{bmatrix} \tag{A.18}$$

Where the element matrices are:

$$\begin{aligned} \mathbf{k}^e_{\mathrm{DaS}}(\rho^e) &= \big((1-\rho^e)\mathbf{k}^e_{\mathrm{F}} + \rho^e \mathbf{k}^e_{\mathrm{D}}\big) \\ \mathbf{b}^e_{\mathrm{DaS}}(\rho^e) &= \big((1-\rho^e)\mathbf{b}^e + \rho^e \mathbf{b}^e_{\mathrm{D}}\big) \\ \mathbf{b}^{e^{\top}}_{\mathrm{DaS}}(\rho^e) &= \Big((1-\rho^e)\mathbf{b}^{e^{\top}} + \rho^e \mathbf{b}^{e^{\top}}_{\mathrm{D}}\Big) \\ \mathbf{m}^e_{\mathrm{DaS}}(\rho^e) &= \big((1-\rho^e)\mathbf{m}^e + \rho^e \mathbf{m}^e_{\mathrm{D}}\big) \end{aligned} \tag{A.19}$$

And the force term are computed as follows:

$$\mathbf{f}_{v\mathrm{DaS}}(\rho^e) = \rho_f \mathbf{b}_v - \underset{e}{\mathbf{A}}\left(\mathbf{k}^e_{\mathrm{DaS}}(\rho^e)\mathbf{g}^e_v\right) \tag{A.20}$$

where ρ_f is the fluid density, $\mathbf{b}_v$ the body forces per unit volume, $\mathbf{g}^e$ the prescribed velocity boundary conditions and $\underset{e}{\mathbf{A}}$ the assembly operator.

B

Derivation of sensitivities

B.1. Surface deformations

The adjoint problem R^* contains the objective function previously referred to as f and referred to in this appendix as R. Two variations of the surface deformation objective are used in this work. Both based on the means square error (MSE) where the logarithm is taken of the alternative method to better cope with the orders of magnitude improvement in the objective function. The method proposed by Haftka [1981] is used as a standard format: $R^* = R + \boldsymbol{\lambda}^\top \cdot (...)$ where the dot product is taken between $\boldsymbol{\lambda}$, a vector containing the system adjoints, and the state equations.

Starting with the MSE objective:

$$\mathrm{R} = \frac{1}{m} \sum_{j=1}^{m} (x_j - \bar{x}_j)^2 \tag{B.1}$$

which in the vector notation is given as:

$$R = \frac{1}{n} (\mathbf{u}_{\mathrm{sel}} - \bar{u}_{\mathrm{sel}})^\top (\mathbf{u}_{\mathrm{sel}} - \bar{u}_{\mathrm{sel}}) \tag{B.2}$$

For the adjoint sensitivities we have to write both $\mathbf{u}_{\mathrm{sel}}$ and $\bar{u}_{\mathrm{sel}}$ in terms of $\mathbf{u}$ the entire displacement vector. Starting with $\mathbf{u}_{\mathrm{sel}}$ this can be seen as:

$$\mathbf{u}_{\mathrm{sel}} = \mathbf{Z}\mathbf{u} \tag{B.3}$$

where $\mathbf{Z}$ is a very sparse selection matrix where both sides are as long as the total number of displacement DOFs, with ones on the diagonals for displacements taken into consideration in the objective.

$\bar{u}_{\mathrm{sel}}$ is displayed in the optimization function as a scalar value, however it is rewritten as a vector with entries located as in $\mathbf{u}_{\mathrm{sel}}$. Rewriting in terms of $\mathbf{u}$:

$$\begin{aligned} \bar{u}_{\mathrm{sel}} &= \frac{1}{n} \mathbf{Z}\mathbf{1}(\mathbf{1}^\top \mathbf{Z}\mathbf{u}) \\ &= \frac{1}{n} \mathbf{z}(\mathbf{z}^\top \mathbf{u}) \end{aligned} \tag{B.4}$$

here n is the number of active displacement DOFs which can also be seen as $n = \mathrm{tr}(\mathbf{Z})$, $\mathbf{1}$ is a ones vector as long as the total number of displacement DOFs. $\mathbf{z}$ has been introduced which is the selection matrix in vector form: $\mathbf{z} = \mathbf{Z}\mathbf{1}$. The objective function can therefore be rewritten as:

$$R = (\mathbf{Z}\mathbf{u} - \frac{1}{n} \mathbf{Z}\mathbf{1}(\mathbf{1}^\top \mathbf{Z}\mathbf{u}))^\top (\mathbf{Z}\mathbf{u} - \frac{1}{n} \mathbf{Z}\mathbf{1}(\mathbf{1}^\top \mathbf{Z}\mathbf{u})) \tag{B.5}$$

For the sensitivities of the response function the displacement term $\mathbf{u}$ has to be taken into account. The response function sensitivity is a function of the displacements $R[\mathbf{u}[s], s]$ therefore the sensitivities are rewritten using the chain rule: $\frac{\partial R}{\partial \rho_i} = \frac{\partial R}{\partial \mathbf{u}} \frac{\partial \mathbf{u}}{\partial \rho_i}$.

$$\begin{aligned}\frac{\partial R}{\partial \mathbf{u}} \frac{\partial \mathbf{u}}{\partial \rho_i} &= 2(\mathbf{Zu} - \frac{1}{n}\mathbf{Z1}(\mathbf{1}^\top \mathbf{Zu}))^\top \ \frac{\partial}{\partial \mathbf{u}}(\mathbf{Zu} - \frac{1}{n}\mathbf{Z1}(\mathbf{1}^\top \mathbf{Zu}))\frac{\partial \mathbf{u}}{\partial \rho_i} \\ &= 2\underbrace{(\mathbf{Zu} - \frac{1}{n}\mathbf{Z1}(\mathbf{1}^\top \mathbf{Zu}))^\top}_{\textbf{vector}} \ \underbrace{(\mathbf{Z} - \frac{1}{n}\mathbf{Z1}(\mathbf{1}^\top \mathbf{Z}))}_{\textbf{matrix}}\frac{\partial \mathbf{u}}{\partial \rho_i}\end{aligned} \tag{B.6}$$

The logarithmic objective is given as:

$$R_{\log} = \log_{10}(CR + 1) \tag{B.7}$$

where C is a constant which is used to scale R in the first optimization iteration to equal one: $C = 1/R_0$. The objective sensitivity of the logarithm is given as:

$$\frac{\partial R_{\log}}{\partial \mathbf{u}} \frac{\partial \mathbf{u}}{\partial \rho_i} = \frac{1}{\ln 10} \frac{C}{CR+1} \frac{\partial R}{\partial \mathbf{u}} \frac{\partial \mathbf{u}}{\partial \rho_i} \tag{B.8}$$

where $\ln 10$ is the natural logarithm of 10.

B.2. Adjoint sensitivities thermo-mechanical problem

The adjoint response function for the thermo-mechanical problem solely:

$$R^* = R + \lambda_1^\top \left(\mathbf{K}_\mathrm{D}\theta - \mathbf{q}\right) + \lambda_2^\top \left(\mathbf{K}_\mathrm{U}\mathbf{u} - \mathbf{A}\theta - \mathbf{f}\right) \tag{B.9}$$

where λ_1 and λ_2 are the adjoints associated to the temperature and displacement DOFs respectively. Taking the derivatives with respect to the design variables ρ_i:

$$\frac{\partial R^*}{\partial \rho_i} = \frac{\partial R}{\partial \mathbf{u}} \frac{\partial \mathbf{u}}{\partial \rho_i} + \lambda_1^\top \left(\frac{\partial \mathbf{K}_\mathrm{D}}{\partial \rho_i}\theta + \mathbf{K}_\mathrm{D}\frac{\partial \theta}{\partial \rho_i}\right) + \lambda_2^\top \left(\frac{\partial \mathbf{K}_\mathrm{U}}{\partial \rho_i}\mathbf{u} + \mathbf{K}_\mathrm{U}\frac{\partial \mathbf{u}}{\partial \rho_i} - \frac{\partial \mathbf{A}}{\partial \rho_i}\theta - \mathbf{A}\frac{\partial \theta}{\partial \rho_i}\right) \tag{B.10}$$

Grouping the derivatives of like DOFs and setting to zero gives:

$$\begin{aligned}\frac{\partial \theta}{\partial \rho_i} \quad &\rightarrow \quad \lambda_1^\top \mathbf{K}_\mathrm{D} - \lambda_2^\top \mathbf{A} = 0 \\ \frac{\partial \mathbf{u}}{\partial \rho_i} \quad &\rightarrow \quad \frac{\partial R}{\partial \mathbf{u}} + \lambda_2^\top \mathbf{K}_\mathrm{U} = 0\end{aligned} \tag{B.11}$$

The adjoints are then calculated by solving for the above:

$$\begin{bmatrix}\mathbf{K}_\mathrm{D}^\top & -\mathbf{A}^\top \\ \mathbf{0} & \mathbf{K}_\mathrm{U}^\top\end{bmatrix}\begin{bmatrix}\lambda_1 \\ \lambda_2\end{bmatrix} = \begin{bmatrix}\mathbf{0} \\ -\frac{\partial R}{\partial \mathbf{u}}\end{bmatrix} \tag{B.12}$$

And the adjoint sensitivities can therefore be written as:

$$\frac{\partial R^*}{\partial \rho_i} = \lambda_1^\top \frac{\partial \mathbf{K}_\mathrm{D}}{\partial \rho_i}\theta + \lambda_2^\top \left(\frac{\partial \mathbf{K}_\mathrm{U}}{\partial \rho_i}\mathbf{u} - \frac{\partial \mathbf{A}}{\partial \rho_i}\theta\right) \tag{B.13}$$

B.3. Adjoint sensitivities thermo-mechanical and convection problem

The adjoint response function for the thermo-mechanical and convection problem is:

$$R^* = R + \lambda_1^\top \left((\mathbf{K}_\mathrm{C} + \mathbf{K}_\mathrm{D})\theta - \mathbf{q}\right) + \lambda_2^\top \left(\mathbf{K}_\mathrm{U}\mathbf{u} - \mathbf{A}\theta - \mathbf{f}\right) \tag{B.14}$$

As in appendix B.2 the adjoints λ_1 and λ_2 are associated to the temperature and displacement DOFs respectively. Although $\mathbf{K}_\mathrm{C}$ is dependent on the velocity field $\mathbf{v}$, the velocities do not vary with respect to the design variables in this version of the topology optimization. Taking the adjoint sensitivities gives:

$$\frac{\partial R^*}{\partial \rho_i} = \frac{\partial R}{\partial \mathbf{u}} \frac{\partial \mathbf{u}}{\partial \rho_i} + \lambda_1^\top \left(\left(\frac{\partial \mathbf{K}_\mathrm{C}}{\partial \rho_i} + \frac{\partial \mathbf{K}_\mathrm{D}}{\partial \rho_i}\right)\theta + (\mathbf{K}_\mathrm{C} + \mathbf{K}_\mathrm{D})\frac{\partial \theta}{\partial \rho_i}\right) + \lambda_2^\top \left(\frac{\partial \mathbf{K}_\mathrm{U}}{\partial \rho_i}\mathbf{u} + \mathbf{K}_\mathrm{U}\frac{\partial \mathbf{u}}{\partial \rho_i} - \frac{\partial \mathbf{A}}{\partial \rho_i}\theta - \mathbf{A}\frac{\partial \theta}{\partial \rho_i}\right) \tag{B.15}$$

Grouping the derivatives of the DOFs together gives:

$$\begin{aligned} \frac{\partial \theta}{\partial \rho_i} &\quad \rightarrow \quad \lambda_1^\top (\mathbf{K}_\mathrm{C} + \mathbf{K}_\mathrm{D}) - \lambda_2^\top \mathbf{A} = 0 \\ \frac{\partial \mathbf{u}}{\partial \rho_i} &\quad \rightarrow \quad \frac{\partial R}{\partial \mathbf{u}} + \lambda_2^\top \mathbf{K}_\mathrm{U} = 0 \end{aligned} \tag{B.16}$$

The adjoints are then calculated by solving for the above:

$$\begin{bmatrix} (\mathbf{K}_\mathrm{C} + \mathbf{K}_\mathrm{D})^\top & -\mathbf{A}^\top \\ \mathbf{0} & \mathbf{K}_\mathrm{U}^\top \end{bmatrix} \begin{bmatrix} \lambda_1 \\ \lambda_2 \end{bmatrix} = \begin{bmatrix} \mathbf{0} \\ -\frac{\partial R}{\partial \mathbf{u}} \end{bmatrix} \tag{B.17}$$

And the adjoint sensitivities can therefore be written as:

$$\frac{\partial R^*}{\partial \rho_i} = \lambda_1^\top \left(\frac{\partial \mathbf{K}_\mathrm{C}}{\partial \rho_i} + \frac{\partial \mathbf{K}_\mathrm{D}}{\partial \rho_i} \right) \theta + \lambda_2^\top \left(\frac{\partial \mathbf{K}_\mathrm{U}}{\partial \rho_i} \mathbf{u} - \frac{\partial \mathbf{A}}{\partial \rho_i} \theta \right) \tag{B.18}$$

B.4. Adjoint sensitivities thermo-mechanical, convection and flow problem

The adjoint response function of the thermo-mechanical, convection and flow problem is:

$$\begin{aligned} R^* = R &+ \lambda_1^\top \left((\mathbf{K}_\mathrm{C}[\mathbf{v}[s], s] + \mathbf{K}_\mathrm{D}) \theta - \mathbf{q} \right) \\ &+ \lambda_2^\top \left(\mathbf{K}_\mathrm{U} \mathbf{u} - \mathbf{A} \theta - \mathbf{f} \right) \\ &+ \lambda_3^\top \left(\mathbf{K}_\mathrm{F} \mathbf{v} - \mathbf{B} \mathbf{p} - \mathbf{f}_\mathrm{v} \right) \\ &+ \lambda_4^\top \left(\mathbf{B}^\top \mathbf{v} + \mathbf{M} \mathbf{p} - \mathbf{f}_\mathrm{p} \right) \end{aligned} \tag{B.19}$$

The sensitivities of the full optimization problem are:

$$\begin{aligned} \frac{\partial R^*}{\partial \rho_i} = \frac{\partial R}{\partial \mathbf{u}} \frac{\partial \mathbf{u}}{\partial \rho_i} &+ \lambda_1^\top \left(\left(\frac{\partial \mathbf{K}_\mathrm{C}[\mathbf{v}[s], s]}{\partial \rho_i} + \frac{\partial \mathbf{K}_\mathrm{D}}{\partial \rho_i} \right) \theta + (\mathbf{K}_\mathrm{C} + \mathbf{K}_\mathrm{D}) \frac{\partial \theta}{\partial \rho_i} \right) \\ &+ \lambda_2^\top \left(\frac{\partial \mathbf{K}_\mathrm{U}}{\partial \rho_i} \mathbf{u} + \mathbf{K}_\mathrm{U} \frac{\partial \mathbf{u}}{\partial \rho_i} - \frac{\partial \mathbf{A}}{\partial \rho_i} \theta - \mathbf{A} \frac{\partial \theta}{\partial \rho_i} \right) \\ &+ \lambda_3^\top \left(\frac{\partial \mathbf{K}}{\partial \rho_i} \mathbf{v} + \mathbf{K} \frac{\partial \mathbf{v}}{\partial \rho_i} + \frac{\partial \mathbf{B}}{\partial \rho_i} \mathbf{p} + \mathbf{B} \frac{\partial \mathbf{p}}{\partial \rho_i} \right) \\ &+ \lambda_4^\top \left(\frac{\partial \mathbf{B}^\top}{\partial \rho_i} \mathbf{v} + \mathbf{B}^\top \frac{\partial \mathbf{v}}{\partial \rho_i} + \frac{\partial \mathbf{M}}{\partial \rho_i} \mathbf{p} + \mathbf{M} \frac{\partial \mathbf{p}}{\partial \rho_i} \right) \end{aligned} \tag{B.20}$$

Taking the coefficients of the DOF sensitivities:

$$\begin{aligned} \frac{\partial \theta}{\partial \rho_i} &\quad \rightarrow \quad \lambda_1^\top (\mathbf{K}_\mathrm{C} + \mathbf{K}_\mathrm{D}) - \lambda_2^\top \mathbf{A} = 0 \\ \frac{\partial \mathbf{u}}{\partial \rho_i} &\quad \rightarrow \quad \frac{\partial R}{\partial \mathbf{u}} + \lambda_2^\top \mathbf{K}_\mathrm{U} = 0 \\ \frac{\partial \mathbf{v}}{\partial \rho_i} &\quad \rightarrow \quad \lambda_3^\top \mathbf{K} + \lambda_4^\top \mathbf{B}^\top + \lambda_1^\top \frac{\partial \mathbf{K}_\mathrm{C}}{\partial \mathbf{v}} \theta = 0 \\ \frac{\partial \mathbf{p}}{\partial \rho_i} &\quad \rightarrow \quad \lambda_3^\top \mathbf{B} + \lambda_4^\top \mathbf{M} = 0 \end{aligned} \tag{B.21}$$

To calculate the adjoints the following system needs to be solved:

$$\begin{bmatrix} (\mathbf{K}_\mathrm{C} + \mathbf{K}_\mathrm{D})^\top & -\mathbf{A}^\top & 0 & 0 \\ 0 & \mathbf{K}_\mathrm{U}^\top & 0 & 0 \\ \left(\frac{\partial \mathbf{K}_\mathrm{C}}{\partial \mathbf{v}} \theta \right)^\top & 0 & \mathbf{K}^\top & \mathbf{B} \\ 0 & 0 & \mathbf{B}^\top & \mathbf{M}^\top \end{bmatrix} \begin{bmatrix} \lambda_1 \\ \lambda_2 \\ \lambda_3 \\ \lambda_4 \end{bmatrix} = \begin{bmatrix} 0 \\ -\frac{\partial R}{\partial \mathbf{u}} \\ 0 \\ 0 \end{bmatrix} \tag{B.22}$$

The final adjoint sensitivities are therefore:

$$\frac{\partial R^*}{\partial \rho_i} = \lambda_1^\top \frac{\partial \mathbf{K}_\mathrm{D}}{\partial \rho_i} \theta + \lambda_2^\top \left(\frac{\partial \mathbf{K}_\mathrm{U}}{\partial \rho_i} \mathbf{u} - \frac{\partial \mathbf{A}}{\partial \rho_i} \theta \right) + \lambda_3^\top \left(\frac{\partial \mathbf{K}}{\partial \rho_i} \mathbf{v} + \frac{\partial \mathbf{B}}{\partial \rho_i} \mathbf{p} \right) + \lambda_4^\top \left(\frac{\partial \mathbf{B}^\top}{\partial \rho_i} \mathbf{v} + \frac{\partial \mathbf{M}}{\partial \rho_i} \mathbf{p} \right) \tag{B.23}$$

B.4.1. Pseudo-code implementation of $\frac{\partial \mathbf{K}_C}{\partial \mathbf{v}}\theta$

The sensitivities of the convection matrix with respect to the velocities are not normally calculated as part of the *hybrida* environment, therefore a pseudo-code is presented in Algorithm 1.

Algorithm 1 Convection matrix sensitivities with respect to velocities

```
$E_{\text{conn}} \leftarrow$ import element connectivity                ▷ Set containing the nodes of each element
$N_{\text{conn}} \leftarrow$ invert mapping of $E_{\text{conn}}$        ▷ Set containing the element participation of each node
$\mathbf{f} \leftarrow$ empty $(n_\theta, n_v)$ matrix                  ▷ To be used as the $\frac{\partial \mathbf{K}_C}{\partial \mathbf{v}}\theta$ variable
for $i$ in range(0, number of nodes) do                                  ▷ Loop over nodes
    for $j$ in range(0,3) do                                             ▷ Loop over each velocity component
        if DOF $3 * i + j$ in $\Omega_{\text{TF}}$ then                  ▷ Ensure node is inside flow domain
            $\frac{\partial \mathbf{K}_C}{\partial v_i} \leftarrow$ empty $(n_\theta, n_\theta)$ sparse matrix    ▷ Define empty matrix
            if $j = 0$: $v =$ diagonal matrix $[1,0,0]$                  ▷ Sensitivities of $v_x$
            if $j = 1$: $v =$ diagonal matrix $[0,1,0]$                  ▷ Sensitivities of $v_y$
            if $j = 2$: $v =$ diagonal matrix $[0,0,1]$                  ▷ Sensitivities of $v_z$
            for $k$ in $N_{\text{conn}}[i]$ do                           ▷ Loop over each element in nodal connectivity matrix
                $I \leftarrow$ repeat $E_{\text{conn}}[k]$ each element for length$(E_{\text{conn}}[k])$    ▷ $I$ index of $\frac{\partial \mathbf{K}_C}{\partial \mathbf{v}}$ matrix
                $J \leftarrow$ repeat $E_{\text{conn}}[k]$ for length$(E_{\text{conn}}[k])$                 ▷ $J$ index of $\frac{\partial \mathbf{K}_C}{\partial \mathbf{v}}$ matrix
                $\frac{\partial \mathbf{K}_C}{\partial v_i}[I, J] \leftarrow$ retrieve element matrix $k$ for velocity vector $v$    ▷ Built element matrix $k$
                $\mathbf{f}[:, 3i + j] \leftarrow \frac{\partial \mathbf{K}_C}{\partial v_i} \cdot \theta$   ▷ Dot product
            end for
        end if
    end for
end for
```

B.5. Adjoint sensitivities mechanical compliance constraint

The mechanical compliance constraint is formulated to provide a minimum mechanical stiffness and is only calculated in the thermo-mechanical domain of the optimization. The mechanical compliance is calculated exclusively from the mechanically induced deformations:

$$c_u = \mathbf{u}_{\text{m}}^\top \mathbf{K}_{\text{U}} \mathbf{u}_{\text{m}} \tag{B.24}$$

where $\mathbf{u}_{\text{m}}$ are the mechanically induced deformations (without the thermo-mechanical contribution), calculated by $\mathbf{u}_{\text{m}} = \mathbf{K}_{\text{U}}^{-1}\mathbf{f}$. A mechanical compliance can be applied as follows:

$$g_2 = \frac{\mathbf{u}_{\text{m}}^\top \mathbf{K}_{\text{U}} \mathbf{u}_{\text{m}}}{c_{\text{u,max}}} - 1 \leq 0. \tag{B.25}$$

The sensitivities of the mechanical compliance constraint are calculated from the adjoint problem:

$$g_2^* = g_2 + \lambda^\top \left(\mathbf{K}_{\text{U}} \mathbf{u}_{\text{m}} - \mathbf{f}\right) \tag{B.26}$$

Differentiating the adjoint problem with respect to the design variables gives, knowing that $\mathbf{K}_{\text{U}}$ is symmetric and $\frac{\partial \mathbf{f}}{\partial \rho_i} = 0$:

$$\frac{\partial g_2^*}{\partial \rho_i} = \frac{1}{c_{\text{u,max}}} \left(2\mathbf{u}_{\text{m}}^\top \mathbf{K}_{\text{U}} \frac{\partial \mathbf{u}_{\text{m}}}{\partial \rho_i} + \mathbf{u}_{\text{m}}^\top \frac{\partial \mathbf{K}_{\text{U}}}{\partial \rho_i} \mathbf{u}_{\text{m}}\right) + \lambda^\top \left(\frac{\partial \mathbf{K}_{\text{U}}}{\partial \rho_i} \mathbf{u}_{\text{m}} + \mathbf{K}_{\text{U}} \frac{\partial \mathbf{u}_{\text{m}}}{\partial \rho_i}\right). \tag{B.27}$$

Grouping the $\frac{\partial \mathbf{u}_{\text{m}}}{\partial \rho_i}$ coefficients:

$$\frac{\partial \mathbf{u}_{\text{m}}}{\partial \rho_i} \quad \rightarrow \quad \frac{2}{c_{\text{u,max}}} \mathbf{u}_{\text{m}}^\top \mathbf{K}_{\text{U}} + \lambda^\top \mathbf{K}_{\text{U}} = 0 \tag{B.28}$$

where cancelling $\mathbf{K}_{\text{U}}$ on both sides and rearranging for λ gives:

$$\lambda = -\frac{2}{c_{\text{u,max}}} \mathbf{u}_{\text{m}} \tag{B.29}$$

substituting this into the adjoint problem gives:

$$\begin{aligned}\frac{\partial g_2^*}{\partial \rho_i} &= \frac{1}{c_{\text{u,max}}}\mathbf{u}_\text{m}^\top \frac{\partial \mathbf{K}_\text{U}}{\partial \rho_i}\mathbf{u}_\text{m} + \left(-\frac{2}{c_{\text{u,max}}}\mathbf{u}_\text{m}^\top\right)\frac{\partial \mathbf{K}_\text{U}}{\partial \rho_i}\mathbf{u}_\text{m} \\ &= -\frac{1}{c_{\text{u,max}}}\mathbf{u}_\text{m}^\top \frac{\partial \mathbf{K}_\text{U}}{\partial \rho_i}\mathbf{u}_\text{m}\end{aligned} \tag{B.30}$$

B.6. Adjoint sensitivities thermal compliance constraint

The thermal compliance constraint is formulated to provide a minimum thermal resistance and is only calculated in the thermo-mechanical domain of the optimization. The thermal compliance is given as follows:

$$c_t = \theta^\top \mathbf{K}_\text{D}\theta. \tag{B.31}$$

This can be incorporated as minimum constraint as:

$$g_3 = \frac{\theta^\top \mathbf{K}_\text{D}\theta}{c_{\text{t,max}}} - 1 \leq 0. \tag{B.32}$$

The sensitivities of the mechanical compliance constraint are calculated from the adjoint problem:

$$g_3^* = g_3 + \lambda^\top\left(\mathbf{K}_\text{D}\theta - \mathbf{q}\right) \tag{B.33}$$

Differentiating the adjoint problem with respect to the design variables knowing that $\mathbf{K}_\text{D}$ is symmetric and $\frac{\partial \mathbf{q}}{\partial \rho_i} = 0$:

$$\frac{\partial g_3^*}{\partial \rho_i} = \frac{1}{c_{\text{t,max}}}\left(2\theta\mathbf{K}_\text{D}\frac{\partial \theta}{\partial \rho_i} + \theta^\top\frac{\partial \mathbf{K}_\text{D}}{\partial \rho_i}\theta\right) + \lambda^\top\left(\frac{\partial \mathbf{K}_\text{D}}{\partial \rho_i}\theta + \mathbf{K}_\text{D}\frac{\partial \theta}{\partial \rho_i}\right). \tag{B.34}$$

Grouping the $\frac{\partial \theta}{\partial \rho_i}$ coefficients:

$$\frac{\partial \theta}{\partial \rho_i} \quad \rightarrow \quad \frac{2}{c_{\text{t,max}}}\theta^\top\mathbf{K}_\text{D} + \lambda^\top\mathbf{K}_\text{D} = 0 \tag{B.35}$$

where cancelling $\mathbf{K}_\text{D}$ on both sides and rearranging for λ gives:

$$\lambda = -\frac{2}{c_{\text{t,max}}}\theta \tag{B.36}$$

substituting this into the adjoint problem gives:

$$\begin{aligned}\frac{\partial g_3^*}{\partial \rho_i} &= \frac{1}{c_{\text{t,max}}}\theta^\top\frac{\partial \mathbf{K}_\text{D}}{\partial \rho_i}\theta + \left(-\frac{2}{c_{\text{t,max}}}\theta^\top\right)\frac{\partial \mathbf{K}_\text{D}}{\partial \rho_i}\theta \\ &= -\frac{1}{c_{\text{t,max}}}\theta^\top\frac{\partial \mathbf{K}_\text{D}}{\partial \rho_i}\theta\end{aligned} \tag{B.37}$$

B.7. Sensitivities pressure drop constraint

This derivation is based on the work of Borrvall and Petersson [2003] and Wiker et al. [2007], where their objective function has been reformulated as a constraint. The objective formulation aims to minimise the power dissipation of the fluid flow, which later in the reference is shown to be equivalent to minimising the pressure drop between the inlet and outlet. Due to a special condition given in the reference of prescribing the velocities at the inlet and that $\mathbf{f}_v = 0$ on Γ_inlet and Γ_outlet, the complexity of the derivation is significantly reduced. The pressure drop constraint is:

$$g_4 = \frac{\mathbf{v}^\top\mathbf{K}_\text{DaS}\mathbf{v}}{c_{\text{f,max}}} - 1 \leq 0 \tag{B.38}$$

where $c_{\text{f,max}}$ is the maximum permissible dissipation energy. The sensitivities of the constraints are taken as follows:

$$\frac{\partial g_4}{\partial \rho_i} = \frac{1}{c_{\text{f,max}}}\mathbf{v}^\top\frac{\partial \mathbf{K}_\text{Da}}{\partial \rho_i}\mathbf{v} \tag{B.39}$$

where the sensitivities are taken of $\mathbf{K}_\text{Da}$, the Darcy matrix.

C

Model and optimization details

This appendix details all the parameters and values used in the thesis which may or may not have already been mentioned. The use of an unstructured mesh is partly due to the limitations in the software package GMSH [Geuzaine and Remacle, 2009] on surfaces with a larger number of edges which Ω_{opt} has.

C.1. Thermo-mechanical based optimization

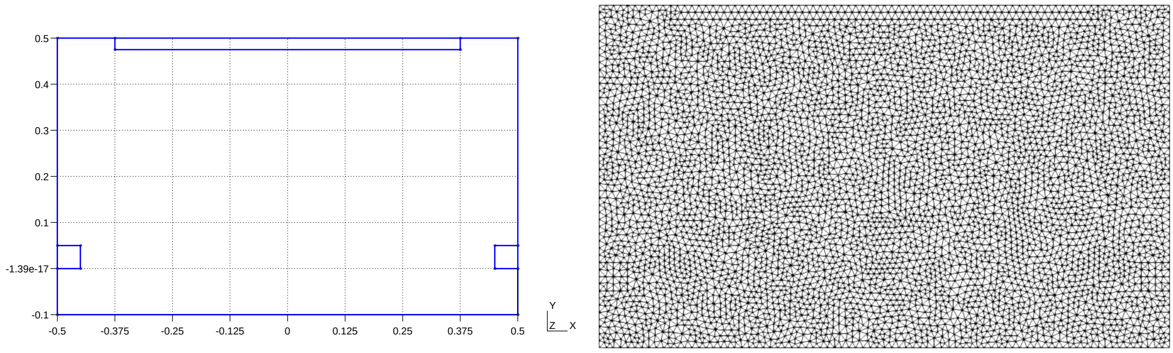

(a) Thermo-mechanical domain dimensions.

(b) Thermo-mechanical mesh.

Figure C.1: Thermo-mechanical domain.

C.1.1. Mesh characteristics

The mesh used in this model is a 2D unstructured mesh. A symmetrical approach (with a symmetry axis along $x = 0$) was not used as the intention was to use a similar mesh to that of the "asymmetric" model in Chapter 4. The number of nodes is 81 therefore the element size is $h_e = 1/(81-1)$m.

C.1.2. Material properties

Mechanical parameters

Young's Modulus	1.0 Pa
Poisson	0.33
Density	1.0 kg/m^3
Thermal-expansion coefficient	1.0 K^{-1}

Thermal parameters

Thermal conductivity	1.0 W/(mK)
Density	1.0 kg/m^3
Specific heat	1.0 J/kg · K

C.1.3. Model parameters

f_y	1×10^{-3} N
q_{in}	1×10^{-2} W

C.1.4. Optimization parameters

RAMP penalisation	3.0
Move-limiter	0.1
Minimum density ρ_{min}	0.001
Initial density ρ_0	0.5
Maximum number of iterations	550

C.2. Thermo-mechanical and convection based optimization

C.2.1. "Symmetric" model

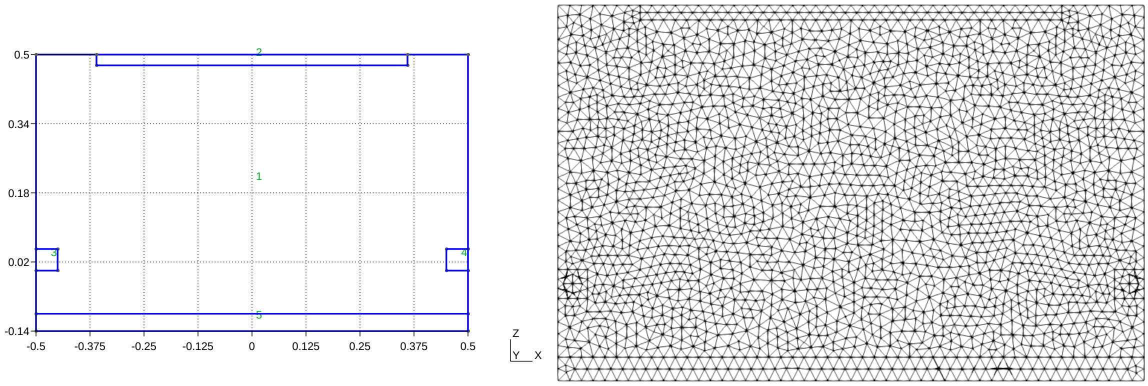

(a) Thermo-mechanical and convective domain dimensions.

(b) Thermo-mechanical and convective mesh of symmetric model.

Figure C.2: Thermo-mechanical and convective domain.

C.2.2. Mesh characteristics

The mesh used in this model is a 3D unstructured mesh. The number of nodes is 51 therefore the element size is $h_e = 1/(51-1)$ m.

C.2.3. Material properties

Mechanical parameters

Young's Modulus	1.0 Pa
Poisson	0.33
Density	1.0 kg/m^3
Thermal-expansion coefficient	1.0 K^{-1}

Thermal parameters

Solid conductivity	1 W/(mK)
Fluid conductivity	$\frac{h_e}{2/\mathrm{Pe}}$ W/(mK)
Density	1.0 kg/m^3
Specific heat	1.0 J/kg$\cdot$K

Fluid parameters

Kinematic viscosity	1.0 m^2/(mK)
Density	1.0 kg/m^3

C.2.4. Model parameters

f_y	$h_e \times 1 \times 10^{-3}$ N
q_{in}	$h_e \times 1 \times 10^{-2}$ W
v_{in}	1×10^{5} ms^{-1}
$c_{\text{u,max}}$	1.75×10^{-8} Nm
$c_{\text{t,max}}$	7.5×10^{-3} WK/m
$c_{\text{SD,max}}$	1.0×10^{-11} m^2

C.2.5. Optimization parameters

RAMP penalisation	3.0
Move-limiter	0.1
Minimum density ρ_{min}	0.001
Initial density ρ_0	0.5
Maximum number of iterations	350

C.2.6. "Asymmetric" model

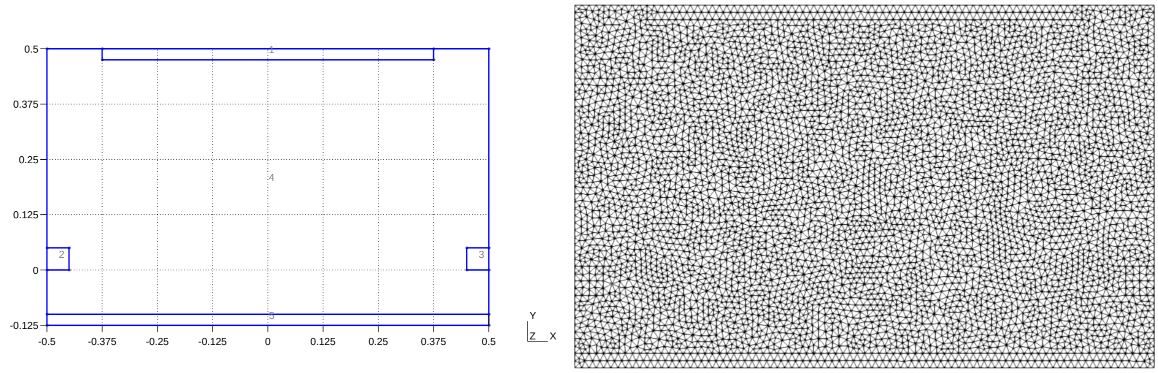

(a) Thermo-mechanical and convective domain dimensions.

(b) Thermo-mechanical and convective mesh of asymmetric model.

Figure C.3: Thermo-mechanical and convective domain.

C.2.7. Mesh characteristics

The mesh used in this model is a 2D unstructured mesh. The number of nodes is 81 therefore the element size is $h_e = 1/(81-1)$ m.

C.2.8. Material properties

Mechanical parameters

Young's Modulus	1.0 Pa
Poisson	0.33
Density	1.0 $\mathrm{kg/m^3}$
Thermal-expansion coefficient	1.0 $\mathrm{K^{-1}}$

Thermal parameters

Solid conductivity	1 W/(mK)
Fluid conductivity	$\frac{h_e}{2/\mathrm{Pe}}$ W/(mK)
Density	1.0 $\mathrm{kg/m^3}$
Specific heat	1.0 J/kg·K

Fluid parameters

Kinematic viscosity	1.0 $\mathrm{m^2/(mK)}$
Density	1.0 $\mathrm{kg/m^3}$

C.2.9. Model parameters

f_y	1×10^{-4} N
q_{in}	1×10^{0} W
v_{in}	$1 \times 10^{5}\,\mathrm{ms^{-1}}$
$c_{\mathrm{u,max}}$	1.9×10^{-9} Nm
$c_{\mathrm{t,max}}$	1.2×10^{-3} WK/m
$c_{\mathrm{SD,max}}$	$1.0 \times 10^{-9}\,\mathrm{m^2}$

C.2.10. Optimization parameters

RAMP penalisation	3.0
Move-limiter	0.1
Minimum density ρ_{min}	0.001
Initial density ρ_0	0.5
Maximum number of iterations	550

C.3. Thermo-mechanical, convection and flow based optimization

C.3.1. Mesh characteristics

The mesh used in this model is a 3D unstructured mesh. The number of nodes is 21 therefore the element size is $h_e = 1/(21-1)$ m.

C.3.2. Material properties

Mechanical parameters

Young's Modulus	1.0 Pa
Poisson	0.33
Density	1.0 $\mathrm{kg/m^3}$
Thermal-expansion coefficient	1.0 $\mathrm{K^{-1}}$

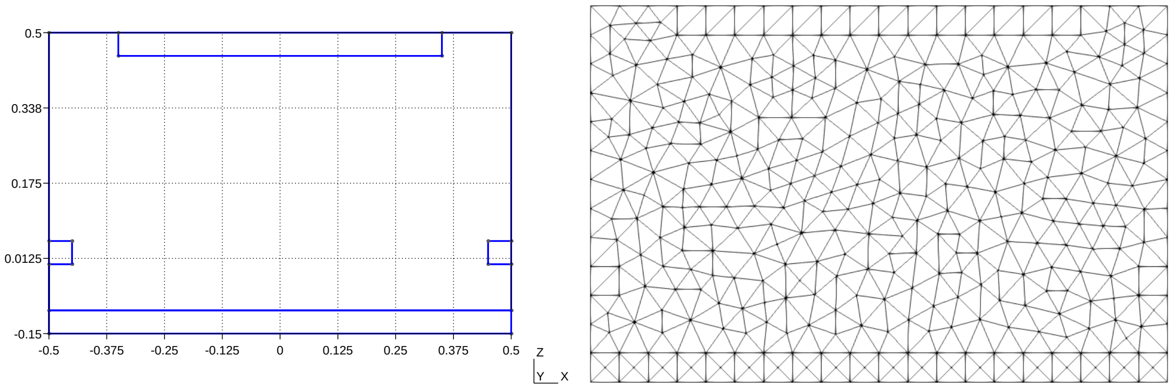
0.5
0.338
0.175
0.0125
-0.15
-0.5
-0.375
-0.25
-0.125
0
0.125
0.25
0.375
0.5
Z
Y
X

(a) Thermo-mechanical, convection and flow domain dimensions of thermo-mechanical plane.

(b) Thermo-mechanical, convective and flow mesh of thermo-mechanical plane.

Figure C.4: Thermo-mechanical plane.

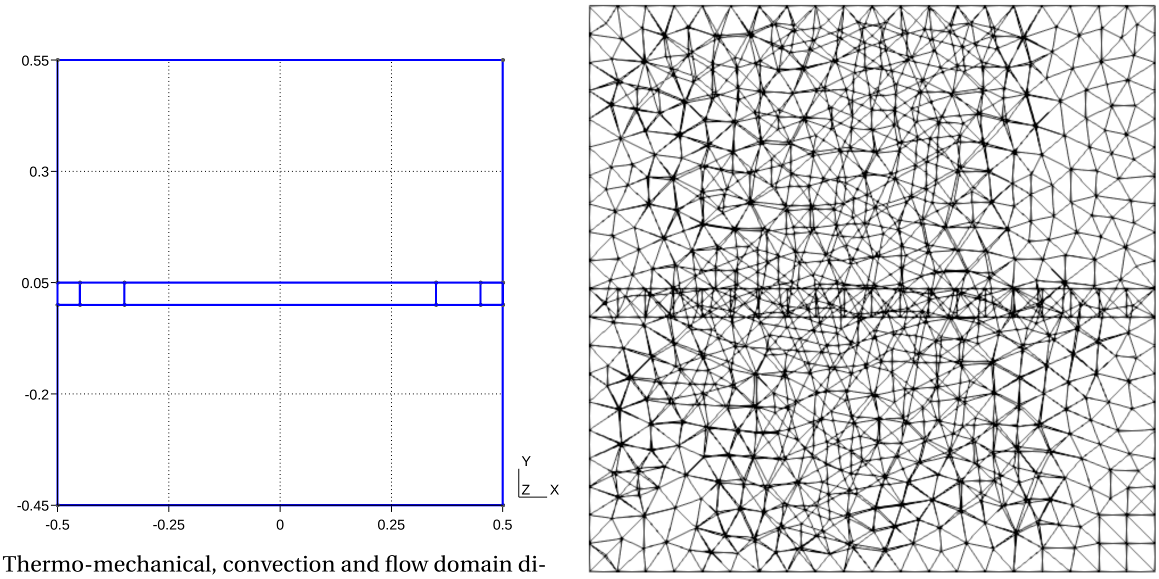
0.55
0.3
0.05
-0.2
-0.45
-0.5
-0.25
0
0.25
0.5
Y
Z
X

(a) Thermo-mechanical, convection and flow domain dimensions of thermo-fluid plane.

(b) Thermo-mechanical, convective and flow mesh of thermo-fluid plane.

Figure C.5: Thermo-fluid plane.

Thermal parameters

Solid conductivity	1 W/(mK)
Fluid conductivity	$\frac{h_e}{2/\mathrm{Pe}}$ W/(mK)
Density	1.0 kg/m^3
Specific heat	1.0 J/kg·K

Fluid parameters

Kinematic viscosity	1.0 m^2/(mK)
Density	1.0 kg/m^3

C.3.3. Model parameters

f_y	1×10^{-4} N
q_{in}	1×10^{0} W
Pe	2250
v_{in}	1×10^{1} ms^{-1}
$c_{\text{u,max}}$	1.406×10^{-7} Nm
$c_{\text{t,max}}$	1.434×10^{-5} WK/m
$c_{\text{f,max}}$	215 Pa
$c_{\text{SD,max}}$	1.0×10^{-9} m^2

C.3.4. Optimization parameters

RAMP penalisation	3.0
Move-limiter	0.1
Minimum density ρ_{min}	0.001
Initial density ρ_0	0.5
Maximum number of iterations	300

D

Extra density distributions and convergence plots

D.1. Density distributions

Some density distributions did not quite converge very discretely due to an overly stringent surface deformation constraint. The examples given here did not manage to converge in the allotted iteration limit, although many if not all of the unconverged designs can bee seen to still be varying in objective value.

Localised $c_{\mathrm{SD,max}} = 10^{-11}\,\mathrm{m}^2$

Table D.1: Comparison of density distributions for varying thermal and mechanical compliance constraints all subject to the same surface deformation constraint. Black regions represent material whereas white areas are voids. The graphs contain the following data: OBJ: Volume minimisation objective function, SD: MSE of surface deformations, MC: Mechanical compliance constraint, TC: Thermal compliance constraint, M_{ND}: Measure of non-discreteness of final iteration.

		Thermal compliance (TC)		
		$c_{\mathrm{t,max}} = 0.75 \times 10^{-4}$	$c_{\mathrm{t,max}} = 1.50 \times 10^{-4}$	$c_{\mathrm{t,max}} = 2.25 \times 10^{-4}$
Mechanical Compliance (MC)	$c_{\mathrm{u,max}} = 0.85 \times 10^{-6}$	$M_{\mathrm{ND}} = 0.08$ 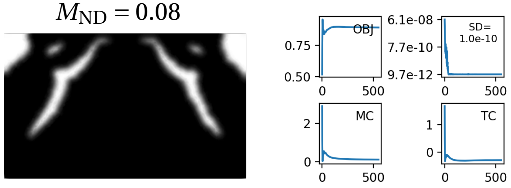	$M_{\mathrm{ND}} = 0.08$ 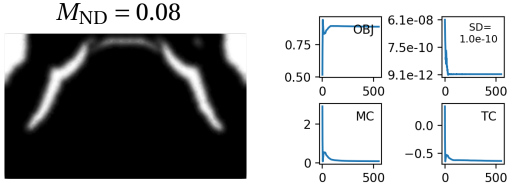	$M_{\mathrm{ND}} = 0.08$ 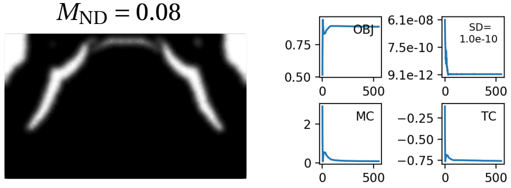
	$c_{\mathrm{u,max}} = 1.50 \times 10^{-6}$	$M_{\mathrm{ND}} = 0.15$ 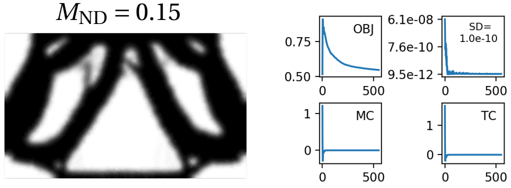	$M_{\mathrm{ND}} = 0.17$ 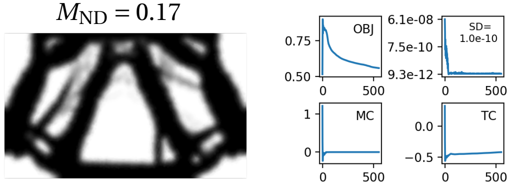	$M_{\mathrm{ND}} = 0.17$ 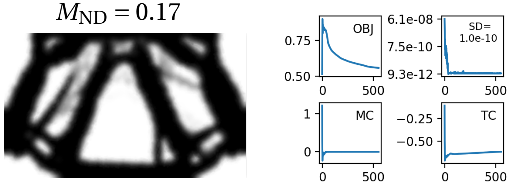
	$c_{\mathrm{u,max}} = 3.30 \times 10^{-6}$	$M_{\mathrm{ND}} = 0.15$ 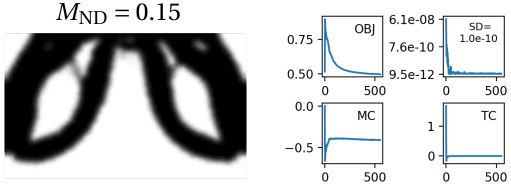	$M_{\mathrm{ND}} = 0.12$ 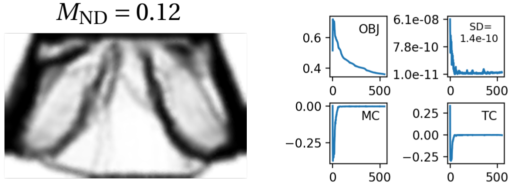	$M_{\mathrm{ND}} = 0.23$ 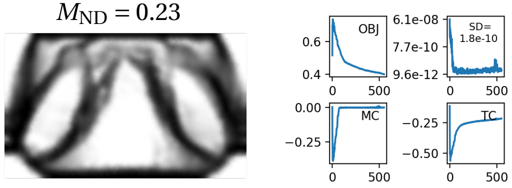

Delocalised $c_{\mathrm{SD,max}} = 10^{-11}\,\mathrm{m}^2$

Table D.2: Comparison of density distributions for varying thermal and mechanical compliance constraints all subject to the same surface deformation constraint. Black regions represent material whereas white areas are voids. The graphs contain the following data: OBJ: Volume minimisation objective function, SD: Surface deformation constraint, MC: Mechanical compliance constraint, TC: Thermal compliance constraint, M_{ND}: Measure of non-discreteness of final iteration.

		Thermal compliance (TC)		
		$c_{\mathrm{t,max}} = 0.75 \times 10^{-4}$	$c_{\mathrm{t,max}} = 1.00 \times 10^{-4}$	$c_{\mathrm{t,max}} = 1.50 \times 10^{-4}$
Mechanical Compliance (MC)	$c_{\mathrm{u,max}} = 1.25 \times 10^{-6}$	$M_{\mathrm{ND}} = 0.14$ 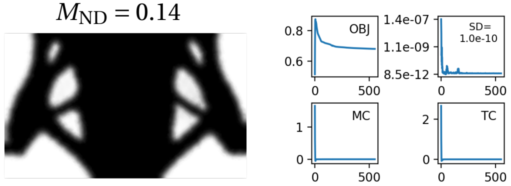	$M_{\mathrm{ND}} = 0.21$ 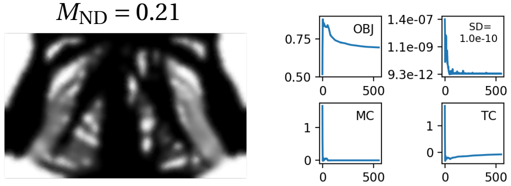	$M_{\mathrm{ND}} = 0.24$ 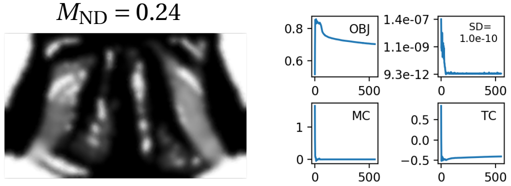
	$c_{\mathrm{u,max}} = 2.25 \times 10^{-6}$	$M_{\mathrm{ND}} = 0.14$ 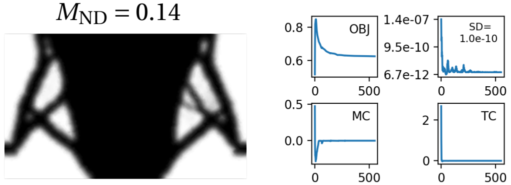	$M_{\mathrm{ND}} = 0.21$ 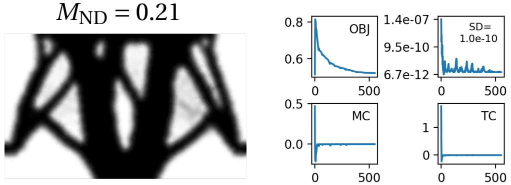	$M_{\mathrm{ND}} = 0.25$ 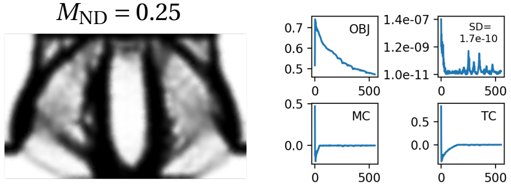
	$c_{\mathrm{u,max}} = 3.30 \times 10^{-6}$	$M_{\mathrm{ND}} = 0.14$ 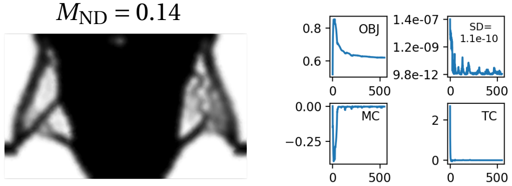	$M_{\mathrm{ND}} = 0.17$ 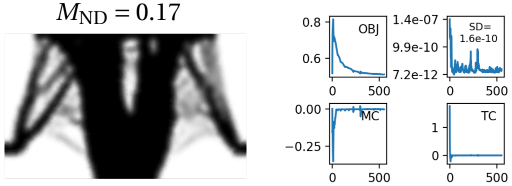	$M_{\mathrm{ND}} = 0.30$ 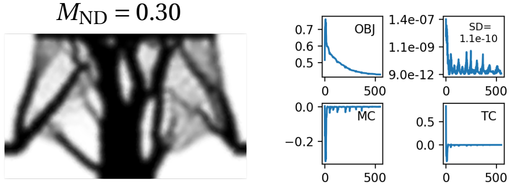

Asymmetric model $c_{\mathrm{SD,max}} = 10^{-11}\,\mathrm{m}^2$. More symmetry seen when the surface deformation constraint is reduced further.

Table D.3: Results of the "asymmetric" model, subject to varying Péclet numbers. The first row represents the density distributions of the final optimization iteration, where the fluid channel runs along the bottom of the thermo-mechanical structure. The second row shows the deformed and undeformed states of the thermo-mechanical structure. The third row shows the surface deformations of the mirror. The fourth row shows the temperature field throughout the thermo-mechanical structure. The fifth row shows the temperature gradients, where the high gradients are seen to be found at the interface between the structure and flow channel. The fifth row is the temperature along the channel Ω_{chan} it has been scaled vertically to better depict the temperature field. The final row is a graph of the bulk temperatures at the outlet of the channel as a function of the Péclet number.

Péclet	3.0	3.5	4.0	5.0	7.0
Density distribution $\rho_i = 0$ 1	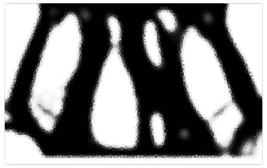	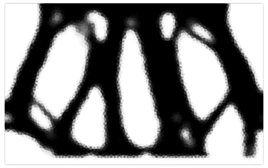	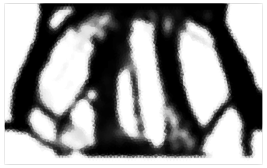	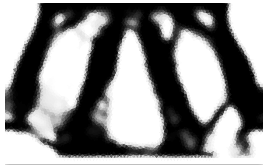	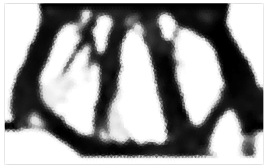
Deformed state ▨ Undeformed ■ Deformed	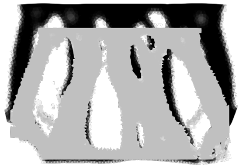	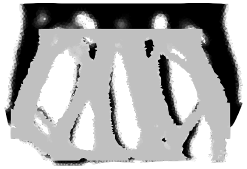	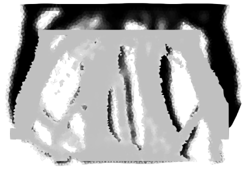	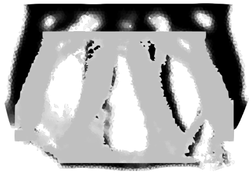	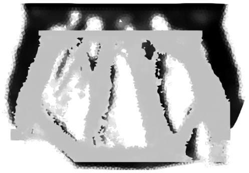
Surface deformation (m)	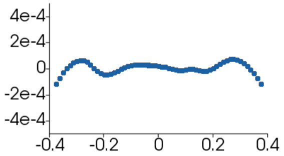	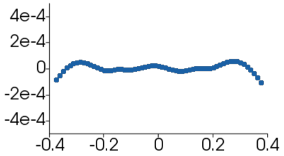	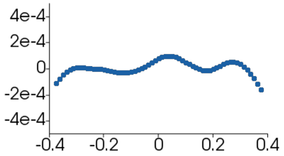	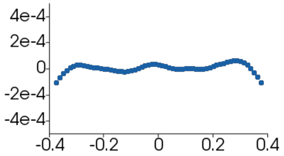	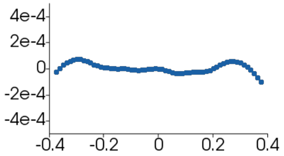
Temperature field (K) $\theta = 0$ 0.01	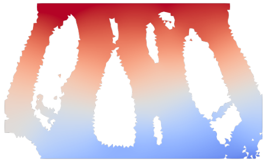	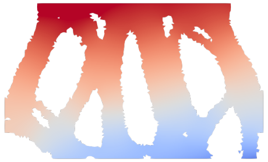	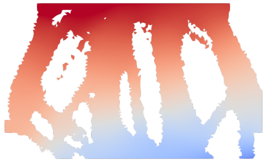	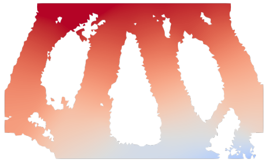	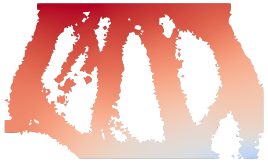
Magnitude of temperature gradient (K/m) $\nabla\theta = 0$ 0.03	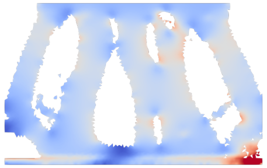	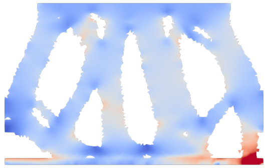	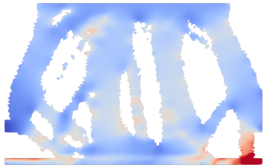	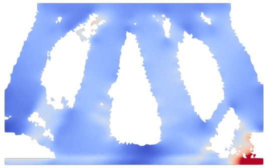	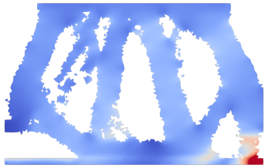
Channel temperature (K) $\theta = 0$ 0.005	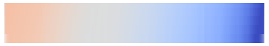	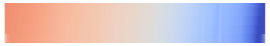	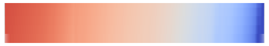	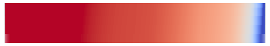	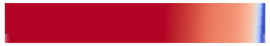

D.2. Convergence plots

As it was not seen to enhance the story line, the convergence plots are given in this appendix as a source of reference to show that convergence has taken place.

D.2.1. Convergence of 3D symmetric models

$c_{\text{SD,max}} = 1 \times 10^{-8}$, $\text{Pe} = 1.0$:

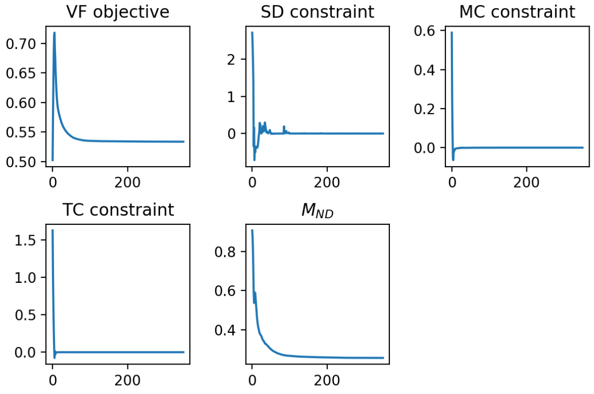

$c_{\text{SD,max}} = 1 \times 10^{-8}$, $\text{Pe} = 1.5$:

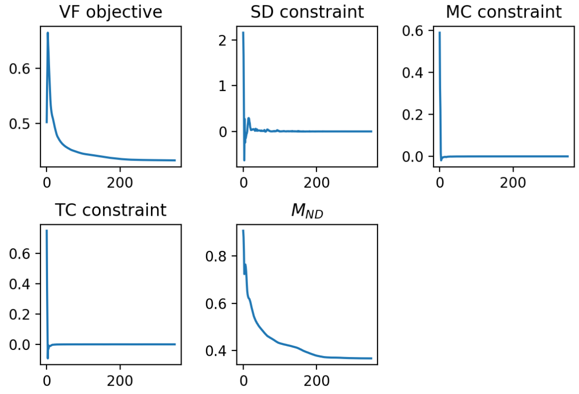

$c_{\text{SD,max}} = 1 \times 10^{-8}$, $\text{Pe} = 2.0$:

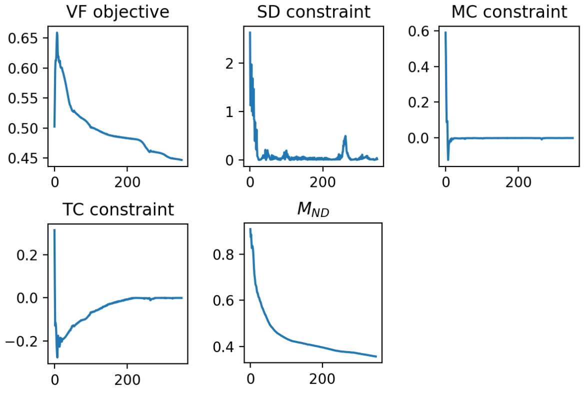

$c_{\mathrm{SD,max}} = 1 \times 10^{-8}$, $\mathrm{Pe} = 3.0$:

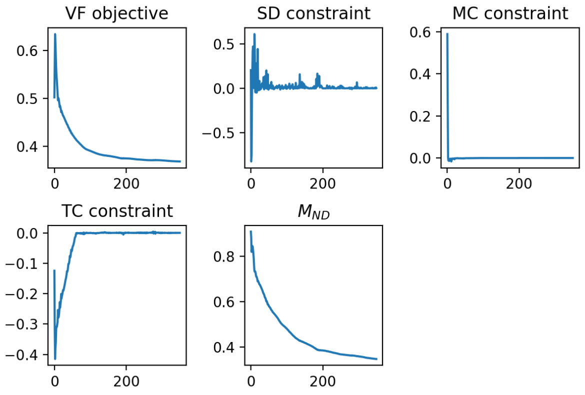

$c_{\mathrm{SD,max}} = 1 \times 10^{-8}$, $\mathrm{Pe} = 5.0$:

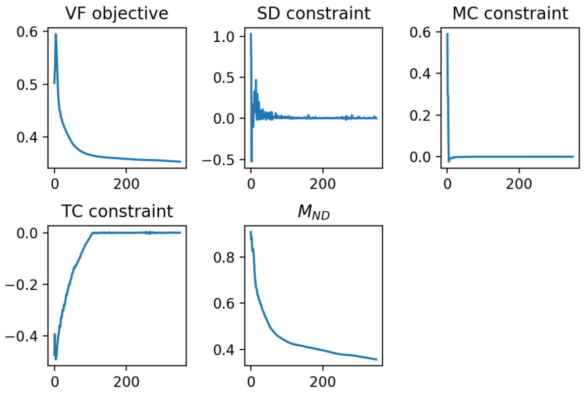

D.2.2. Convergence of 2D asymmetric models

$c_{\mathrm{SD,max}} = 1 \times 10^{-10}$, $\mathrm{Pe} = 2.5$:

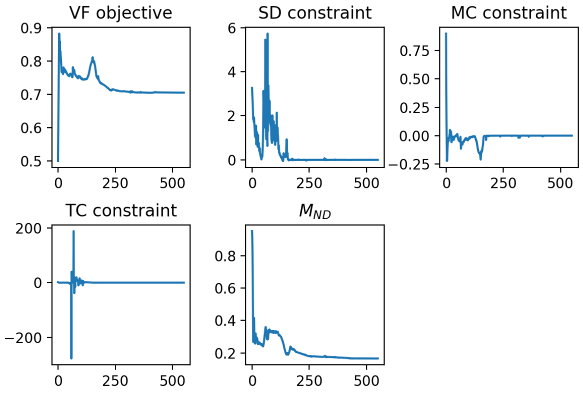

$c_{\mathrm{SD,max}} = 1 \times 10^{-10}$, $\mathrm{Pe} = 3.0$:

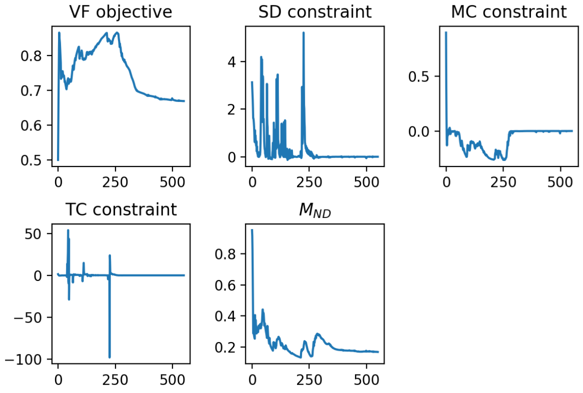

$c_{\mathrm{SD,max}} = 1 \times 10^{-10}$, $\mathrm{Pe} = 3.5$:

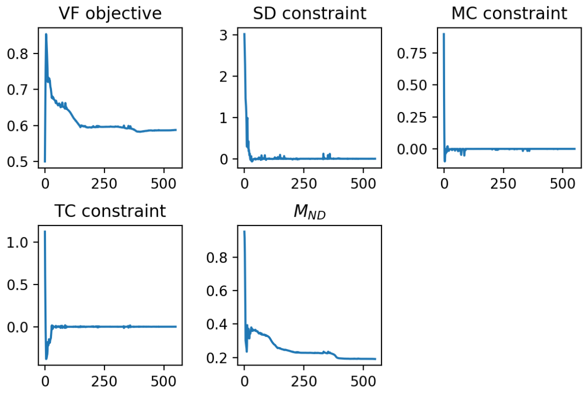

$c_{\mathrm{SD,max}} = 1 \times 10^{-10}$, $\mathrm{Pe} = 4.0$:

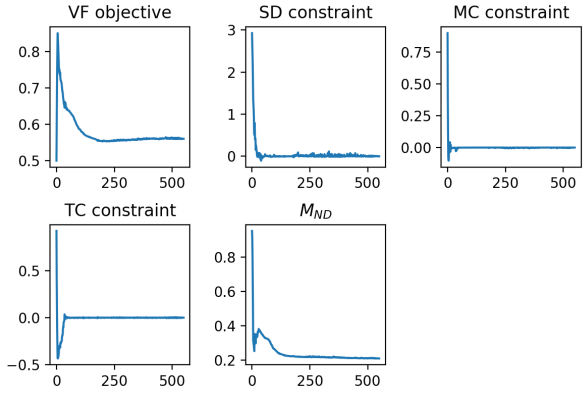

$c_{\mathrm{SD,max}} = 1 \times 10^{-10}$, $\mathrm{Pe} = 5.0$:

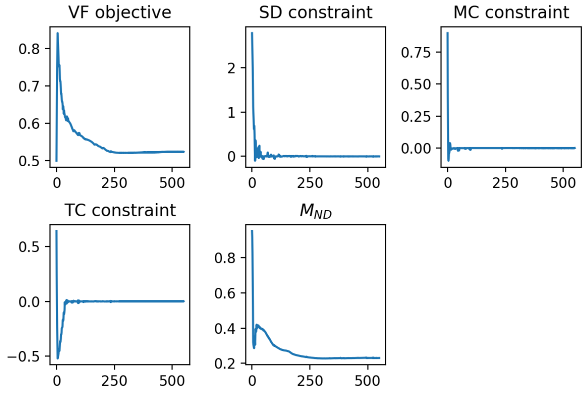

D.2.3. Convergence of 3D thermo-mechanical and thermo-fluid

$c_{\mathrm{SD,max}} = 1 \times 10^{-9}$, Model 1:

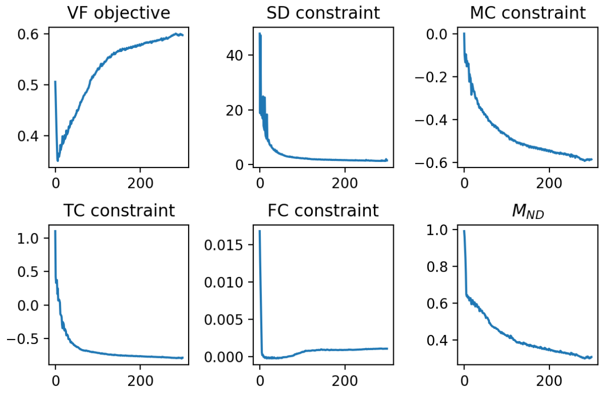

$c_{\mathrm{SD,max}} = 1 \times 10^{-9}$, Model 2:

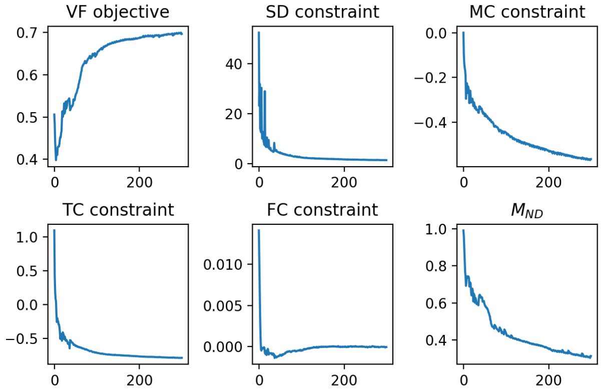

$c_{\mathrm{SD,max}} = 1 \times 10^{-9}$, Model 3:

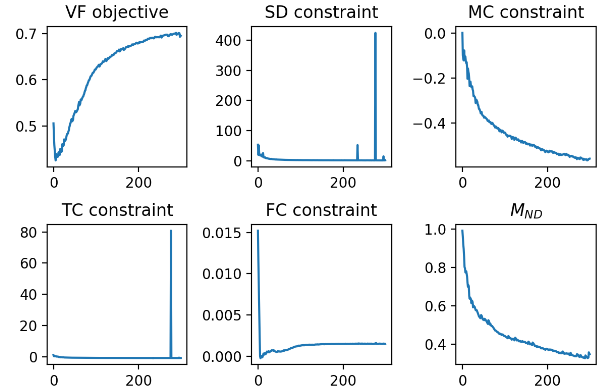

E

Finite differences

In this appendix, the adjoints of Chapters 3-5 of the surface deformation constraint will be validated by means of central finite differences. The method involves retaining the error between the sensitivities of the constraint and the finite difference for different step sizes of the finite difference. The error is given by:

$$\epsilon = \frac{\frac{g(\rho_1)-g(\rho_{-1})}{2h} - \left.\frac{\partial g_i}{\partial \rho}\right|_{\rho=\rho_0}}{\frac{g(\rho_1)-g(\rho_{-1})}{2h}} \tag{E.1}$$

where the first term is the constraint sensitivities of element i and the second term the constraint finite differences with a step size h. The upper and lower finite difference values for the central finite difference scheme are taken as follows:

$$\begin{aligned} \rho_{1i} &= (1+h)\rho_{0i} \\ \rho_{-1i} &= (1-h)\rho_{0i}. \end{aligned} \tag{E.2}$$

Two sources of error are present in such an analysis:

- **Rounding error:** is due to computers not being able to represent all real numbers. Therefore a rounding error arises when the step size is small. This is represented by a "noisy" -1 slope on a log-log plot of the absolute error versus the step size.
- **Approximation error:** is due to the step size becoming too large. This brings upon an increasing error in the calculation of the sensitivities. Represented in a log-log plot of the absolute error versus the step size by a +1 slope.

Step size $h = h^*$ is where the error is at its minimum. This is roughly the square root of the computer precision $h^* \approx \sqrt{\text{eps}}$.

In Chapter 3 two models are used based on the same 2D framework, the difference is the locations of the boundary conditions. Chapter 4 used two models based on a 2D ("asymmetric" model) and a 3D ("symmetric" model) framework. Chapter 5 uses the same 3D framework for all three models. Four finite differences will be performed, one for each framework.

In Figure E.1 the finite differences for the aforementioned models are shown. As expected, the rounding error is clearly seen in all models by the -1 slope. The lengths of the approximation error are however stunted due to the flat region which becomes somewhat larger with rising model complexity.

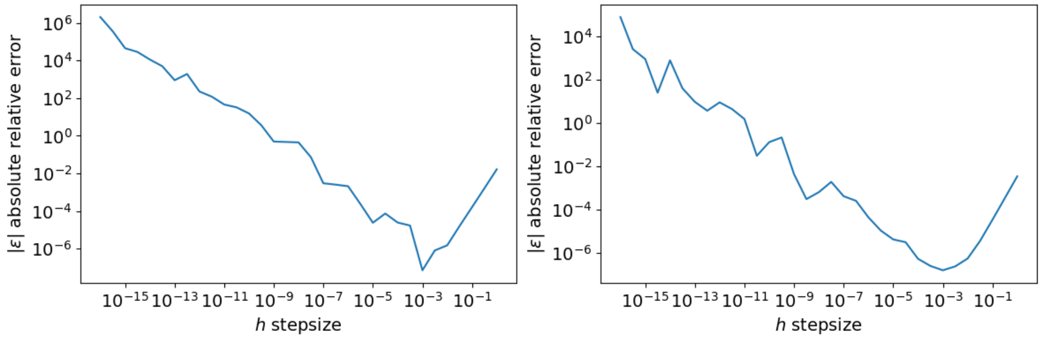

(a) Thermo-mechanical finite differences.

(b) Thermo-mechanical and convective finite differences of asymmetric model.

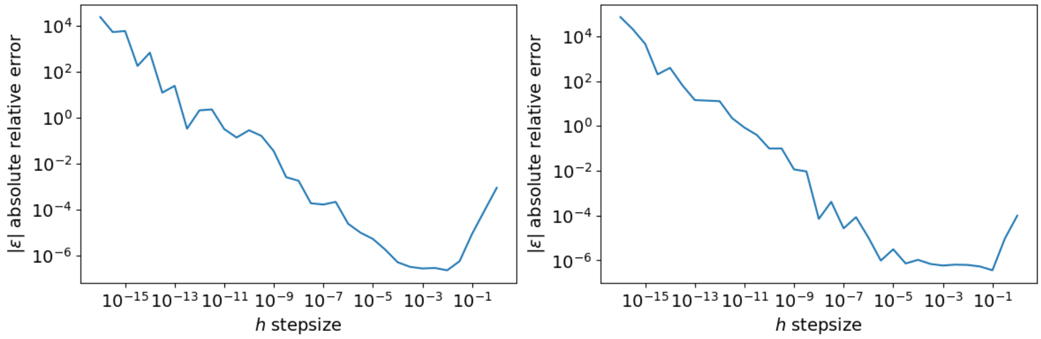

(c) Thermo-mechanical and convective finite differences of symmetric model.

(d) Thermo-mechanical, convective and flow finite differences.

Figure E.1: Absolute errors between the analytical and finite differences sensitivities of the different model frameworks.

F

Modal decomposition of advection-diffusion equation

The eigenvalue problem being solved is as follows:

$$(\{\mathbf{K}_\mathrm{D} + \mathbf{K}_\mathrm{C}\} - \lambda \mathbf{C}_\theta)\, \boldsymbol{\phi} e^{-\lambda t} = \mathbf{0} \tag{F.1}$$

where $\boldsymbol{\phi}$ are the eigenvectors, λ the values and t time. The capacitance, convective and conductive matrices are given as follows:

$$\begin{aligned} \left[C_\theta^\mathrm{e}\right] &= \rho \int_\Omega c[N][N]^\top \mathrm{d}V \\ \left[K_\mathrm{C}^\mathrm{e}\right] &= \rho \int_\Omega c[N][v]^\top [B] \mathrm{d}V \\ \left[K_\mathrm{D}^\mathrm{e}\right] &= \int_\Omega [B]^\top [D][B] \mathrm{d}V \end{aligned} \tag{F.2}$$

where the linear shape functions used are $[N] = [1-\eta, \eta]$ and $[B] = \frac{1}{h_\mathrm{e}}[-1, 1]$. Building up the element matrices using the aforementioned shape functions provides two symmetric contributions, $[C_\theta^\mathrm{e}]$ and $[K_\mathrm{D}^\mathrm{e}]$ and an asymmetric contribution brought upon by the velocity term $[K_\mathrm{C}^\mathrm{e}]$.

There are as many eigenvalues as there are nodes in the system if you include the trivial solution $\lambda = 0$. By sorting the eigenvalues and eigenvectors in order of increasing absolute eigenvalue we can extract the lowest modes.

No complex eigenvalues were found in the system also meaning that there aren't any complex eigenmodes. A complex eigenmode would signify that there is an energy flux in the system, in dynamics this could be coupled to a damping, in temperature control this would be a heat flux in the system. However, little to no proof has been found with respect to complex eigenvalues or time constants in literature.

F.1. 1D Model

The 1D model consists of uniform heat load q along its length where the fluxes at either end of the unit length domain are $\frac{\partial \theta}{\partial x}[x = 0] = 0\,\mathrm{K}$ and $\frac{\partial \theta}{\partial x}[x = 1] = 0\,\mathrm{K}$.

Plotting the results of the discrete modal analysis against a variation in velocity clearly shows the phase shift and in fact includes an increase in amplitude seen in Figure F.1.

F.2. 2D Model

The 2D model consists of a uniform heat load q across the entire surface area of the domain. A fluid flow runs along the top border of the domain from left to right, with a temperature at the inlet of $\theta_\mathrm{in} = 0\,\mathrm{K}$. The modes are shown in Figure F.2.

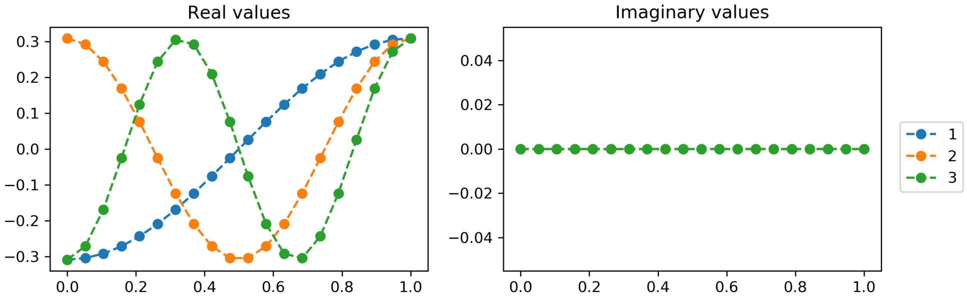

(a) $v = 0$

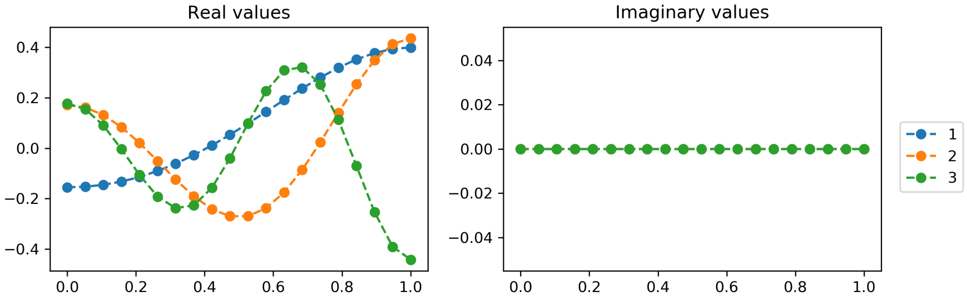

(b) $v = 2$

Figure F.1: Modal amplitudes [K] plotted against domain length [m] to show the effect of velocity on 1D model of modes 1-3 of the advection-diffusion problem.

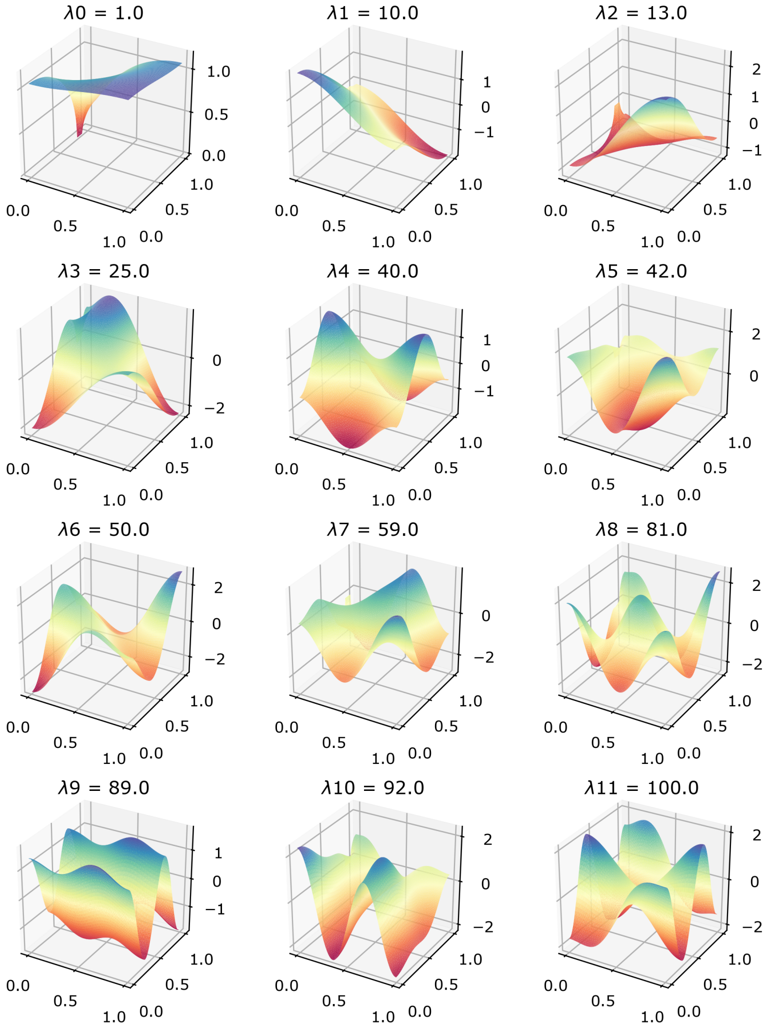

Figure F.2: Modal amplitudes [K] of the advection-diffusion equation on square domain.

Bibliography

Niels Aage, Erik Andreassen, Boyan Stefanov Lazarov, and Ole Sigmund. Giga-voxel computational morphogenesis for structural design. *Nature Publishing Group*, 550(7674):84–86, October 2017.

Joe Alexandersen. *Efficient topology optimisation of multiscale and multiphysics problems.* PhD thesis, Technical University of Denmark, November 2016.

Reza Behrou and James K Guest. Topology optimization for transient response of structures subjected to dynamic loads. In *18th AIAA/ISSMO Multidisciplinary Analysis and Optimization Conference*, 2017.

Martin Philip Bendsoe and Ole Sigmund. *Topology Optimization.* Theory, Methods, and Applications. Springer Science & Business Media, April 2003.

Thomas Borrvall and Joakim Petersson. Topology optimization of fluids in Stokes flow. *International Journal for Numerical Methods in Fluids*, 41(1):77–107, 2003.

Tyler E Bruns. A reevaluation of the SIMP method with filtering and an alternative formulation for solid–void topology optimization. *Structural and Multidisciplinary Optimization*, 30(6):428–436, August 2005.

Tyler E Bruns and Daniel A Tortorelli. Topology optimization of non-linear elastic structures and compliant mechanisms. *Computer Methods in Applied Mechanics and Engineering*, 190(26-27):3443–3459, 2001.

Talib Dbouk. A review about the engineering design of optimal heat transfer systems using topology optimization. *Applied Thermal Engineering*, 112:841–854, February 2017.

Joshua D Deaton and Ramana V Grandhi. Stiffening of restrained thermal structures via topology optimization. *Structural and Multidisciplinary Optimization*, 48(4):731–745, April 2013.

Ercan M Dede. Multiphysics Topology Optimization of Heat Transfer and Fluid Flow Systems. In *COMSOL Conference Boston*, pages 1–7, September 2009.

N P van Dijk, Kurt Maute, Matthijs Langelaar, and Fred van Keulen. Level-set methods for structural topology optimization: a review. *Structural and Multidisciplinary Optimization*, 48(3):437–472, March 2013.

Jean Donea and Antonio Huerta. Viscous Incompressible Flows. In *Finite Element Methods for Flow Problems*, pages 265–322. Wiley-Blackwell, Chichester, UK, 2005.

Johann Dugge. Thermal Modes for the Optimisation of Transient Thermo-Mechanics. Master's thesis, TU Delft, November 2012.

John A Dye, Peter E Weber, and United Technologies Corp. High performance cooled laser mirror. US Patent Office, February 1982.

Tong Gao and Weihong Zhang. Topology optimization involving thermo-elastic stress loads. *Structural and Multidisciplinary Optimization*, 42(5):725–738, June 2010.

Victor L Genberg. Optical Surface Evaluation. In *Structural Mechanics of Optical Systems I*, pages 81–88. International Society for Optics and Photonics, January 1984.

Allan R Gersborg-Hansen, Ole Sigmund, and Robert B Haber. Topology optimization of channel flow problems. *Structural and Multidisciplinary Optimization*, 30(3):181–192, June 2005.

Christophe Geuzaine and Jean-François Remacle. Gmsh: A 3-D finite element mesh generator with built-in pre- and post-processing facilities. *International Journal for Numerical Methods in Engineering*, 79(11): 1309–1331, September 2009.

James K Guest and Jean H Prévost. Topology optimization of creeping fluid flows using a Darcy–Stokes finite element. *International Journal for Numerical Methods in Engineering*, 66(3):461–484, 2006.

James K Guest, J H Prévost, and T Belytschko. Achieving minimum length scale in topology optimization using nodal design variables and projection functions. *International Journal for Numerical Methods in Engineering*, 61(2):238–254, August 2004.

Raphael T Haftka. Techniques for thermal sensitivity analysis. *International Journal for Numerical Methods in Engineering*, 17(1):71–80, 1981.

Evert C Hooijkamp and Fred van Keulen. Topology Optimization for Linear Thermo-Mechanical Transient Problems: Modal Reduction and Adjoint Sensitivities. *International Journal for Numerical Methods in Engineering*, 47(2):557, 2017.

Evert C Hooijkamp, Emiel van de Ven, Matthijs Langelaar, and Fred van Keulen. Proper Handling of Thermal Errors. *Mikroniek*, 54(3):60–66, June 2014.

Thomas J R Hughes, Leopoldo P Franca, and Marc Balestra. A new finite element formulation for computational fluid dynamics: V. Circumventing the babuška-brezzi condition: a stable Petrov-Galerkin formulation of the stokes problem accommodating equal-order interpolations. *Computer Methods in Applied Mechanics and Engineering*, 59(1):85–99, 1986.

Fred van Keulen, Raphael T Haftka, and N H Kim. Review of options for structural design sensitivity analysis. Part 1: Linear systems. *Computer Methods in Applied Mechanics and Engineering*, 194(30-33):3213–3243, August 2005.

Ji-Yeon Kim, Kang-Soo Park, and Sung-Kie Youn. The Design of Reflective Mirrors for High-power Laser Systems using Topology Optimization. In *11th World Congress of Structural and Multidisciplinary Optimization*, Rio de Janeiro, 2005.

Anders Klarbring, Joakim Petersson, Bo Torstenfelt, and Matts Karlsson. Topology optimization of flow networks. *Computer Methods in Applied Mechanics and Engineering*, 192(35-36):3909–3932, August 2003.

Stijn Koppen, Max van der Kolk, F C M van Kempen, Jan de Vreugd, and Matthijs Langelaar. Topology optimization of multicomponent optomechanical systems for improved optical performance. *Structural and Multidisciplinary Optimization*, 58(3):1–17, March 2018.

Jules Kouatchou. Basic Comparison of Python, Julia, Matlab, IDL, and Java (2018 Edition), February 2018. URL `https://modelingguru.nasa.gov/docs/DOC-2676`.

Jun Ho Lee. Lightweight mirror design method using topology optimization. *Optical Engineering*, 44(5): 053002–6, May 2005.

Qing Li, Grant P Steven, and Y M Xie. Thermoelastic Topology Optimization for Problems with Varying Temperature Fields. *Journal of Thermal Stresses*, 24(4):347–366, April 2001.

Ying Li, Kazuhiro Saitou, and Noboru Kikuchi. Topology optimization of thermally actuated compliant mechanisms considering time-transient effect. *Finite Elements in Analysis and Design*, 40(11):1317–1331, July 2004.

D Mansell and US Air Force. Spiral grooved liquid cooled laser mirror. May 1973.

Arif Masud and Thomas J R Hughes. A stabilized mixed finite element method for Darcy flow. *Computer Methods in Applied Mechanics and Engineering*, 191(39-40):4341–4370, 2002.

Tadayoshi Matsumori, Tsuguo Kondoh, Atsushi Kawamoto, and Tsuyoshi Nomura. Topology optimization for fluid–thermal interaction problems under constant input power. *Structural and Multidisciplinary Optimization*, 47(4):571–581, February 2013.

Sebastian Nørgaard, Ole Sigmund, and Boyan Stefanov Lazarov. Topology optimization of unsteady flow problems using the lattice Boltzmann method. *Journal of Computational Physics*, 307(C):291–307, February 2016.

Panos Y Papalambros and Douglas J Wilde. *Principles of Optimal Design - Modeling and Computation 2nd ed - Panos Y. Papalambros, Douglass J. Wilde (Cambridge University Press, 2000).* Modeling and Computation. Cambridge University Press, 2nd edition, July 2010.

G J Park and B S Kang. Validation of a Structural Optimization Algorithm Transforming Dynamic Loads into Equivalent Static Loads. *Journal of Optimization Theory and Applications*, 118(1):191–200, 2003.

Claus B W Pedersen. Crashworthiness design of transient frame structures using topology optimization. *Computer Methods in Applied Mechanics and Engineering*, 193(6-8):653–678, February 2004.

Daniel J. Rixen. *Mechanical Analysis for Engineering*. December 2011.

Rupali Sahu, Vrushang Patel, Sandeep Kumar Singh, and B S Munjal. Structural optimization of a space mirror to selectively constrain optical aberrations. *Structural and Multidisciplinary Optimization*, 55(6):1–11, April 2017.

Enrique Sanchez-Palencia. *Non-Homogeneous Media and Vibration Theory*, volume 127 of *Lecture Notes in Physics*. Springer Berlin Heidelberg, Berlin, Heidelberg, 1980.

Sarah Saunders. HiETA Uses Renishaw Metal 3D Printer to Take Heat Exchangers From Prototyping to Commercial Production, January 2018. URL `https://3dprint.com/198933/hieta-renishaw-heat-exchangers/`.

Ole Sigmund. On the Design of Compliant Mechanisms Using Topology Optimization. *Mechanics of Structures and Machines*, 25(4):493–524, January 1997.

Ole Sigmund. Design of multiphysics actuators using topology optimization – Part I: One-material structures. *Computer Methods in Applied Mechanics and Engineering*, 190(49-50):6577–6604, 2001.

Ole Sigmund. Morphology-based black and white filters for topology optimization. *Structural and Multidisciplinary Optimization*, 33(4-5):401–424, January 2007.

Ole Sigmund and Kurt Maute. Sensitivity filtering from a continuum mechanics perspective. *Structural and Multidisciplinary Optimization*, pages 1–5, September 2012.

Ole Sigmund and Kurt Maute. Topology optimization approaches. *Structural and Multidisciplinary Optimization*, 48(6):1031–1055, August 2013.

Ole Sigmund and Joakim Petersson. Numerical instabilities in topology optimization: A survey on procedures dealing with checkerboards, mesh-dependencies and local minima. *Structural Optimization*, 16(1):68–75, 1998.

M Stolpe and Krister Svanberg. An alternative interpolation scheme for minimum compliance topology optimization. *Structural and Multidisciplinary Optimization*, 22(2):116–124, 2001.

Krister Svanberg. MMA and GCMMA – two methods for nonlinear optimization. Technical report.

Jyh-Haw Tang and Bonan Jiang. A study of fluid flow and heat transfer of three-dimensional plate-fin and tube heat exchangers by the least-squares finite element method. In *European Conference on Computational Fluid Dynamics*, pages 1–19, July 2006.

Yu Wang, Kai-Min Yu, and Charlie C L Wang. Spiral and conformal cooling in plastic injection molding . *Computer-Aided Design*, 63:1–11, June 2015.

Niclas Wiker, Anders Klarbring, and Thomas Borrvall. Topology optimization of regions of Darcy and Stokes flow. *International Journal for Numerical Methods in Engineering*, 69(7):1374–1404, 2007.

Chi Wu, Jianguang Fang, and Qing Li. Multi-material topology optimization for thermal buckling criteria. *Comput. Methods Appl. Mech. Engrg.*, pages 1–31, August 2018.

Kentaro Yaji, Takayuki Yamada, Seiji Kubo, Kazuhiro Izui, and Shinji Nishiwaki. A topology optimization method for a coupled thermal–fluid problem using level set boundary expressions. *International Journal of Heat and Mass Transfer*, 81:878–888, February 2015.

Kentaro Yaji, Masao Ogino, Cong Chen, and Kikuo Fujita. Large-scale topology optimization incorporating local-in-time adjoint-based method for unsteady thermal-fluid problem. *Structural and Multidisciplinary Optimization*, 58(2):1–6, February 2018.

Chungang Zhuang and Zhenhua Xiong. Temperature-Constrained Topology Optimization of Transient Heat Conduction Problems. *Numerical Heat Transfer, Part B: Fundamentals*, 68(4):366–385, June 2015.

O C Zienkiewicz and R L Taylor. *The Finite Element Method: Its Basis and Fundamentals*. Elsevier Ltd, seventh edition edition, 2013.

O C Zienkiewicz, R L Taylor, and P Nithiarasu. Introduction to the Equations of Fluid Dynamics and the Finite Element Approximation. Elsevier, 2014.